UNIVERSITY OF CALIFORNIA, SAN DIEGO

Fine-scale spatial and temporal plankton distributions in the Southern California Bight: lessons from *in situ* microscopes and broadband echosounders

A dissertation submitted in partial satisfaction of the
requirements for the degree Doctor of Philosophy

in

Oceanography

by

Christian Briseño-Avena

Committee in charge:

Peter J.S. Franks, Co-Chair
Jules S. Jaffe, Co-Chair
David M. Checkley Jr.
Michael R. Landry
Andrew T. Scull

2015

The Dissertation of Christian Briseño-Avena is approved, and it is acceptable in quality and form for publication on microfilm and electronically:

_____

_____

_____

_____
Co-Chair

_____
Co-Chair

University of California, San Diego

2015

DEDICATION

I dedicate this work to my mother, Ma. Rosa Elvira Avena Domínguez, single mother of four kids who taught me to be a person of integrity, respect, and strong work ethics. A woman who worked as a kindergarten teacher from 7 a.m. to 6 p.m., and sometimes later for 33 plus years until retirement (with only a few days missing in her entire career –when I and my siblings were born). No matter how big the adversities were she had the strength and courage to keep us afloat. Thank you, mother.

TABLE OF CONTENTS

LIST OF FIGURES

LIST OF TABLES

ACKNOWLEDGEMENTS

First and foremost I would like to thank my advisors Jules Jaffe and Peter Franks. I was very fortunate to work with them at Scripps Institution of Oceanography. They were great mentors to me and I will always carry with me their best present to me: their thorough scientific advice. I also thank them for having treated me not only as a graduate student, but also as a colleague. I will always be grateful to them for helping me to improve my English written and spoken skills.

I would like to thank my dissertation committee members Dave Checkley and Mike Landry. Their comments and suggestions during our committee meetings helped improve my research work. I also would like to thank committee member Andy Scull for agreeing to become part of my committee in such a short notice.

Many thanks to past and present members of the Jaffe Lab for their great support; Robert Glatts, Fernando Simonet, Ben Laxton, Justin Haag, Eric Orenstein, Andy Mullen. It was a treat working with all of you throughout my graduate career. I want to thank in special lab mate, and co-author Paul Roberts – I had so much fun working with him in the lab and in the field and he was always ready with feedback.

To the Franks lab members with whom I had the pleasure to work with throughout the years, Jenny Prairie, Meg Rippy, Darcy Taniguchi, Alain de Verneil, Stephanie Snyder, Bryce Inman, Jess C-Garwood (Why not!? – inside joke).

To my cohort peers and great friends, Alain de Verneil, Joseph Camapanale and his husband Greg Russo, Lauren Shipp and her husband Reggie Robertson, Mindi

Summers, Noelle Bowlin, Jill Harris, Matt Leslie, Cotton Rockwood, Levi Lewis…you are my family away from home. Thank you!

To my family and friends at home in Mexico, who supported me and encouraged me to follow my dreams, I will forever be indebted with them and I cannot thank enough.

I wouldn't have gone this far without the encouragement of my undergraduate advisors Lupita Robles Jarero, M.S., and Drs. Aarón Rodríguez Contreras and Eduardo Ríos Jara at the Universidad de Guadalajara, Mexico. They all thought I should pursue a graduate career in the sciences. To my master's advisor and friend Mark Benfield I want to thank for giving me the opportunity to come to the U.S. to pursue my graduate career in the ocean sciences –he thought I was "PhD material" and he pushed me to go further in pursuing a career in oceanography. Thank you all!

I have not enough words to thank my husband, James Fischer for being such a supportive partner through thick and thin during this long journey of graduate school. I love you and I thank you not only for supporting me, but also for challenging me to be a better person.

I would like to thank the several people and organizations that contributed to fund my PhD career. The Mexican agency Consejo Nacional de Ciencia y Tecnología (CONACyT) and its partner University of California Institute for Mexico and the United States (UC MEXUS) granted me with a 5-year scholarship to study at Scripps Institution of Oceanography. I wouldn't have been able to do this without their support and I will be forever indebted to them.

Not less important was the support I received through the SIO endowments and fellowships funded by generous philanthropists. Among them are the Arts Proceeds, Shirley Boyd Memorial Fellowship, and the Mexican Marine Science Scholars Fellowship (William T. Hammond). I thank them all for their support – it was instrumental for my professional development.

Chapter 2, in full, is currently being prepared for submission for publication of the material. Briseño-Avena, C., Franks, P.J.S., and Jaffe, J.S. The dissertation author was the primary investigator and author of this paper.

Chapter 3, in full, is a reprint of previously published material as it appears in Methods in Oceanography, 2015, Briseño-Avena, C., Roberts, P.L.D., Franks, P.J.S., and Jaffe, J.S. The dissertation author was the primary investigator and author of this paper.

Chapter 4, in full, is currently being prepared for submission for publication of the material. Briseño-Avena, C., Franks, P.J.S., and Jaffe, J.S. The dissertation author was the primary investigator and author of this paper.

Chapter 5, in full, has been submitted for publication as a short communication paper to Journal of Plankton Research. Briseño-Avena, C. The dissertation author was the primary investigator and solely author of this paper.

VITA

2015 Doctor of Philosophy, University of California San Diego

2009 Master of Science, Louisiana State University

2004 Bachelor of Science, Universidad de Guadalajara, Mexico

PUBLICATIONS

Briseño-Avena, C., Franks, P.J.S., and Jaffe, J.S. *in prep.* High-resolution optical measurements of taxon-specific plankton vertical distributions: evidence for regulation by water density and large fluorescent particles (*Marine Ecology Progress Series*)

Briseño-Avena, C., Roberts, P.L.D., Franks, P.J.S., and Jaffe, J.S. 2015. ZOOPS-O^2: A broadband echosounder with coordinated stereo optical imaging for observing plankton *in situ*. Methods in Oceanography, 12: 36-54.

Briseño-Avena, C., Jaffe, J.S., and Franks, P.J.S. *in prep*. Underwater active acoustics: an unexpected diversity of *echogenic* particles (*ICES Journal of Marine Sciences*)

Briseño-Avena, C. *in review.* First observation of the rhizarian *Paradinium poucheti* parasitizing the copepod *Oithona similis* in the Pacific Ocean: evidence from a moored *in situ* camera (*Journal of Plankton Research*)

ABSTRACT OF THE DISSERTATION

Fine-scale spatial and temporal plankton distributions in the Southern California Bight: lessons from *in situ* microscopes and broadband echosounders

by

Christian Briseño-Avena

Doctor of Philosophy in Oceanography

University of California, San Diego 2015

Peter J.S. Franks, Co-Chair
Jules S. Jaffe, Co-Chair

Phytoplankton and zooplankton are important components of marine ecosystems, and play a major role in the biological pump, affecting carbon transport in the global oceans. Their dynamic heterogeneous spatial and temporal distributions require special tools for observing them at the ecological scales relevant to the individual organisms. In this work, I used optic and acoustic methods to study Southern California Bight. Highly resolved spatial observations revealed cryptic maxima of fluorescent particles not observed with traditional fluorometers.

Furthermore, this high sampling resolution revealed that water density, and not depth, regulated the vertical position, and interactions between observed phytoplankton and zooplankton distributions. Underwater acoustic echosounders can be powerful tools to observe *in situ* plankton distributions. Interpreting the acoustic echoes, however, requires highly calibrated instruments and ground-truthing experiments to identify the source of acoustic signals. This work presents the description of a novel combination of a broadband, high-frequency (1.5-2.5 MHz) echosounder and a stereoscopic camera –combined, these systems can localize the echo produced by an individual target while simultaneously providing visual identification of the target. This work has provided one of the first comparisons of *in situ* measured broadband target strength (BTS) and the expected signal using a physical model. The results of this experiment revealed unexpected, important differences between measured and modeled BTS. This system was also used to make *in situ* observations of individual fragile gelatinous organisms, marine snow particles and phytoplankton, providing evidence of their significant acoustic reflectivity. Finally, using a moored *in situ* microscope (Scripps Plankton Camera) similar in design to the O-Cam helped identify a parasite-host interaction over a period of a few months. This is the first reported observation of *Paradinium poucheti* parasitizing *Oithona similis* in the North Pacific Ocean. The short time-series revealed that the prevalence of this parasite is higher than previously observed in other ocean basins.

CHAPTER 1

Introduction

Planktonic distributions in the open ocean impact ecosystem dynamics that in turn affect global carbon fluxes. In the upper ocean, primary producers form features such as the chlorophyll maximum and the primary productivity maximum (e.g., Venrick et al., 1973; Cullen and Eppley, 1981; Herman et al., 1981; Napp, 1987; Pierson et al., 2005). Herbivorous zooplankton also form biomass maxima at this scale (Fiedler, 1983). At smaller (cm to meters) vertical scales, phytoplankton form thin layers (Franks, 1995; Cowles et al., 1998; McManus et al., 2012; Prairie et al., 2010, 2011), and there is evidence that intense zooplankton grazing activity may be focused in and around these features (Benoit-Bird et al., 2009; Greer et al., 2013). Unfortunately, our ability to quantify and understand the mechanisms driving these planktonic distributions has been limited by the low temporal and spatial resolution of typical sampling devices such as plankton nets, Niskin bottles, and plankton pumps.

While tools exist to sample fine-scale fluorescent particle distributions (Cowles et al., 1993; Desiderio et al., 1993; Franks and Jaffe, 2001, 2008, Prairie et al., 2010), zooplankton are sampled mostly by nets, yielding coarse (>10 m vertical) spatial sampling resolution. It has been shown, however, that the vertical resolution necessary to detect zooplankton aggregations ranges from 1-10 meters (Longhurst and Herman, 1981; Napp, 1987; Graham et al., 2001). Our ability to sample grazers, and their prey and predators simultaneously at fine scales will allow us to gain a deeper

understanding of predator-prey interactions in the pelagic ecosystem, and how trophic dynamics at small scales propagate to larger-scale processes.

Recent technological advances in optical and acoustical sensors have improved our ability to sample the aquatic environment at high temporal (minutes-hours) and spatial (<0.1 m) resolution. These spatial scales are similar to the foraging ambits of the organisms being studied. Optical systems provide an ideal combination of fine-scale resolution and undisturbed sampling, and are a logical choice to study zooplankton-phytoplankton and zooplankton-zooplankton interactions. In addition, because of their far-reaching, fast-acquisition, and fast-processing capabilities, acoustic sensors are important tools for sampling planktonic particle (living and dead) distributions. In **Chapter 2** I used two optical systems and an acoustic system to quantify the fine-scale (meters) vertical distributions of phytoplankton and zooplankton in a coastal region of the Southern California Bight. The main goal of this chapter is to use these distributions to uncover ecological relationships among primary producers and their grazers, and grazers with their predators.

The first optical system is the Planar Laser Imaging Fluorometer (PLIF), designed to acquire two-dimensional images of the laser-stimulated *in vivo* fluorescence of individual chlorophyll-containing particles (e.g., Franks and Jaffe, 2001, 2008; Prairie et al., 2010). The second system, the O-Cam, was designed to acquire images of zooplankton and marine snow. Combined with other environmental sensors such as CTDs, fluorometers, and acoustic transducers, and mounted on a semi-Lagrangian platform, the Free-falling Imaging Device for Observing Plankton (FIDO-

Φ), these optical systems were deployed simultaneously to sample phytoplankton, zooplankton, marine snow, and their physical environment. The main objective was to understand how phytoplankton distributions affect the vertical location of grazers, and how these distributions might affect the spatial structure of potential predators of the grazers and each other.

Newly developed optic and acoustic systems must be tested and calibrated before any conclusions can be drawn from the data they acquire. Early versions of the Video Plankton Recorder (VPR), for example, underwent rigorous comparisons with commonly used tools such as the Multiple Opening Closing Net and Environmental Sensor System (MOCNESS; Benfield et al., 1996; Broughton and Lough, 2006). Similarly, the Laser Optical Plankton Counter (LOPC) was deployed with BONGO plankton nets to compare its performance and capability of quantifying plankton abundances (Herman *et al.*, 2004). The results from such experiments have shown the advantages and limitations of optical systems for sampling different zooplankton taxa. One advantage of optical systems is their potential for imaging organisms undisturbed, allowing us to infer behaviors such as orientation in the water column, diel vertical migration mode, and natural distributions at the scales of the organisms. Due to their small imaging volume, however, optical systems tend to undersample highly motile taxa (e.g., euphausiids, chaetognaths) and organisms at low abundances (Benfield et al., 1996). However, optical systems are ideal for imaging fragile, non-living particles such as marine snow that cannot be quantitatively sampled by nets (González-Quirós and Checkley, 2006).

Another objective in **Chapter 2** was to compare the abundances of plankton obtained with the O-Cam system against those estimates from more traditional methods, such as nets. For this work I used the 1 m^2, 202 μm mesh size, MOCNESS. **Chapter 2** presents the results of the alternating deployments of the O-Cam and MOCNESS systems from a cruise to the Santa Barbara Basin on September 25-October 3, 2010 on board R/V Melville. This exercise emphasizes the quantitative capabilities of the O-Cam.

Thanks to their far-reaching detection, fast sampling rate, and relatively large sample volume, acoustic systems are particularly suited for exploring plankton distributions in the water column (Pieper et al., 1990; Lavery et al., 2007; Stanton, 2012). However, the interpretation and processing of acoustic data are strongly affected by the lack of knowledge of acoustic properties of living and non-living particles suspended in the water column (Richter, 1985a,b). Interpretation of acoustic signals relies on the uniqueness of the acoustic backscatter signal from a given organism or particle. Extant acoustic backscatter models (Stanton et al., 1996) mostly use laboratory-based measurements of zooplankton (Beamish, 1971; Greenlaw, 1977; Richter, 1985a,b; Lavery et al., 2002), often focusing on a few taxa (mostly euphausiids), and with limited *in situ* calibration measurements (Jaffe et al., 1998), making data interpretation challenging. It is clear that better calibrations of *in situ* acoustic measurements of plankton and other particles need to be carried out to aid in the interpretation of *in situ* acoustic data. **Chapter 3** describes a newly developed

system to measure the *in situ* acoustic signal of individual targets while obtaining the visual identification of the organism or particle producing the signal.

The Zooplankton Sonar (ZOOPS) and the two stereoscopically calibrated O-Cams were combined in a single platform known as ZOOPS-O^2 (ZOOPS-O-squared). The acoustic system, ZOOPS, is a broadband, high-frequency (1.5-2.5 MHz) sonar that detects echoes from individual zooplankton and other particles 0.5 mm to 2 cm in size. For this study, ZOOPS-O^2 was deployed in the Southern California Bight and repeatedly profiled at inshore and offshore locations. The O-Cams provided high-resolution optical images of the particles being insonified by ZOOPS, allowing me to compare acoustic and optical data collected *in situ* from the same particles. Because of the stereoscopic nature of this system, it was possible to determine the orientation and identification of unique echo-producing particles. The latter provided unique data that could be used to compare the *in situ* measured broadband target strength (BTS) and signal spectra to those expected from physical models. **Chapter 3** provides the results of a comparison of the BTS and spectra of 224 individual copepods and the BTS and spectra from a well-known model: the Distorted Wave Born Approximation (DWBA; Chu and Ye, 1999) applied to a spheroid model. The parameters for the spheroid were extracted from the three-dimensional prosome length, width, and pose (orientation) of the *in situ* imaged copepods using the stereoscopically calibrated optical system. Measuring the effect of orientation on the overall BTS of a target is important because physical models predict that the pose (along with speed and sound contrast) of a target significantly affects the amount of sound scattered by the insonified particle. The

similarities and differences observed between the modeled and *in situ* measured BTS and spectra are discussed in **Chapter 3**.

In addition to copepods, a variety of other planktonic targets were observed in the ZOOPS-O^2 data collected during the same fieldwork. The organisms included other crustaceans such as euphausiids, mysids, and ostracods, as well as fragile taxa such as hydromedusae, doliolids, ctenophores, chaetognaths, and appendicularians (both with and without their "house"). Most surprisingly of all, marine snow particles and diatom aggregations were detected in the acoustic records. **Chapter 4** presents the results of these observations and discusses the consequences of not taking into account the potential contribution to acoustic surveys by fragile taxa, marine snow, and phytoplankton layers. For example, it is well known that phytoplankton and marine snow layers are pervasive phenomena in the world coastal regions. Furthermore, these layers persist for hours to days and extend over kilometers. Neglecting these common features during acoustic surveys without proper simultaneous ground truthing can lead to misinterpretations of the acoustic signals, potentially affecting the acoustic estimates. Admittedly, this work utilizes high frequencies (1.5-2.5 MHz) while commonly used echosounders are focused at much lower frequencies. However, Timmerman and collaborators (Timmerman et al., 2014) recently suggested that a strong sound scattering layer detected by a Simrad 200 kHz channel was most likely due to flocculated *Pseudo-nitzschia* sp. While the authors cautiously suggested that the diatom layer they observed with another optical system (the In Situ Ichthyoplankton Imaging System or ISIIS) was responsible for the observed acoustic signal, the

research presented in **Chapter 4** of this dissertation provides unequivocal evidence that flocculated material (marine snow) and high concentrations of diatoms are indeed capable of reflecting sound.

Deployment modes of optical systems

Imaging devices, from the Video Plankton Recorder (VPR; Davis et al., 1996), to the Zooplankton Visualization System (ZOOVIS; Bi et al., 2013) to the In Situ Ichthyoplankton Imaging System (ISIIS; Cowen and Guigand, 2008) and the Laser Optical Plankton Counter (LOPC; Herman et al., 2004), were designed to be towed, and are capable of being mounted on fast-towed platforms, including net frames (e.g., MOCNESS, Bongo Nets). The O-Cam, on the other hand, was designed to be self-contained and deployable as a vertical profiler, either tethered to a ship or mounted on a free-falling platform (as described in **Chapter 2**). In this context, the LOPC has been deployed on autonomous profiling floats (SOLOPC; Checkley et al., 2008). However, the O-Cam can also be moored to permanent structures and is capable of yielding highly resolved time series of planktonic images providing new insights into species-species interactions. A camera designed after the O-Cam has been permanently moored on the Scripps Pier (and is referred to as the Scripps Plankton Camera or SPC) since March 13, 2015 has been continuously imaging planktonic organisms at 1 Hz.

In **Chapter 5** I report the first observation of a time-sensitive parasitic event affecting *Oithona similis* copepod assemblages in the North Pacific using SPC image data. Reports of copepods afflicted by the parasite *Paradinum poucheti* in Mediterranean waters date back more than a century (Chatton, 1910). More recently *Oithona* spp. infected by *P. poucheti* was studied in the same basin, and in the Northeast Atlantic Ocean (Skovgaard and Saiz, 2006; Skovgaard and Daubgjerg, 2008). The observation of the gonosphere, the external physical manifestation of the parasite in *O. similis* (which only lasts a few hours) was successfully captured by the moored SPC. The high resolution and fast image acquisition of this *in situ* microscope allowed me to first identify the parasite's characteristic gononosphere attached to the copepod's urosome, and second to estimate the parasite prevalence with a temporal resolution of a couple of days over a four-month period. These first observations of *P. poucheti* infection of *O. similis* in the North Pacific suggest that parasite prevalence in *Oithona* assemblages might be higher than previously thought (Skovgaard, *pers. comm.*). While direct sampling is still needed to gain further insights into the effect this parasite has on its host, the monitoring capability of the SPC/O-Cam will allow us to estimate parasite prevalence over longer – even interannual – time scales, supplemented by physical and chemical sensors available from the various SIO pier monitoring programs.

References

Beamish, P. 1971. Quantitative measurements of acoustic scattering from zooplanktonic organisms. Deep-Sea Research, 18: 811-822.

Benfield, M.C., Davis, C.S., Wiebe, P.H., Gallager, S.M., Lough, R.G., and Copley, N.J. 1996. Video Plankton Recorder estimates of copepod, pteropod and larvacean distributions from a stratified region of Georges Bank with comparative measurements from a MOCNESS sampler. Deep-Sea Research II, 43: 1925-1945.

Benoit-Bird, K.J., Cowles, T.J., and Wingard, C.E. 2009. Edge gradients provide evidence of ecological interactions in planktonic thin layers. Limnology and Oceanography, 54: 1382-1392.

Bi, H., Cook, S., Yu, H., Benfield, M.C., and Houde, E.D. 2013. Deployment of an imaging system to investigate fine-scale spatial distribution of early life stages of the ctenophore *Mnemiopsis leidyi* in Chesapeake Bay. Journal of Plankton Research, 35: 270-280.

Broughton, E.A., and Lough, R.G. 2006. A direct comparison of MOCNESS and Video Plankton Recorder zooplankton abundance estimates: Possible applications for augmenting net sampling with video systems. Deep-Sea Research II, 53: 2789-2807.

Chatton, E. 1910. Paradinium poucheti n.g., n. sp., flagellé parasite d'Acartia clausi Giesbrecht (Copépode pélagique) (Note préliminaire). C. R. Soc. Biol. 69: 341-343.

Checkley, D.M., Jr., Davis, R.E., Herman, A.W., Jackson, G.A., Beanlands, B., and Regier, L.A. 2008. Assessing plankton and other particles in situ with the SOLOPC. Limnology and Oceanography, 53: 2123-2136.

Chu, D. and Ye, Z. 1999. A phase-compensated distorted wave Born approximation representation of the bistatic scattering by weakly scattering objects: Applications to zooplankton. Journal of the Acoustical Society of America, 106: 1732-1743.

Cowen, R. K. and Guigand, C.M. 2008. *In situ* ichthyoplankton imaging system (*IS*IIS): system design and preliminary results. Limnology and Oceanography: Methods, 6: 126-132.

Cowles, T.J., Desiderio, R.A., and Carr, M. 1998. Small-scale planktonic structure: perspective and trophic consequences. Oceanography, 11: 4-9.

Cowles, T.J., Desiderio, R.A., and Neuer, S. 1993. *In situ* characterization of phytoplankton from vertical profiles of fluorescence emission spectra. Marine Biology, 115: 217-222.

Cullen, J.J. and Eppley, R.W. 1981. Chlorophyll maximum layers of the Southern California Bight and possible mechanisms of their formation and maintenance. Oceanologica Acta, 4:23-32.

Fiedler, P.C. 1983. Fine-scale spatial patterns in the coastal epiplankton off southern California. Journal of Plankton Research, 5: 865-879.

Franks, P.J.S. 1995. Thin layers of phytoplankton: a model of formation by near-inertial wave shear. Deep-Sea Research I, 42: 75-91.

Franks, P.J.S. and Jaffe, J.S. 2001. Microscale distributions of phytoplankton: initial results from a two-dimensional imaging fluorometer, OSST. Marine Ecology Progress Series, 220: 59-72.

Franks, P.J.S. and Jaffe, J.S. 2008. Microscale variability in the distributions of large fluorescent particles observed *in situ* with a planar laser imaging fluorometer. Journal of Marine Systems, 69: 254-270.

González-Quirós, R. and Checkley, D.M., Jr. Occurrence of fragile particles inferred from optical plankton counters used in situ and to analyze net samples collected simultaneously. Journal of Geophysical Research, 111: C05S06.

Graham, W.M., Pages, F., and Hammer, W.M. 2001. A physical context for gelatinous zooplankton aggregations: a review. *In* Purcell, J.E., Graham, W.M., and Dumont, H.J. (Eds.). Jellyfish blooms: ecological and societal importance. Developments in Hydrobiology, Springer, Netherlands, 155: 199-212.

Greenlaw, C.F. 1977. Backscattering spectra of preserved zooplankton. Journal of the Acoustical Society of America, 62: 44-52.

Greer, A.T., Cowen, R.K., Guigand, C.M., McManus, M.A., Sevaddjian, J.C., and Timmerman, A.H.V. 2013. Relationships between phytoplankton thin layers and the fine-scale vertical distributions of two trophic levels of zooplankton. Journal of Plankton Research, 35: 939-956.

Herman, A.W., Beanlands, B, and Phillips, E. 2004. The next generation of Optical Plankton Counter: the Laser-OPC. Journal of Plankton Research, 26: 1135-1145.

Herman, A.W., Sameoto, D.D., and Longhurst, A.R. 1981. Vertical and horizontal distribution patterns of copepods near the shelf break south of Nova Scotia. Canadian Journal of Fisheries and Aquatic Sciences, 38: 1065-1076.

Jaffe, J.S., Ohman, M.D., and de Robertis, A. 1998. OASIS in the sea: measurement of the acoustic reflectivity of zooplankton with concurrent optical imaging. Deep-Sea Research II, 45: 1239-1253.

Lavery, A.C., Stanton, T.K., McGehee, D.E., and Chu, D. 202. Three-dimensional modeling of acoustic backscattering from fluid-like zooplankton. Journal of the Acoustical Society of America, 111: 1197-1210.

Lavery, A.C., Wiebe, P.H., Stanton, T.K., Lawson, G.L., Benfield, M.C., Copley, N. 2007. Determining dominant scatters of sound in mixed zooplankton populations. Journal of the Acoustical Society of America, 122: 3304-3326.

Longhurst, A.R. and Herman, A.W. 1981. Do oceanic zooplankton aggregate at, or near, the deep chlorophyll maximum? Journal of Marine Research, 39: 353-356.

McManus, M.A., Sevadjian, J.C., Benoit-Bird, K.J., Cheriton, O.M., Timmerman, A.H.V., and Waluk, C.M. 2012. Observations of thin layers in coastal Hawaiian waters. Estuaries and Coasts, 35: 1119-1127.

Napp, J.M. 1987. Primary productivity maxima in the Southern California Bight: distribution, predicted depth and nutritional content. Oceanologica Acta, 10: 329-337.

Pieper, R.E., Holliday, D.V., and Kleppel, G.S. 1990. Quantitative zooplankton distributions from multifrequency acoustics. Journal of Plankton Research, 12: 433-441.

Pierson, J.J., Leising, A.W., Halsband-Lenk, C., and Ferm, N. 2005. Vertical distribution and abundance of *Calanus pacificus* and *Pseudocalanus newmani* in relation to chlorophyll *a* concentrations in Dabob Bay, Washington. Progress in Oceanography, 67: 349-365.

Prairie, J.C., Franks, P.J.S., and Jaffe, J.S. 2010. Cryptic peaks: Invisible vertical structure in fluorescent particles revealed using a planar laser imaging fluorometer. Limnology and Oceanography, 55: 1943-1958.

Prairie, J.C., Franks P.J.S., Jaffe, J.S., Doubell, M.J., and Yamazaki, H. 2011. Physical and biological controls of vertical gradients in phytoplankton. Limnology and Oceanography: Fluids and Environments, 1: 75-90.

Richter, K.S. 1985a. Acoustic scattering at 1.2 MHz from individual zooplankters and copepod populations. Deep-Sea Research, 32: 149-161.

Richter, K.E. 1985b. Acoustic determination of small-scale distributions of individual zooplankters and zooplankton aggregations. Deep-Sea Research, 32: 163-182.

Skovgaard, A. and Daugbjerg, N. 2008. Identity and systematic position of *Paradinium poucheti* and other *Paradinium*-like parasites of marine copepods based on morphology and nuclear-encoded SSU rDNA. Protist, 159: 401-413.

Skovgaard, A. and Saiz, E. 2006. Seasonal occurrence and role of protistan parasites in coastal marine zooplankton. Marine Ecology Progress Series, 327: 37-49.

Stanton, T.K. 2012. 30 years of advances in active bioacoustics: *A personal perspective*. Methods in Oceanography, 1-2: 49-77.

Stanton, T.K., Chu, D., and Wiebe, P.H. 1996. Acoustic scattering characteristics of several zooplankton groups. ICES Journal of Marine Science, 53: 289-295.

Timmerman, A.H.V., McManus, M.A., Cheriton, O.M., Cowen, R.K., Greer, A.T., Kudela, R.P., Ruttenberg, K., and Sevadjian, J. 2014. Hidden layers of toxic diatoms in a coastal bay. Deep-Sea Research II, 101: 129-140.

Venrick, E.L., McGowan, J.A., and Mantyla, A.W. 1973. Deep maxima of photosynthetic chlorophyll in the Pacific Ocean. Fishery Bulletin, 71: 41-52.

CHAPTER 2

High-resolution optical measurements of taxon-specific plankton vertical distributions: evidence for regulation by water density and large fluorescent particles

Christian Briseño-Avena, Peter J.S. Franks, and Jules S. Jaffe

2.1. Abstract

Trophic interactions involving zooplankton and phytoplankton are difficult to assess *in situ* at spatial scales relevant to the individuals. This work presents high spatial resolution observations of the nighttime vertical distributions of plankton and particles in stratified coastal waters of the Southern California Bight, obtained using a planar laser imaging fluorometer (PLIF) augmented with a shadowgraph zooplankton imaging system (O-Cam). Comparisons of the O-Cam with net samples suggest that this system generates reliable relative abundance estimates of several zooplankton groups. Using these optical sensors augmented with hydrographic profilers we found that phytoplankton and zooplankton distributions were more closely associated with water density than depth – a result that would not be apparent using with traditional discrete sampling. Cryptic maxima in fluorescent particles appeared to regulate the relative distributions of zooplankton grazers and their predators. Our analyses suggest that cyclopoid copepods can be important to carbon export by being located below both the subsurface chlorophyll *a* maximum and the fluorescent particle maximum

2.2. Introduction

Plankton distributions are known to be patchy over spatial scales as small as cm and time scales as short as minutes (Steele, 1978, and references therein). In the vertical direction, the zooplankton community can change locally daily through diel vertical migrations (DVM; e.g. Ohman et al., 1983; Lampert, 1989; Loose and Dawidowicz, 1994). On longer time scales some zooplankton shift their vertical distributions seasonally – such as during diapause (or dormancy) when certain copepods overwinter at depth in dense aggregations (e.g. Hirche, 1996; Alldredge et al., 1984; Ohman et al., 1998; Johnson and Checkley, 2004). Vertical repositioning at shorter time and spatial scales can also occur in response to reproduction, feeding, predation and physical forcing. Appendicularians, for example, tend to aggregate at the surface during mating to increase their encounter rates, but are usually found in deeper waters when not reproducing (Alldredge, 1982; Tomita et al., 2003). Gelatinous organisms (such as hydromedusae and ctenophores) on the other hand have often been observed in higher concentrations at density discontinuities (e.g. Jacobsen and Norrbin, 2009; Greer et al., 2013 and references therein). Copepods and euphausiids tend to exhibit some of the most intense DVMs, which can also be ontogenetic (differential timing of migration among life stages) (e.g. Bollens et al., 1992; de Robertis et al., 2000; Holliland et al., 2012).

This dynamic vertical repositioning by zooplankton poses challenges for plankton ecologists, inspiring the design of new tools to sample these organisms to unveil the mechanisms (both physical and biological) driving the observed

distributions. This has resulted in a variety of multi-net sampling devices capable of taking samples over discrete depth intervals either vertically (e.g., Puget Sound Closing Net, MultiNet) or obliquely (e.g., MOCNESS). Pumps have also been commonly used to sample zooplankton vertical distributions (e.g. Holliday et. al., 1989; Masson et al., 2004). Through such tools the DVM was first identified, its different modes characterized, and the mechanisms driving these different modes revealed.

Discrete vertical sampling using bottles also led to the discovery of the chlorophyll *a* max (see Lorenzen, 1966). This was soon followed by observations of associated vertical distributions of zooplankton that were potentially grazing on these phytoplankton features (e.g. Frost, 1972; Napp et al., 1988a,b). However, the results were mixed and sometimes the vertical distributions of zooplankton and phytoplankton could not explained using the coarse sampling techniques. It has become clear that finer-scale vertical sample resolution – sampling on the scale of the organism's foraging ambits – would be needed to further our understanding of phytoplankton-zooplankton and zooplankton-zooplankton interactions.

Measuring fine-scale distributions of grazers with respect to their food source(s) is difficult using nets that, at best, sample over tens of meters vertically and filter hundreds of cubic meters of water. Furthermore, stratified sampling by towed nets is usually performed relative to depth: vertical displacements of isopycnals and organisms by internal waves, for example, are aliased by such sampling, and any potential relationship of the organism distributions to other variables such as density

will be lost. The introduction of imaging devices to observe individual plankton *in situ* has opened up new opportunities to quantify their fine-scale distributions while simultaneously measuring environmental parameters (see a historical review of the evolution of imaging devices by Wiebe and Benfield, 2003).

Using imaging devices such as the Video Plankton Recorder (VPR; Davis et al., 1996), the In Situ Ichthyoplankton Imaging System (ISIIS; Cowen and Guigand, 2008), the Optical Plankton Counter (OPC; Herman et al., 2004) just to name a few, observations of the fine-scale distributions of phytoplankton and zooplankton are now possible. In particular, such imaging devices are advancing our understanding of distributions of fragile taxa (e.g., cnidarians and pelagic hemicordates), which are oftentimes undersampled or destroyed by nets (e.g. Benfield et al., 1996; Remsen et al., 2004). Recently, for example, the ISIIS system was utilized to study phytoplankton thin layers (cm to m in thickness) and the associated zooplankton from two trophic levels (Greer et al., 2013).

The subsurface chlorophyll maximum (CMAX) layer is often the site of intense biological activity, such as grazing, predation, sexual reproduction and infection, all factors affecting the biological pump and associated carbon transport (see Cullen, 2015 for a review of the CMAX). For example, it has often been found that the zooplankton abundance maximum occurs above or in the CMAX (e.g., Cullen and Eppley, 1981; Herman et al., 1981; Herman, 1983; Jaffe et al., 1998). Using an undulating towed vehicle with an electronic zooplankton counter, Herman (1983) found that most calanoid copepods (the locally dominant zooplankton group) were

located above the CMAX in an Arctic basin (Baffin Bay), and in the Northwest Atlantic off Nova Scotia (Herman et al., 1981). Similar distributions have been observed in other ocean basins (e.g., Fiedler, 1983; Castro et al., 1991). However, these works have focused on one type of organism: grazers, such as copepods. Investigations such as that of Greer and collaborators (Greer et al., 2013), where at least three trophic levels are simultaneously sampled, are still necessary to better understand the mechanisms behind complex predator-prey interactions in pelagic ecosystems.

Here we explore the relationships among phytoplankton fluorescence distributions and vertical structure of different zooplankton taxa in the coastal Southern California Bight (SCB). We used the Free-falling Imaging Device for Observing Plankton (FIDO-Φ; Franks and Jaffe, 2008) equipped with a planar laser imaging fluorometer (PLIF), a zooplankton-imaging device (O-Cam) and a CTD. We first demonstrate the quantitative capabilities of the O-Cam by comparing the image-derived abundances to those obtained with the Multiple Opening and Closing Net and Environmental Sensor System (MOCNESS), a net system often used to sample zooplankton obliquely over discrete depth intervals. We then analyze the data from the environmental sensors, the PLIF, and the O-Cam to study the fine-scale vertical distribution of phytoplankton, particles and zooplankton.

2.3. Materials and Methods

2.3.1. Description of the CalEchoes and FIDO-Φ-O-Cam cruises

Data were acquired during two separate cruises located within the SCB. The first was the cruise "California's Ecological Changes and Historical Origins" (CalEchoes) carried out in the Santa Barbara Basin (square marker in Fig. 2.1) aboard the R/V Melville from September 25 to October 3, 2010. During this cruise we tested the quantitative ability of the newly developed underwater microscope, O-Cam (see below for a description) to estimate zooplankton abundances. O-Cam-derived estimates were compared to those obtained using a 1 m^2, 202 μm mesh size MOCNESS.

The second field expedition was the FIDO-Φ-O-Cam cruise conducted near the head of a canyon in the northern end of the Santa Catalina Basin aboard the R/V New Horizon during August 18-23 2011 (triangle symbol in Fig. 2.1). Fine-scale vertical distributions of zooplankton and phytoplankton were resolved using the free-falling vehicle FIDO. The FIDO was equipped with an O-Cam to image zooplankton, and a PLIF to measure fluorescent and scattering particle sizes, distributions and concentrations.

2.3.1.1. CalEchoes O-cam image annotation and zooplankton abundance estimation

The O-cam is a self-contained shadowgraph camera designed to image zooplankton (Fig. 2.2), similar to the O-Cam described in Briseño-Avena et al. (2015).

The O-Cam had a sampling volume of 0.106 L, estimated in the lab by measuring the distance a checkerboard pattern printed on a transparency target went out of focus in the near and far depth of field of the camera (15 cm) multiplied by the circular area of the field of view (7. 0686 cm^2). During the CalEchoes cruise, the O-cam was vertically profiled on its own platform from the starboard boom winch from 0 to 500 m, the maximum operation depth of the system. Vertical profiles were carried out before or following MOCNESS tows (Table I). Only downcast data were analyzed.

O-cam images were manually annotated using a graphical user interface in Matlab. Every image for all profiles presented here was visually inspected for the presence of zooplankton. For the CalEchoes O-Cam data set, a total of 17,633 images, spanning 6 vertical profiles were annotated. The annotation consisted of drawing a box around the identified organism, extracting the subimage, and then assigning it to one of 22 predetermined taxonomic categories. These categories were created based on the most common zooplankton observed in early deployments of the O-Cam. For this work, the most abundant categories were: hydromedusae, euphausiids, calanoid copepods, cyclopoid copepods, and appendicularians (Fig. 2.2). Abundance estimates (organisms per liter) were obtained by dividing the number of observations in each frame by the volume sampled per frame (0.106 L).

2.3.1.2. CalEchoes MOCNESS sample processing

MOCNESS samples were preserved in 1.8% formalin solution at sea and processed in the lab using the specialized zooplankton flatbed scanner ZOOSCAN

(Gorsky et al., 2010) following the method described in Powell and Ohman (2012). Briefly, the preserved samples were size-fractionated using 5 mm, 1 mm and 0.2 mm meshes. The contents of each mesh were re-suspended in a known volume of filtered seawater and aliquots from each size fraction were scanned. Usually $1/100^{th}$ of the 0.2 mm fraction, $1/20^{th}$ of the 1 mm fraction and the full contents of the 5 mm fraction were scanned. This method ensured that larger organisms, which tend to be less abundant, were included in the abundance estimates. Regions of interest (ROI) containing organisms were extracted and automatically sorted into 23 zooplankton categories using the ZOOSCAN software. The sorting of each ROI was visually inspected and corrected if necessary. Abundances were reported as organisms per liter.

2.3.1.3. CalEchoes O-cam versus MOCNESS

The O-Cam abundance estimates were compared to those obtained from the net samples. The MOCNESS is a towed system and typically collects samples obliquely over nine discrete depth intervals starting at the targeted depth and sequentially closing and opening nets on the way up – there are a total of 10 nets, but net number 1 is open when the system is deployed, and is generally not used for quantitative analyses. Because the nets sampled over irregularly spaced depth intervals (spanning tens of meters vertically), the O-Cam abundance data were integrated over the same depth interval sampled by each net. As a result, 9 bins of O-cam abundance estimates were created for each profile, one for each MOCNESS net and tow. The O-Cam estimates from each profile were compared against the closest tow in time or

space as shown in Table I. Because each method is subject to errors (sampling errors, processing errors, avoidance issues, etc.) a Type II regression analysis was used to compare the data sets.

2.3.2. Description of the FIDO-Φ-O-Cam cruise platform deployment

The FIDO-Φ-O-Cam (Fig. 2.3) was utilized to image phytoplankton and zooplankton simultaneously in a coastal location in the Santa Catalina Basin. One major difference between previous FIDO-Φ configurations (e.g. Prairie et al., 2010) is that the present version included an O-cam to image zooplankton. The O-Cam was placed immediately above the PLIF imaging volume (Fig. 2.3b). In addition an SBE25 CTD and an SB49 CTD (Sea-Bird Electronis, U.S.A.) were placed on the platform; the SBE25 also included an ECO FL fluorometer (Wet Labs).

The region where the FIDO-Φ-O-Cam platform was deployed is bathymetrically complex; however, the platform was deployed in the same general location relative to the bathymetric features. The platform was deployed only during nighttime to avoid contamination of the PLIF images by ambient sunlight (Franks and Jaffe, 2008). Each FIDO-Φ-O-Cam drop was composed of three consecutive profiles; data were acquired during the downcast to a maximum depth of 75 m. After each drop cycle was completed, the platform was recovered for data download and system updates, such as battery charging or replacement. Because the platform drifted with the water currents, the ship was repositioned to the original drop location centered at 33° 33’ N and 118° 54’ W and FIDO-Φ-O-Cam re-deployed for a new cycle. Only the

9 profiles when all the sensors were fully functional were chosen for the present analysis (Table II).

2.3.2.1. PLIF and O-Cam Image Processing

The PLIF has been extensively described elsewhere (Franks and Jaffe, 2001, 2008; Prairie et al., 2010). Briefly, the PLIF system consists of a CCD camera (Cooke Sensicam) equipped with a 50 mm Nikor lens (f/1.4 aperture) that images a 6.5 mm thick sheet of light at a 90º angle (Figure 2.3b). The light was produced by a 3-W, 532-nm diode-pumped solid-state laser (CVI Melles Griot). The field of view of the camera was approximately 9.8 x 13 cm and had a resolution slightly smaller than 100 μm per pixel. The camera used a rotating mechanism with two types of filters – one that transmitted light at wavelengths of 670-690 nm, the same wavelengths used to measure chlorophyll *a* fluorescence, and a second that transmitted all wavelengths in the visible spectrum. The PLIF camera acquired images at 2 Hz, alternately imaging fluorescent and scattering particles with an exposure time of 20 ms. PLIF bulk fluorescence, obtained by integrating the fluorescence over the entire image, is linearly correlated with fluorescence intensity measured by commercial fluorometers (Franks and Jaffe, 2001; Prairie et al., 2010). Fluorescent particle and scattering particle concentrations were obtained following the protocol of Prairie et al. (2010): images were corrected for spatial variations in the intensity of the incident laser sheet. A threshold was used to define “fluorescent particles”, which were pixels with fluorescence greater than a threshold fluorescence corresponding to the background

fluorescence. The threshold was determined separately for each profile prior to processing. Fluorescent particles included fluorescent organisms smaller than 100 microns (the imaging pixel size), and aggregates up to millimeters in diameter. "Scattering particles" were defined similarly to the fluorescent particles, but were obtained from the scattered-light images rather than the fluorescence images. A total of 6,116 fluorescence/scattering images from 9 profiles were analyzed.

2.3.2.2. Sensor Data Merging and Statistical Analysis

Given the fact that most of the instruments had their own pressure sensors, all data from a given profile were merged based on depth. The PLIF imaging volume was 0.8 m below the depth sensor and this offset was corrected before merging. Because the O-Cam was self-contained and had its own temperature-pressure (TP) sensor no depth corrections were necessary for this data set. After data merging, each parameter was independently binned by depth using a 0.3 m bin size and then smoothed over 1.5 m using LOWESS to remove small spatial scale noise. The result was a fixed sized data vector for each parameter, giving profiles that could be compared to each other using regular depth coordinates. In addition, data from the PLIF, SBE 25-ECO FL, SBE 49 and O-Cam were binned in density coordinates using a density bin size of 0.09 kg/m^3. This bin size was found to be the minimum size that would allow enough observations per bin, given the density range of 1023.8 to 1026.1 kg/m^3. Normalized profiles were calculated in depth and density coordinates by dividing all the values in a given profile by its maximum. The normalized values thus varied between zero and

one. Finally, the normalized density-binned profiles were averaged over time to create canonical vertical profiles for each parameter. This time averaging was justifiable given the spatial and temporal proximity of drops and profiles (see Table II), and the similarity among distributions of properties in different normalized profiles. A Spearman rank correlation analysis was carried out to investigate the relationships among the observed distributions. This non-parametric test was appropriate due to the fact that *a priori* t-tests rejected the null hypothesis that the canonical profile data came from a normal distribution.

2.3. Results and Discussion

2.3.1. CalEchoes O-Cam versus MOCNESS abundance estimates

The Type II regression analysis yielded positive relationships between O-Cam and MOCNESS abundance estimates for all five classes of zooplankton (plus all copepods combined) included in this work (Fig. 2.4). In all cases the regression line had a lower slope than the 1:1 line, indicative of abundance overestimation (underestimation) by the O-Cam (MOCNESS).

A Type II regression analysis does not seek to predict one variable using the other, but rather to show how two variables co-vary. All the O-Cam/MOCNESS relationships were positive. While the strongest correlations between MOCNESS and O-Cam-derived abundances were observed for hydromedusae and appendicularians it should be noted that these groups also showed the greatest discrepancies of the absolute abundance values from the two systems. Notice, for example, in figure 2.4a

the MOCNESS yielded hydromedusae abundances ranging from 0 to $5x10^{-3}$ individuals mL^{-1} while the O-cam produced estimates ranging from 0 to 1.2 individuals mL^{-1}. The discrepancy for appendicularians (Fig. 2.4b) was much smaller, though the nets produced abundances ten times smaller than the estimates from the O-cam. Notice also that in the case of the hydromedusae, variations at low abundances in the MOCNESS samples were not reflected in the O-Cam data. Recall that these data were obtained from samples and images taken from 0 to 500 meters depth; while the O-Cam was vertically profiled, the MOCNESS was towed obliquely. This means that if there were hydromedusae (which we know can be present in low abundances at depth and would only occasionally imaged by our camera) they were more likely to be captured by a system that filters several hundreds of cubic meters than imaged by a system whose imaged volume is 106 mL per frame. The low values yielded by the nets thus indicate underestimation by the MOCNESS – the non-destructive imaging system yields more accurate abundance estimates of delicate gelatinous organisms. Nets towed at 3-5 knots tend to damage fragile organisms, in particular those in the size range imaged by the O-Cam (< 2 cm in bell diameter). The discrepancy of cnidarian abundances between net and imaging systems has been observed previously. For example, Remsen and co-workers (2004) reported a 1200% abundance underestimation of cnidarian abundances by nets in comparison to the abundance estimates obtained using their imaging system. The discrepancy in the hydromedusae abundance estimates between the O-Cam and the MOCNESS in the present work is consistent with the latter report.

The apparent underestimation of appendicularians by the MOCNESS may also be real, and was previously observed in a comparison exercise between bongo nets and the optical plankton counter (OPC; González-Quirós and Checkley, 2006). In addition, Remsen et al. (2004) found that nets underestimated apperdicularians by 300% in comparison to the camera system. Hydromedusae and appendicularians are fragile and can be subjected to damage not only during net tows, but also during size fractionation while preparing the samples to be processed on the ZOOSCAN. Jellies will become indistinguishable to the automatic classification system of the scanner, and appendicularians will not be correctly identified if their trunk is separated from the tail. Such damage may explain the apparent underestimation of appendicularian abundances by the MOCNESS.

Moderate correlations of MOCNESS and O-Cam-derived abundances were observed for all copepods combined (Fig. 2.4e) and weak, but still positive correlations were observed for cyclopoid and calanoid copepods (Fig. 2.4c, d). As expected calanoid copepods and all copepods combined showed the greatest agreement between both techniques in term of absolute abundances. Within copepods, cyclopoids showed a greater departure from the 1:1 line, suggesting this group was underestimated (overestimated) by the MOCNESS samples (O-Cam image data). This result is consistent with the work of Galliene and Robins (2001), who reported cyclopoid copepods being under-represented in historical data worldwide due to current net sampling practices.

The MOCNESS and O-Cam abundance estimates for euphausiids were positively correlated (r=0.525; Fig. 2.4f). Euphausiids are highly motile and avoidance has been observed even for high-speed samplers with large collection areas such as the MOCNESS, (e.g., Wiebe et al., 2013). However, these authors have shown that using LED lights mounted on the net improves the capture of euphausiids by a factor of 4.5 (nighttime) or 11 (daytime) compared to a net without lights. It is possible that the O-Cam LEDs contributed to increased imaging of euphausiids.

Ideally for this comparison the O-Cam would have been mounted on the MOCNESS frame; unfortunately, at the time of the CalEchoes cruise the O-Cam was not designed for towing. The differences observed in this comparison analysis contain inherent methodological errors due the spatial and temporal separation in the deployment of the systems. We tried to minimize this by integrating the O-Cam-derived estimates over the same depth strata sampled by each net. Further errors have presumably been introduced by the processing methodology using the ZOOSCAN. However, the positive (albeit weak in some instances) relationship observed between the abundance estimates from the two systems supports the notion that the O-Cam can yield accurate estimates of zooplankton relative abundances.

2.3.2. Depth profiles from the CTD, PLIF and O-Cam

The free-falling nature of the FIDO platform and the high sampling rate of the sensors yielded a fine-scale (cm) distribution of physical and biological data, uncontaminated by motions due to ship heave. The sampling method permitted us to

quantify the profiles of salinity and temperature (Fig. 2.5a, b) as well as fluorescence intensity (Fig. 2.5c), fluorescence and scattering particle concentrations (Fig. 2.5d,e), and the abundance of five zooplankton groups: hydromedusae, appendicularians, calanoid copepods, cyclopoid copepods, and euphausiids (Fig. 2.5f-j). It is clear that the vertical distributions of these properties vary in time, presumably due to factors such as internal waves and the internal tide. These purely advective effects can be removed by plotting the data with density as the vertical coordinate, rather than depth, as we show below.

2.3.3. CTD, PLIF and O-Cam *non-normalized* profiles in density coordinates

The depth displacement evident in the fluorescence intensity profiles (Fig. 2.5c) followed the displacement of isotherms (Fig. 2.5b) – temperature being the main determinant of density in this region. This suggested that density might explain the vertical variability of biological data better than depth. The density-binned data (from now on referred to as density coordinates) shown in figure 2.6 clearly show that the low-frequency vertical displacements among profiles disappeared when plotted vs. density, confirming that fluorescence intensity, for example, followed isopycnals rather than pressure surfaces. Not obvious in figures 2.5 and 2.6 are vertical displacements of the fluorescent particle concentration profiles. This is because profile 6_3 showed a significantly higher signal than the profiles before and after. We can remove such inter-profile variability by normalizing each profile by its maximum

value. This gives normalized relative vertical distributions of each variable, where the variable now ranges between zero and one in each profile.

2.3.4. CTD, PLIF and O-Cam *normalized* profiles in density coordinates

Once normalized data were plotted on density coordinates, the patterns became strikingly evident (Fig. 2.7). Two fluorescence maxima were identified: a bulk fluorescence maximum (CMAX) and a fluorescent particle concentration maximum (FPCMAX) – the latter being located around the lower boundary of the former (Fig. 2.7c,d). The scattering particle concentration distributions were found to overlap both fluorescence maxima but with no consistent pattern (Fig. 2.7c). As we show below, our data suggested that the FPCMAX (bounded by the black on white lines in Fig. 2.7) and not the CMAX seemed to be driving the observed zooplankton distributions; thus subsequent analyses were carried out using the depth of the FPCMAX.

No zooplankton taxa were found exclusively within the FPCMAX. Hydromedusae showed some overlap but were mostly located above the FPCMAX (Fig. 2.7f). Similarly, appendicularians and calanoid copepods (Fig. 2.7g, h) were mainly located above the FPCMAX. Cyclopoid copepods were mainly concentrated at the lower boundary of the FPCMAX (Fig. 2.7i). Euphausiids showed a more even vertical distribution, with some located above the FPCMAX at the beginning of the cruise and within it towards the end (Fig. 2.7j).

2.3.5. Canonical Profiles and Spearman rank correlation analysis

Canonical profiles were formed by averaging the individual normalized profiles in density coordinates. These time-integrated profiles for each variable clearly show how zooplankton were distributed with respect to the CMAX and FPCMAX (Fig. 2.8). The Spearman rank correlation analysis (Table III) quantified the correlations of pairs of the canonical vertical distributions observed in the normalized density coordinate plots (Fig. 2.7), which we synthesized into a vertical distribution-interaction schematic (Fig. 2.9). Not surprisingly, correlation coefficients showed that fluorescence intensity was positively correlated with fluorescent particle concentration. All zooplankton groups showed statistically significant correlations with scattering particles – however cyclopoid copepods were the only group showing a negative correlation. Unexpectedly, cyclopoid copepods were negatively correlated with the other zooplankton groups, although statistically significant (negative) values were only found between this group and calanoid copepods and appendicularians. Calanoid copepods showed no significant correlation with fluorescence intensity, but a strong negative correlation with fluorescent particles and a positive correlation with scattering particles. Cyclopoid copepods showed the opposite – a statistically significant positive correlation with fluorescent particles and a weak negative correlation with scattering particles. Hydromedusae showed positive statistically significant correlations with fluorescence, scattering particles and calanoid copepods. Appendicularians also showed positive correlations with scattering particles, calanoids and hydromedusae. The only non-significant correlations for euphausiids were those

with fluorescence particle concentration and cyclopoid copepods; the remaining correlations were significant and positive.

In the Southern California Bight the dynamics of the chlorophyll maximum (CMAX) has been extensively studied. It is well known, for example, that the depth of the CMAX changes predictably with season (Napp, 1987) though vertical advection can cause vertical motions of the maxima at shorter time scales (Cullen et al., 1983). The depth of the CMAX (fluorescence intensity maximum) in the present work agrees with historical observations for the highly stratified summer season for a coastal location (Napp, 1987). No particulate organic carbon (POC) was measured in the present work, however, the scattering particle distributions (Fig. 2.8b) indicate that the POC maximum is likely above the CMAX, as is often observed (Napp, 1987). This can also be seen in figure 2.7e, where scattering particle concentrations were found to overlap the upper boundary of the CMAX.

Interestingly, the fluorescent particle concentration maximum (FPCMAX) is located below the CMAX. While the fluorescent particle concentration cannot be interpreted as biomass, it certainly indicates the abundance of large fluorescent particles (large chains, aggregates, etc.), while the bulk fluorescence includes fluorescence from smaller organisms, including cyanobacteria. The vertical offset of CMAX and FPCMAX is indicative of a dominance by smaller phytoplankton in the waters above the FPCMAX, and an increased relative abundance of large fluorescent particles below CMAX.

The location of the cyclopoid copepods below the CMAX and FPCMAX may have important implications for carbon export. Whether cyclopoid copepods penetrate the CMAX, or get above it during other seasons cannot be inferred from the present data. For these summer data, however, the cyclopoid location suggests that their fecal pellets may have a higher chance than other organisms' fecal material to reach deeper into the ocean, escaping remineralization higher in the euphotic zone, and positively influencing carbon export. Their location below the CMAX and FPCMAX, but also below the seasonal pycnocline may further enhance their fecal pellet flux. For example, it has been shown that sinking particles slow down when they interact with sharp density gradients (Prairie et al., 2013) – a process known as 'ballasting' (Ploug et al., 2008) – making such particles more vulnerable to remineralization in surface waters. The fact that cyclopoid copepod fecal pellets will not pass through such sharp gradients suggests that carbon export during the strongly stratified water column may be quite efficient in the summer in the SCB.

Cyclopoid copepods observed in the present study were mostly *Oithona* spp. Galliene and Robins (2001) reported that these cosmopolitan copepods are under-represented in historical data sets in the 200-600 μm net mesozooplankton size fraction. The cyclopoid copepods imaged by the O-Cam fall in this range; despite the 202 μm mesh size of the MOCNESS used to test the quantitative capabilities of the O-Cam, it is clear that the nets underestimated their abundances relative to the O-Cam (Fig. 2.4). This suggests that the contribution of *Oithona* spp. to carbon export might also be underestimated.

Oithona spp. copepods are known to be ambush-feeding (also known as "sit and wait") predators (Paffenhöfer, 1993; Kiørboe et al., 2015), feeding mainly on small (18-30 μm) ciliates and flagellates (Saiz et al., 2014). The exceptional sensory system of *Oithona* spp. to detect hydromechanical signals from their prey and their infrequent relocation jumps (Pafenhöffer, 1993) may confer them the additional benefit of detecting and escaping from their predators. This may explain the observed distribution of cyclopoid copepods below the location of potential predators such as calanoid copepods and hydromedusae.

The calanoid copepod distribution was collocated with the appendicularians; they both overlapped those of the hydromedusae in the upper region of the FPCMAX. Calanoid copepods can shift their feeding from detritivory to herbivory to carnivory (Landry, 1981), and some calanoids are known to feed on appendicularians and appendicularian eggs (Sommer et al., 2003; López-Urrutia, 2004). During a season when food might be limiting (such as the summer), calanoid copepods must maximize their utilization of available food resources. This may explain their spatial correlation with both appendicularians and scattering particles, while risking predation by hydromedusae.

Hydromedusae where observed within the CMAX and above the FPCMAX (Fig. 2.8). These organisms are known to feed on copepods and appendicularians (e.g., Fulton and Wear, 1985; Costello and Colin, 2002). Furthermore, Costello and Colin (2002) present evidence that different hydromedusae can co-exist by exploiting different resources. In our data the hydromedusae group was composed of at least 5

different body types, and most likely different species, all present in every FIDO-Φ-O-Cam profile. Costello and Colin (2002) noted that while some hydromedusae prefer crustaceans, others more effectively exploit appendicularians. The co-location of these hydromedusae predators with respect to these potential crustacean and appendicularian prey may explain the vertical distributions observed here.

Appendicularians were observed in high densities in shallower waters (Fig. 2.8). Similar observations were made by Alldredge (1982) in a location close to our sampling area, who showed that the shallow water aggregation of *Oikopleura longicaudata* was due to a spawning event – she observed sexually mature individuals (without "houses" or free swimming), as well as juveniles and eggs. She also reported that these appendicularians became highly aggregated in windrows, a phenomenon that may have helped to increase encounter rates. Our present observations included numerous free-swimming, sexually mature appendicularians mainly from the genus *Oikopleura*. This evidence suggests that we most likely observed a spawning event, which provides further explanation for the observed co-location (and high correlation) with their predators: calanoid copepods and hydromedusae.

2.4. Conclusions

This work describes the fine-scale vertical distributions of five zooplankton taxa in relation to fluorescent particle distributions, acquired using two *in situ* optical systems –PLIF and O-Cam. The fine-scale resolution of our biological and hydrographic data allowed us to show that water density explained much of the

temporal variability of the vertical distributions of both zooplankton and fluorescent particles. Such observations would not have been possible using net sampling techniques, which tend to average away such fine structures. The location of each zooplankton group in relation to the fluorescent particle distribution and with respect to each other was explained by invoking predator-prey interactions. Cyclopoid copepods, for example tended to avoid areas where their predators were present in large abundances, while calanoid copepods tended to be present in areas where a suitable assemblage of prey (appendicularians and marine snow aggregates) was present – in spite of being exposed to higher abundances of their own predators: hydromedusae. The observed shallow distributions of appendicularians suggested that we observed a reproduction event. The observations made here present a very dynamic ecological picture. Future observations using these tools should include daylight deployments and more frequent sampling to observe diel vertical distributions. Extending these observations to other seasons would also help us understand whether the location of cyclopoid copepods beneath both the CMAX and FPCMAX is a recurrent phenomenon. The latter is particularly important, for it may have important effects on carbon export via fecal pellet production below the seasonal thermocline.

2.5 Acknowledgements

I would like to thank Jennifer Prairie for processing the PLIF image data. I would like to thank UC Ship Funds for funding the CalEchoes cruise and the CCE-LTER program for the generous support to conduct MOCNESS tows and for

providing materials and equipment necessary to process the zooplankton samples. Jesse Powell helped me sorting zooplankton net samples –thank you! I am also indebted to the members, past and present, of the Jaffe Lab who worked hard in setting up the FIDO-Φ platform. The fieldwork wouldn't have been possible without the help of the captains and crew of the R/V New Horizon and R/V Melville.

Chapter 2, in full, is currently being prepared for submission for publication of the material. Briseño-Avena, C., Franks, P.J.S., and Jaffe, J.S. The dissertation author was the primary investigator and author of this paper.

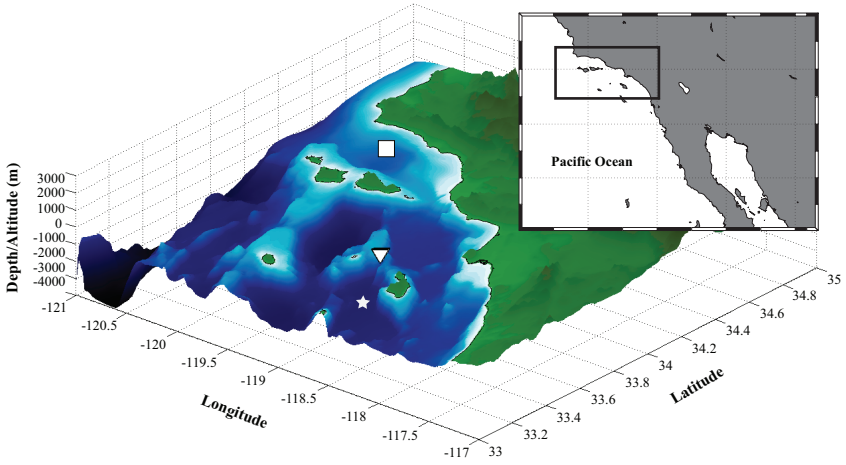

Figure 2.1. Bathymetry of the study region (area bounded by the solid black rectangle in the inset map). White square indicates the general location of the Santa Barbara Channel sampling sites for the CalEchoes cruise aboard R/V Melville from September 26 - October 1, 2010. Inverted triangle represents the site occupied during the FIDO-Φ-O-cam cruise aboard R/V New Horizon from August 18-23, 2011. White star indicates the location of the Santa Catalina Basin.

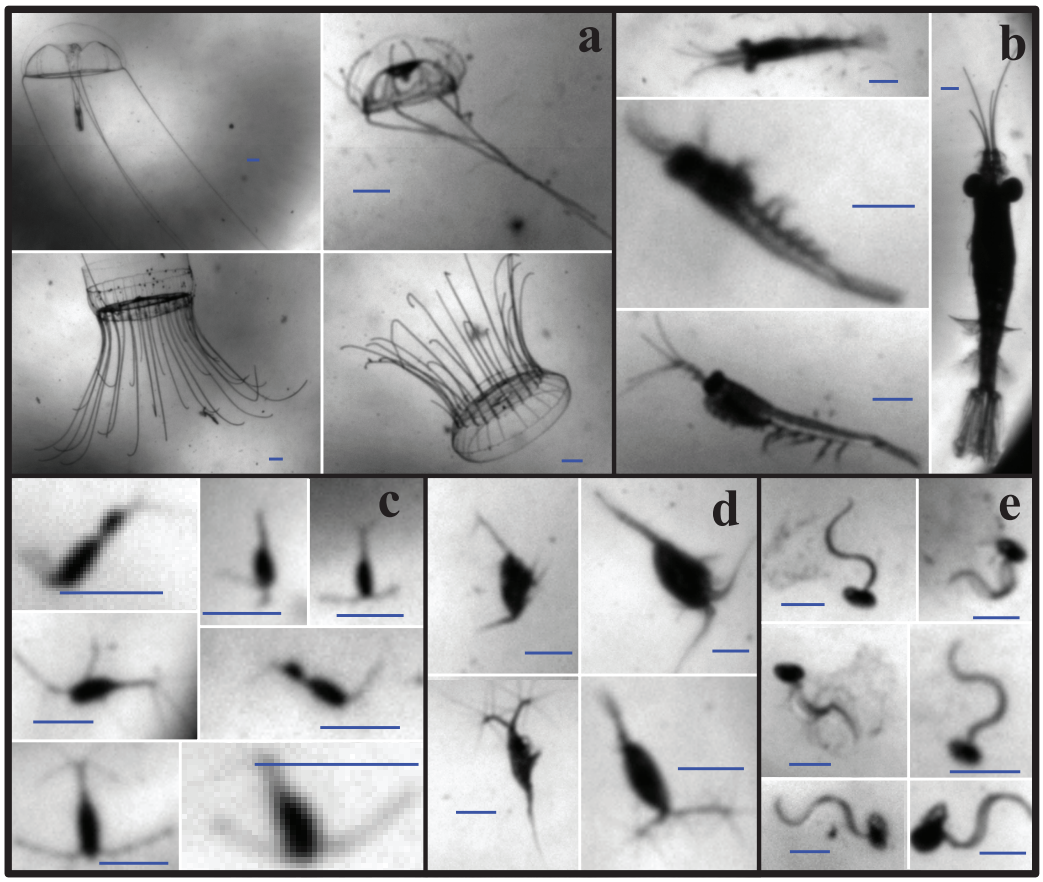

Figure 2.2. Examples of zooplankton images from the O-Cam system. a) Hydromedusae; b) Euphausiids; c) Cyclopoid copepods; d) Calanoid copepods; e) Appendicularians. All the scale bars are 1 mm long.

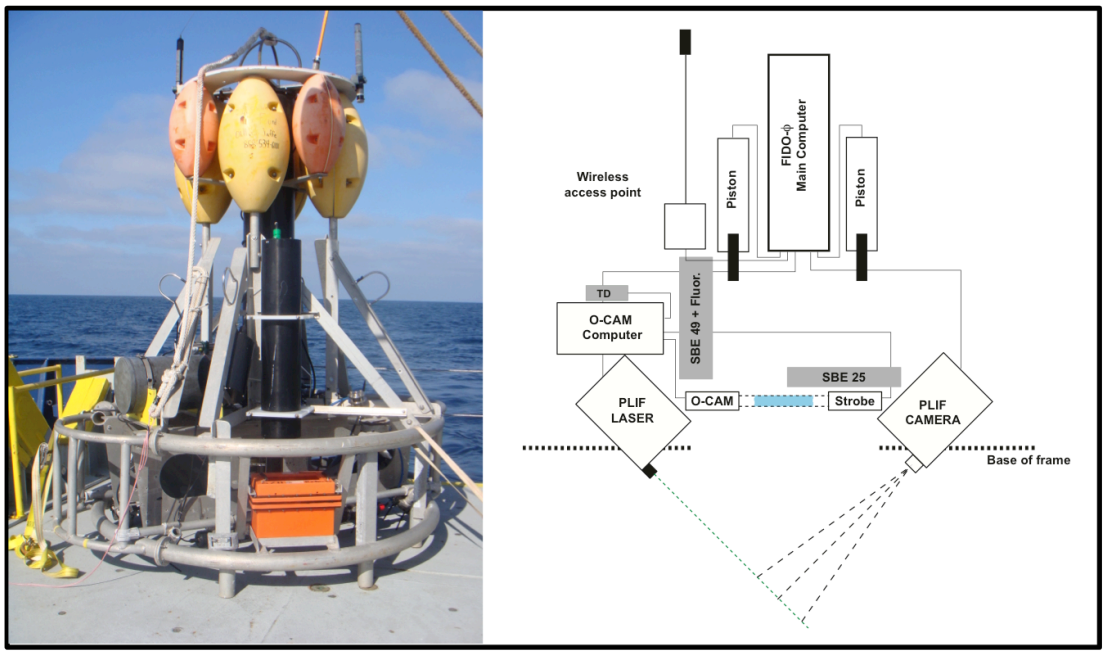

Figure 2.3. a) FIDO-ϕ-O-Cam on the deck of R/V *New Horizon* during the August 2011cruise. b) Modified schematic from Prairie et al. (2011) to reflect the sensors used for this work. The relative position of the imaging volumes for the PLIF and O-Cam systems are shown, as well as the location of the imaging volumes with respect to CTD (SBE 25 and SBE 49) and TP sensors.

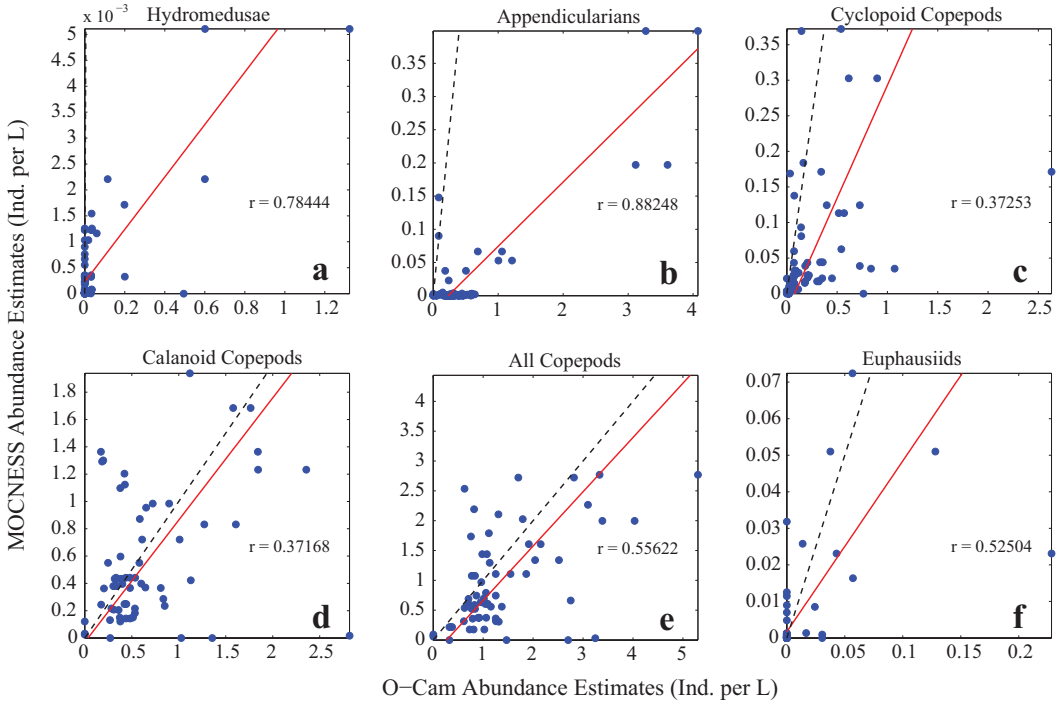

Figure 2.4. Type-II correlation analyses between O-Cam- and MOCNESS-derived zooplankton abundances (Individuals L^{-1}) sampled during the CalEchoes cruise in the Santa Barbara Basin from 26 September-1 October, 2010. Blue dots represent individual observations. Red solid lines represent the regression lines derived from the analysis. Black dashed lines represent the 1:1 relationship. Correlation coefficients (r) are indicated in each panel. a) Hydromedusae; b) Appendicularians; c) Cyclopoid copepods; d) Calanoid copepods; e) All copepods; f) Euphausiids.

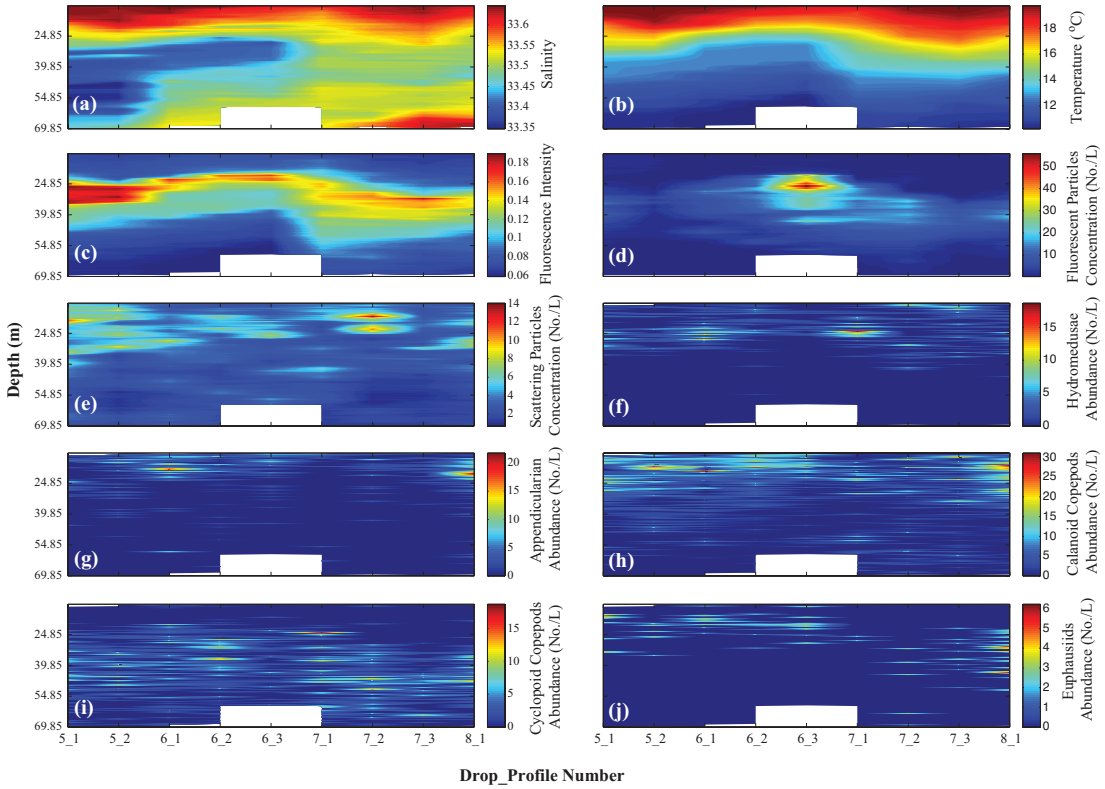

Figure 2.5. Depth-time distributions of physical and non-normalized biological data. a) Salinity; b) Temperature (°C); c) Fluorescence Intensity (SBE 25 + fluorometer); d) Planar Laser Imaging Fluorometer (PLIF) fluorescent particle concentration (Numbers/L); e) PLIF-derived scattering particle concentration (Numbers/L). Panels f through j represent O-Cam zooplankton abundances (Numbers/L): f) Hydromedusae; g) Appendicularians; h) Calanoid copepods; i) Cyclopod copepods; and j) Euphausiids.

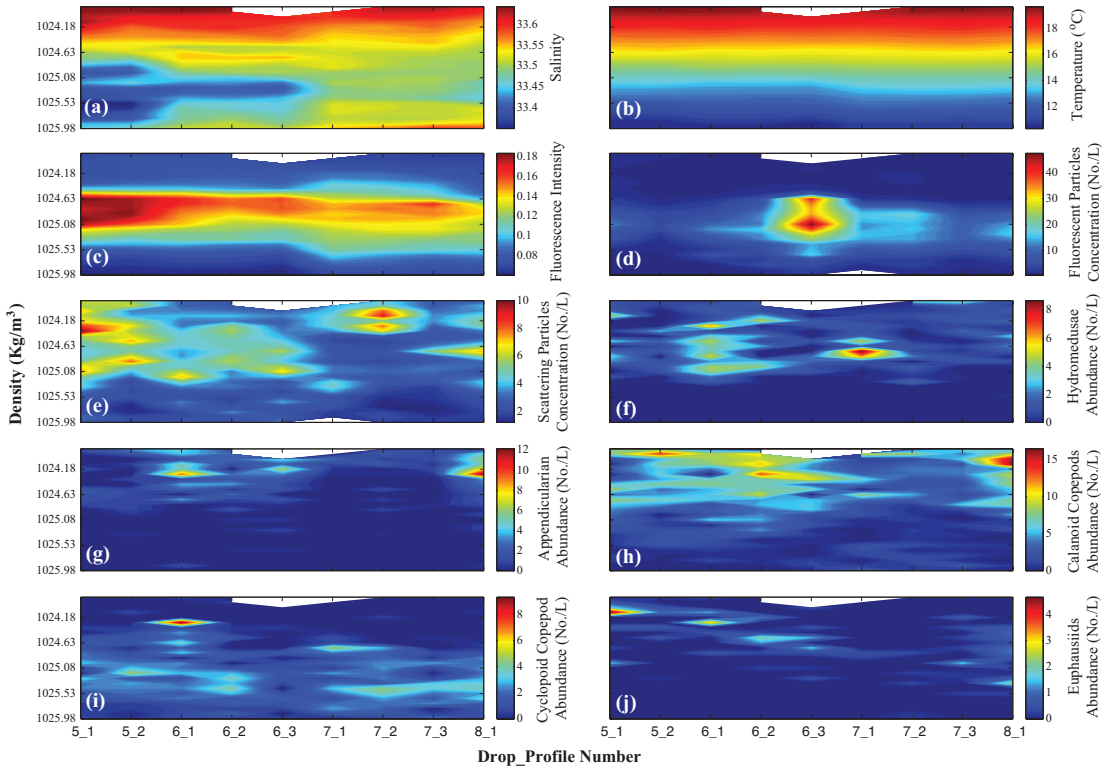

Figure 2.6. Density-time distributions of physical and non-normalized biological data. a) Salinity; b) Temperature (°C); c) Fluorescence Intensity (SBE 25 + fluorometer); d) Planar Laser Imaging Fluorometer (PLIF) fluorescent particle concentration (Numbers/L); e) PLIF-derived scattering particle concentration (Numbers/L). Panels f through j represent O-Cam zooplankton abundance (Numbers/L) data: f) Hydromedusae; g) Appendicularians; h) Calanoid copepods; i) Cyclopod copepods; and j) Euphausiids.

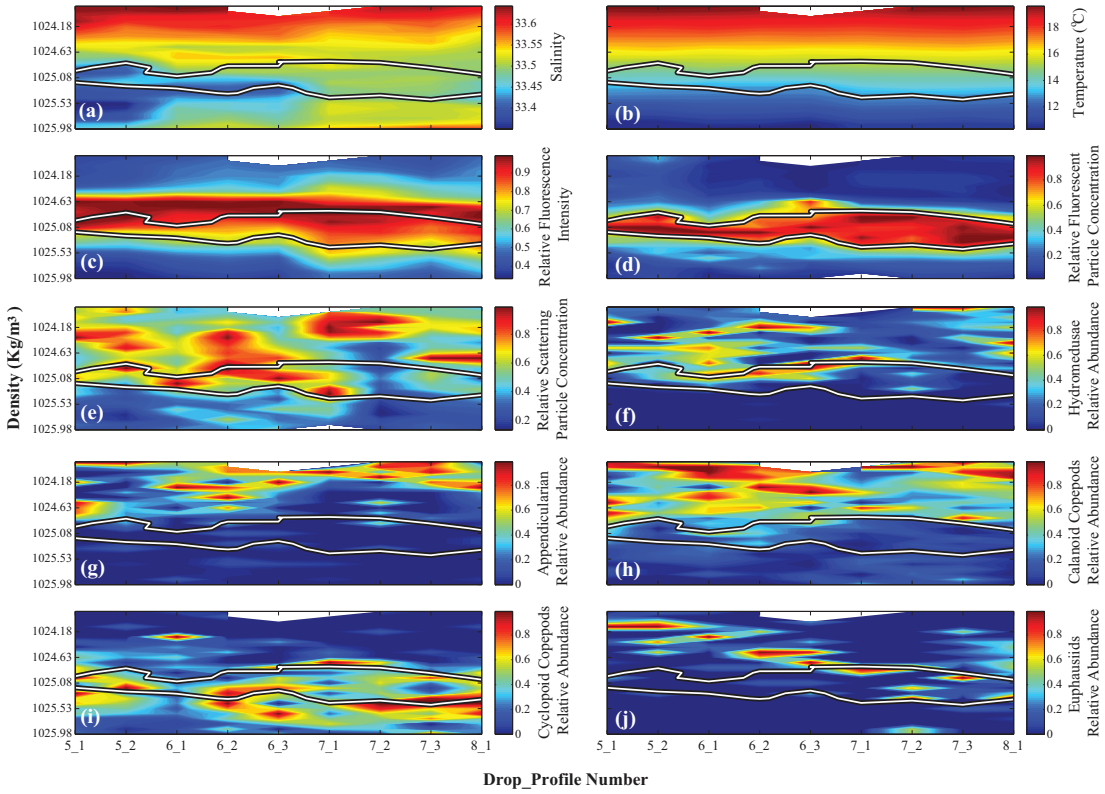

Figure 2.7. Density-time distributions of physical and normalized biological data. a) Salinity; b) Temperature (°C); c) Fluorescence Intensity (SBE 25 + fluorometer); d) Planar Laser Imaging Fluorometer (PLIF) relative fluorescent particle concentration ; e) PLIF-derived relative scattering particle concentration. Panels f through j represent O-Cam zooplankton relative abundance data: f) Hydromedusae; g) Appendicularians; h) Calanoid copepods; i) Cyclopod copepods; and j) Euphausiids. White-on-black lines superimposed on panels represent the 0.7 relative fluorescent particle concentration contour (panel d).

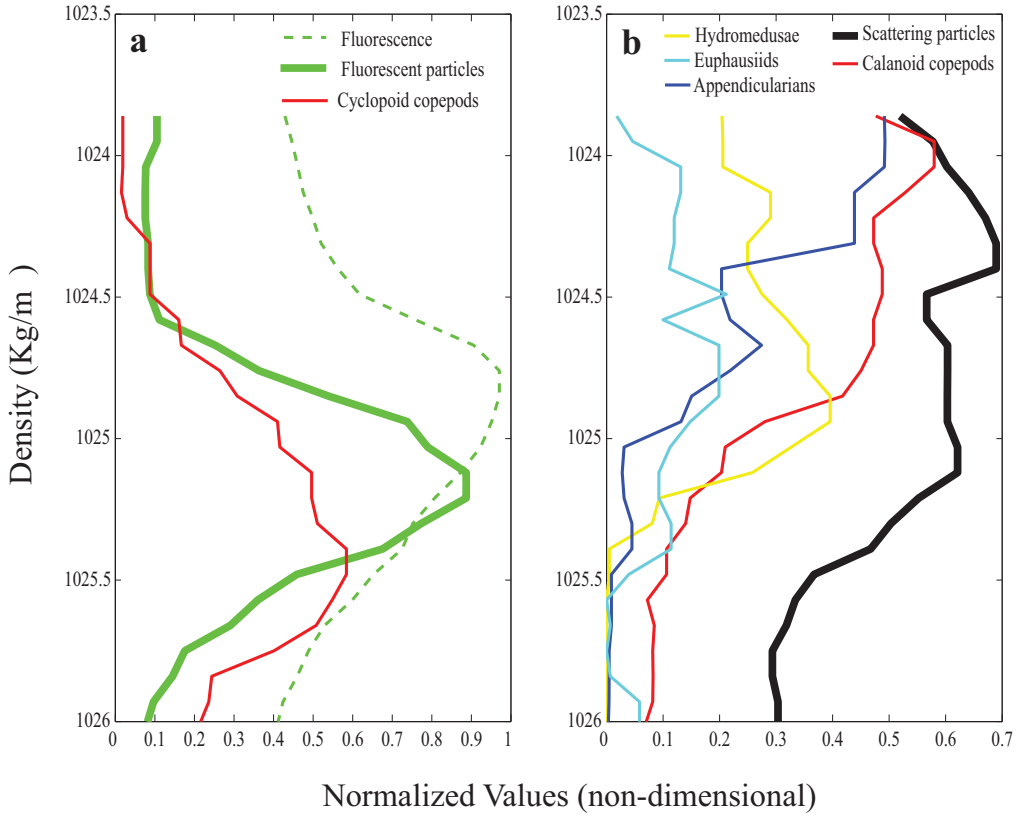

Figure 2.8. Canonical profiles (integrated over time in density space) for a) fluorescence intensity, fluorescent particle concentration, and cyclopoid copepods; b) hydromedusae, euphausiids, appendicularians, scattering particles and calanoid copepods.

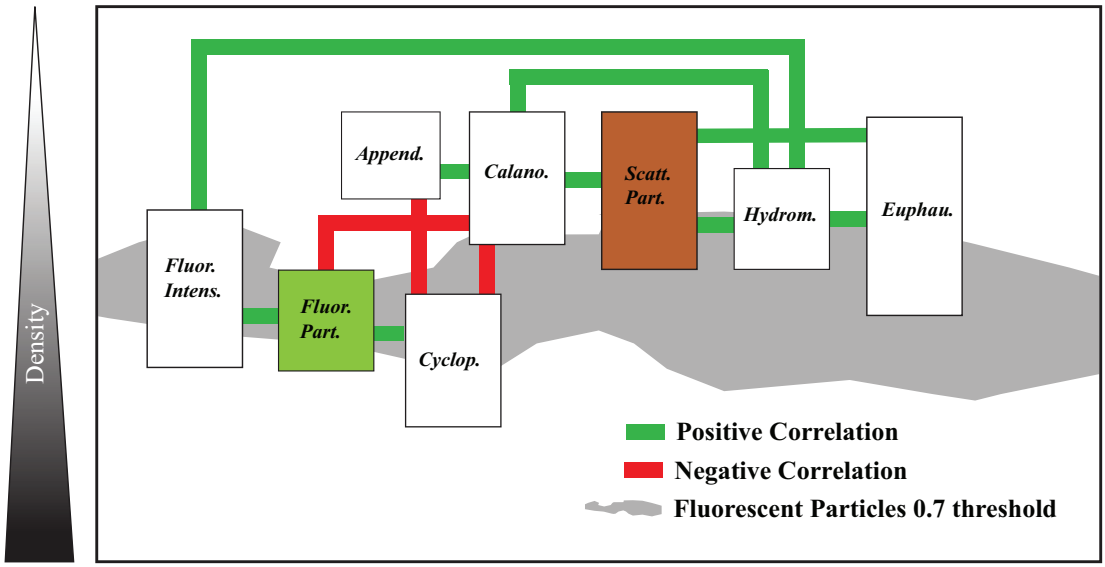

Figure 2.9. Schematic representation of the vertical (versus density) distributions of biological variables and their statistically significant correlations from the Spearman Rank correlation analysis. Gray patch is the 0.7 fluorescent particle concentration threshold (from Fig. 2.7d). Green lines connecting the boxes indicate positive correlations while red lines represent negative correlations.

Table 2.1. Sampling locations and deployment sequence of O-Cam vertical profiles and MOCNESS oblique tows (grayed out rows) used in the present analysis.

Platform	Tow/ profile	Date (local)	Time (local)	Deployment Location (Lat. N, Lon. W)	Recovery Location (Lat. N, Lon. W)	Sampled Depth Range (m)
MOCNESS	2	26-Sep-2010	01:42	34.32, 120.02	34.28, 120.05	0-397.1
O-Cam	1	26-Sep-2010	21:26	34.29, 120.04	N/A	5.9-481.74
MOCNESS	3	27-Sep-2010	11:02	34.29, 120.04	34.33, 119.97	0-497.9
MOCNESS	4	27-Sep-2010	21:35	34.27, 119.97	34.25, 119.91	0-464.7
O-Cam	2	28-Sep-2010	02:39	34.29, 120.11	N/A	2.03-503.34
O-Cam	5	29-Sep-2010	01:57	34.26, 120.96	N/A	2.35-502.06
MOCNESS	8	30-Sep-2010	05:25	34.29, 120.02	34.26, 119.97	0-497.0
O-Cam	7	30-Sep-2010	06:26	34.29, 119.99	N/A	2.00-503.37
O-Cam	8	30-Sep-2010	21:00	34.29, 120.04	N/A	1.83-502.21
MOCNESS	9	01-Oct-2010	00:45	34.30, 120.02	34.29, -120.09	0-497.4
O-Cam	9	01-Oct-2010	07:39	34.26, 119.96	N/A	2.41-502.16

Table 2.2. FIDO-ϕ-O-cam drop_profile information.

Drop_profile Number	Location of Deployment	Deployment date and time (local)	Usable Depth Range (m)	PLIF: total images*	O-cam: total images
05_1	33.57 N 118.91 W	21-Aug-2011, 21:44	10-70	1,169	589
05_2	33.56 N 118.91 W	21-Aug-2011, 22:15	10-70	1,228	654
06_1	33.55 N 118.91 W	22-Aug-2011, 02:14	10-70	1,343	672
06_2	33.55 N 118.92 W	22-Aug-2011, 03:03	10-70	1,874	971
06_3	33.56 N 118.93 W	22-Aug-2011, 04:02	10-60	1,138	610
07_1	33.57 N 118.92 W	22-Aug-2011, 20:33	10-70	1,147	584
07_2	33.57 N 118.92 W	22-Aug-2011, 21:04	10-70	1,221	649
07_3	33.57 N 118.92 W	22-Aug-2011, 21:32	10-70	1,412	750
08_1	33.56 N 118.93 W	23-Aug-2011, 00:26	10-70	1,285	637

* The PLIF system samples at 2 Hz –the numbers given here include both, fluorescent and scattering particle images.

Table 2.3. Spearman rank correlation coefficients between biological parameters. Gray values represent non-significant coefficients. Asterisks indicate statistically significant ($p_{\alpha=0.05}$ <0.05) coefficients. Values in regular black values indicate positive correlations and black bold values represent negative correlations.

	Fluor. Intens.	*Fluor. Part.*	*Scatt. Part.*	*Cyclop.*	*Calano.*	*Hydrom.*	*Append.*	*Euphau.*
Fluor. Intens.	1	0.7253*	0.3817	0.4930	0.0131	0.6445*	0.0260	0.5019*
Fluor. Part.		1	-0.1378	0.8226*	**-0.4289***	0.0840	-0.3819	-0.0739
Scatt. Part.			1	**-0.4169***	0.7293*	0.7993*	0.6741*	0.6565*
Cyclop.				1	**-0.7566***	-0.3057	**-0.6963***	-0.2864
Calano.					1	0.6334*	0.9321*	0.5626*
Hydrom.						1	0.6037*	0.7990*
Append.							1	0.5302*
Euphau.								1

2.6 References

Alldredge, A.L. 1982. Aggregation of spawning appendicularians in surface windrows. Bulletin of Marine Science, 32: 250-254.

Alldredge, A.L., Robison, B.H., Fleminger, A., Torres, J.J., King, J.M., and Mammer, W.M. 1984. Direct sampling and *in situ* observation of a persistent copepod aggregation in the mesopelagic zone of the Santa Barbara Basin. Marine Biology, 80: 75-81.

Benfield, M.C., Davis, C.S., Wiebe, P.H., Gallager, S.M., Lough, R. G., and Copley, N. J. 1996. Video Plankton Recorder estimates of copepod, pteropod and larvacean distributions from a stratified region of Georges Bank with comparative measurements from a MOCNESS sampler. Deep-Sea Research II, 43: 1925-1945.

Bollens, S.M., Frost, B. W., and Lin, T.S. 1992. Recruitment, growth, and diel vertical migration of *Euphausia pacifica* in a temperate fjord. Marine Biology, 14: 219-228.

Briseño-Avena, C., Roberts, P.L.D., Franks, P.J.S., and Jaffe, J.S. 2015. ZOOPS-O^2: A broadband echosounder with coordinated stereo optical imaging for observing plankton in situ. Methods in Oceanography, 12: 36-54.

Castro, L.R., Bernal, P.A., and Gonzalez, H.E. 1991. Vertical distribution of copepods and the utilization of the chlorophyll *a* layer within Concepcion Bay, Chile. Estuarine, Coastal and Shelf Science, 32: 243-256.

Costello, J.H., and Colin, S.P. 2002. Prey resource use by coexistent hydromedusae from Friday Harbor, Washington. Limnology and Oceanography, 47: 934-942.

Cowen, R. K., and Guigand, C. M. 2008. *In situ* ichthyoplankton imaging system (*IS*IIS): system design and preliminary results. Limnology and Oceanography: Methods, 6: 126-132.

Cullen, J.J. 2015. Subsurface chlorophyll maximum layers: Enduring enigma or mystery solved? Annual Review of Marine Science, 7: 207-239.

Cullen, J.J., and Eppley, R.W. 1981. Chlorophyll maximum layers of the Southern California Bight and possible mechanisms of their formation and maintenance. Oceanologica Acta, 4: 23-32.

Cullen, J.J., Stewart, E., Renger, E., Eppley, R.W., and Winant, C.D. 1983. Vertical motion of the thermocline, nitrcline and chlorophyll maximum layers in

relation to currents on the Southern California Shelf. Journal of Marine Research, 41: 239-262.

Davis, C.S., Gallager, S.M., Marra, M., and Sewart, W. K. 1996. Rapid visualization of plankton abundance and taxonomic composition using the Video Plankton Recorder. Deep-Sea Research II, 43: 1947-1970.

de Robertis, A., Jaffe, J.S. and Ohman, M.D. 2000. Size-dependent visual predation risk and the timing of vertical migration in zooplankton. Limnology and Oceanography, 45: 1838-1844.

Fiedler, P.C. 1983. Fine-scale patterns in the coastal epiplankton off southern California. Journal of Plankton Research, 5: 865-879.

Franks, P.J.S., and Jaffe, J.S. 2001. Microscale distributions of phytoplankton: initial results from a two-dimensional imaging fluorometer, OSST. Marine Ecology Progress Series, 220: 59-72.

Franks, P.J.S., and Jaffe, J.S. 2008. Microscale variability in the distributions of large fluorescent particles observed *in situ* with a planar laser imaging fluorometer. Journal of Marine Systems, 69: 254-270.

Frost, B. W. 1972. Effects of size and concentration of food particles on the feeding behavior of the marine planktonic copepod *Calanus pacificus*. Limnology and Oceanography, 17: 805-815.

Fulton, R.S., and Wear, R.G. 1985. Predatory feeding of the nydromedusae *Obelia geniculata* and *Phialella quadrata*. Marine Biology, 87: 47-54.

Galliene, C.P., and Robins, D.B. 2001. Is *Oithona* the most important copepod in the world's oceans? Journal of Plankton Research, 23: 1421-1432.

González-Quirós, R., and Checkley, D.M., Jr. 2006. Occurrence of fragile particles from optical plankton counters used *in situ* and to analyze net samples collected simultaneously. Journal of Geophysical Research, 111, C05S06.

Gorsky, G., Ohman, M.D., Picheral, M., Gasparini, S., Stemmann, L., Romagnan, B., Cawood, A., Pesant, S., García-Comas, C. and Prejger, F. 2010. Digital zooplankton image analysis using the ZooScan integrated system. Journal of Plankton Research, 32: 285-303.

Greer, A.T., Cowen, R.K., Guigand, C.M., McManus, M.A., Sevadjian, J.C., and Timmerman, A.H.V. 2013. Relationships between phytoplankton thin layers

and the fine-scale vertical distributions of two trophic levels of zooplankton. Journal of Plankton Research, 35: 939-956.

Herman, A.W. Vertical patterns of copepods, chlorophyll, and production in northern Baffin Bay. Limnology and Oceanography, 28: 709-719.

Herman, A.W., Beanlands, B., and Phillips, E.F. 2004. The next generation of Optical Plankton Counter: the Laser-OPC. Journal of Plankton Research, 26: 1135-1145.

Herman, A.W., Sameoto, D.D., and Longhurst, A.R. 1981. Vertical and horizontal distribution patterns of copepods near the shelf break south of Nova Scotia. Canadian Journal of Fisheries and Aquatic Science, 38: 1065-1076.

Hirche, H. 1996. Diapause in the marine copepod, *Calanus finmarchicus* –A review. Ophelia, 44: 129-143.

Holliday, D.V., Pieper, R.E., and Kleppel, G.S. 1989. Determination of zooplankton size and distribution with multifrequency acoustic technology. ICES Journal of Marine Sciences, 46: 52-61.

Holliland, P.B., Ahlbeck, I., Westlung, E. and Hansson, S. 2012. Ontogenetic and seasonal changes in diel vertical migration amplitude of the calanoid copepods *Eurytemora affinis* and *Acartia* spp. in a coastal area of the northern Baltic proper. Journal of Plankton Research, 0: 1-10.

Jacobsen, H.P., and Norrbin, M.F. 2009. Fine-scale layer of hydromedusae is revealed by video plankton recorder (VPR) in a semi-enclosed bay in northern Norway. Marine Ecology Progress Series, 380: 129-135.

Jaffe, J.S., Franks, P.J.S., and Leising, A.W. 1998. Simultaneous imaging of phytoplankton and zooplankton distributions. Oceanography, 11: 24-29.

Johnson, C.L, and Checkley, D.M. 2004. Vertical distribution of diapausing *Calanus pacificus* (Copepoda) and implications for transport in the California undercurrent. Progress in Oceanogrphy, 62: 1-13.

Kiørboe, T., Jian, H., and Colin, S.P. 2015. Danger of zooplankton feeding: the fluid signal generated by ambush-feeding copepods. Proceedings of the Royal Society B, 277: 3229-3237.

Lampert, W. 1989. The adaptive significance of diel vertical migration of zooplankton. Functional Ecology, 3: 21-27.

Landry, M.R. 1981. Switching between herbivory and carnivory by the planktonic marine copepod *Calanus pacificus*. Marine Biology, 65: 77-82.

Loose, C.T., and Dawidowicz, P. 1994. Trade-Offs in diel vertical migration by zooplankton: the costs of predator avoidance. Ecology, 75: 2255-2263.

López-Urrutia, A., Harris, R.P., and Smith, T. 2004. Predation by calanoid copepods on the appendicularian *Oikopleura dioica*, Limnology and Oceanography, 49: 303-307.

Lorenzen, C. J. 1966. A method for the continuous measurement of *in vivo* chlorophyll concentration. Deep-Sea Research, 1966, 13: 223-227.

Masson, S. Pinel-Alloul B., Méthot, G., and Richard, N. 2004. Comparison of nets and pump sampling gears to assess zooplankton vertical distributions in stratified lakes. Journal of Plankton Research, 26: 1199-1206.

Napp, J.M. 1987. Primary productivity maxima in the Southern California Bight: distribution, predicted depth and nutritional content. Oceanologica Acta, 10: 329-337.

Napp, J. M., Brooks, E.R., Reid, F.M.H., Matrai, P., and Mullin, M.M. 1988a. Vertical distribution of marine particles and grazers. I. Vertical distribution of food quality and quantity. Marine Ecology Progress Series, 50: 45-58.

Napp, J.M., Brooks, E.R., Matrai, P., and Mullin, M.M. 1988b. Vertical distribution of marine particles and grazers. II. Relation of grazer distribution to food quality and quantity. Marine Ecology Progress Series, 50: 59-72.

Ohman, M.D., Frost, B.W., and Cohen, E.B. Reverse diel vertical migration: An escape from invertebrate predators. Science, 220: 1404-1407.

Ohman, M.D., Drits, A.V., Clarke, M.E., and Plourde, S. 1998. Differential dormancy of co-occurring copepods. Deep-Sea Research II, 45: 1709-1740.

Paffenhöfer, G. 1993. On the ecology of marine cyclopoid copepods (Crustacea, Copepoda). Journal of Plankton Research, 15: 37-55.

Ploug, H., Iversen, M.H., and Fischer, G. 2008. Ballast, sinking velocity, and apparent diffusivity within marine snow and zooplankton fecal pellets: Implications for substrate turnover by attached bacteria. Limnology and Oceanography, 53: 1878-1886.

Powell, J.R. and Ohman, M.D. 2012. Use of glider-class acoustic Doppler profilers for estimating zooplankton biomass. Journal of Plankton Research, 34: 563-568.

Prairie, J.C., Franks, P.J.S., and Jaffe, J.S. 2010. Cryptic peaks: Invisible vertical structure in fluorescent particles revealed using a planar laser imaging Fluorometer. Limnology and Oceanography, 55: 1943-1958.

Prairie, J.C., Ziervogel, K., Arnosti, C., Camassa, R., Falcon, C., Khatri, S., McLaughlin, R.M., White, B.L., and Yu, S. 2013. Delayed settling of marine snow at sharp density transitions driven by fluid entrainment and diffusion-limited rentention. Marine Ecology Progress Series, 487: 185-200.

Remsen, A., Hopkins, T.L., and Samson, S. 2004. What you see is not what you catch: a comparison of concurrently collected net, Optical Plankton Counter, and Shadowed Image Particle Profiling Evaluation Recorder data from the northeast Gulf of Mexico. Deep-Sea Research I, 51: 129-151.

Saiz, E., Griffell, K., Calbet, A., and Isari, S. 2014. Feeding rates and prey: predator size ratios of the nauplii and adult females of the marine cyclopoid copepod *Oithona davisae*. Limnology and Oceanography, 59: 2077-2088.

Sommer, F., Hansen, T., Feuchtmayr, H., Santer, B., Tokle, N., and Sommer, U. 2003. Do calanoid copepods suppress appendicularians in the coastal ocean? Journal of Plankton Research, 25: 869-871.

Steele, J.H. (Ed). 1978. Spatial pattern in plankton communities. NATO Conference Series, Springer, New York, 470 pp.

Tomita, M., Shiga, N., and Ikeda, T. 2003. Seasonal occurrence and vertical distribution of appendicularians in Toyama Bay, southern Japan Sea. Journal of Plankton Research, 25: 579-589.

Wiebe, P.H., and Benfield, M.C. 2003. From the Hansen net towards four-dimensional biological oceanography. Progress in Oceanography 56: 7-136.

Wiebe, P.H., Lawson, G.L., Lavery, A.C., Copley, N.J., Horgan, E., and Bradley, A. 2013. Improved agreement of net and acoustical methods for surveying euphausiids by mitigating avoidance using a net-based LED strobe light system. ICES Journal of Marine Science, doi:10.1093/icesjms/fst005.

CHAPTER 3

ZOOPS-O^2: a broadband echosounder with coordinated stereo optical imaging for observing plankton *in situ*

Christian Briseño-Avena, Paul L.D. Roberts, Peter J.S. Franks, Jules S. Jaffe

3.1. Abstract

Here we describe the configuration, calibration, and initial results from the combination of two recently developed underwater instruments that measure acoustic reflectivity and, simultaneously, the location, pose and size of millimeter-sized plankton relative to the sonar beam. The acoustic system, ZOOPS (ZOOPlankton Sonar), uses a broadband chirp signal that operates with a single monostatically configured transducer in the 1.5 – 2.5 MHz frequency range. We demonstrate that the system can record, with adequate signal-to-noise levels, identifiable reflections from single copepods with lengths as small as 360 μm. To simultaneously identify taxa and measure orientation, a pair of "O-Cam" microscopes were stereoscopically calibrated and geometrically co-registered with the orientation and range-resolved acoustic transmissions of the sonar beam. The system's capability is demonstrated via the *in situ* measurement of acoustic reflectivity as a function of orientation for 224 individual pelagic copepods comprising three orders of free-living taxa. Comparison with a well-known model, the Distorted Wave Born Approximation (DWBA), using a spheroidal formulation, yields both differences and similarities between the *in situ* field data and the model's predictions.

3.2. Introduction

As acoustic systems continue to be employed routinely in underwater monitoring, there is strong interest in the refinement of methods for *in situ* sensing of various pelagic and benthic features of the environment. This is especially true given the continued and increasing human exploitation – and in many cases depletion – of marine resources. Simultaneously, as the effects of climate change become more apparent there is a need for improved tools to assess the changes.

In the ocean, acoustic methods have many advantages over other potential remote sensing approaches: the low absorption and frequency-dependent properties of sound can be used to acquire information about many important aspects of the submarine world that are invisible to other methodologies. Acoustic methods have been prominent in, for example, the management of fish stocks and the survey of the sea floor for oil and gas exploration or the retrieval of lost objects such as jetliners.

Because of the importance of plankton in underwater ecology, a variety of remote sensing methods to measure abundance as a function of taxonomic category, including optical and acoustic techniques, have been under development for quite some time (e.g., Fernandes et al., 2002; ICES, 2011, 2012, 2013, 2014). To interpret acoustic field data it is important to have either direct empirical observations from known organisms, or a model that can be inverted to obtain the desired results. Ideally, the model would be derived from physical principles based on the organism's morphological and acoustic properties, and applied in concert with *a priori* knowledge

of the planktonic (or nektonic) species assemblage known to occur in a given ecosystem.

The end product of a typical field program to verify the sources of acoustic backscatter is a set of observed size-class distributions of dominant taxa, a practice oftentimes referred to as “ground truthing”. The methods to collect the data include nets (Sutor et al., 2005; Lavery et al., 2007; Lavery et al., 2010; Powell and Ohman, 2012), pumps (Costello et al., 1989; Pieper et al., 1990), and/or optical systems (Benfield et al., 1998; Wiebe et al., 1996; Lavery et al., 2007). Acoustic backscatter data has also been collected in the lab, though this has been limited to a few taxa such as euphausiids, pteropods and physonect (gas-bearing) siphonophores that can be collected without damaging the organisms (Stanton et al., 1996; Stanton et al., 1998 A, B; Stanton et al., 2004).

In addition to using the more traditional volume backscatter systems that were primarily developed for fisheries and bottom surveys, several systems have been formulated specifically for plankton. One such system, developed by Van Holliday and co-workers over a number of decades, had a variety of realizations; all were based on the use of a number of narrow-band frequencies spanning a given frequency range. Early versions of the system used as many as 21 frequencies (Holliday and Pieper, 1980; Pieper et al., 1990) while the last versions (TAPS) mostly used four. Building on this work, the BIOMAPER system, as developed by Wiebe and colleagues (Greene et al., 1989; Wiebe et al., 1990; Wiebe et al., 1996), employed 5 frequencies (43, 120, 200, 420, and 1000 kHz). This system was deployed extensively; however, the

complexity of the backscattered waveforms, the complications due to orientation dependence, and the strong dependence on rare but extremely strong scatterers (Stanton et al., 1996; Wiebe et al., 1996), and the resultant ambiguities has restricted the interpretation of the data in many applications.

One system that used concurrent optic and narrowband acoustic technologies to identify individual targets producing a given *in situ* echo was the FishTV multibeam system (Jaffe et al., 1998). Here, individual acoustic signals of relatively large mesozooplankton (gammarid amphipods, euphausiids: 5.3-20 mm) and micronekton (gadid fish: 36-92 mm) were measured. A later version of the system, FishTV Jr. was used in the Red Sea, without optical technology, to test the hypothesis that zooplankton, likely copepods, were holding depth in the face of vertical currents (Genin et al., 2005).

A more recent advance in acoustic echosounders is the use of spectrally continuous, broadband systems (Stanton, 2012; Fornshell and Tesei, 2013). Such systems result in higher range resolution (Chu and Stanton, 1998; Stanton and Chu, 2008; Stanton, 2012), which increases the ability to observe echoes from individual scatterers, allowing echo counting. Furthermore, continuous spectral information can provide an advantage in taxonomic discrimination (Roberts and Jaffe, 2007, 2008). Recent broadband systems of Ross and Lawson (2009) used 85-155 kHz sound and that of Lavery et al. (2010) used frequencies of 50-600 kHz to study copepods, pteropods, amphipods, and euphausiids with sizes between 2 mm and close to 3 cm.

Since the most abundant net mesozooplankton in pelagic habitats are < 5 mm (e.g., Gallienne and Robins, 2001; San Martin et al., 2006; Thompson et al., 2013) there is clearly a need to measure small organisms. In pursuit of this goal, and building on work of previous investigators, we invented the ZOOPS-O^2 (ZOOPlankton Sonar with stereo Optical imaging) system. ZOOPS-O^2 is designed to obtain broadband acoustic reflections *in situ* from small (360 μm to < 2 cm), individual plankton with concurrent stereoscopic images of the organisms. The instrument combines two stand-alone technologies – acoustic and optic – to unambiguously assign the acoustic echo of individual living and non-living particles to their simultaneous stereoscopic images. The system employs a broadband, ultrasonic transducer (1.5-2.5 MHz) with close to millimeter range resolution and a stereoscopic camera system to image organisms. ZOOPS-O^2 is self-contained, and can be profiled vertically or towed. To date, the system has been used to measure thousands of acoustic reflections with concurrent optical identification. Importantly, this includes delicate, free-living taxa that are abundant, but difficult to assess in lab-based experiments due to their fragility.

Here we detail the configuration, calibration, and at-sea deployment of the ZOOPS-O^2 system. First, the optical and the acoustic systems are described separately. The stereo-camera calibration and its progression to the acousto-optic calibration (mapping acoustic data into the camera coordinate system) are then documented. This includes quantifying the 3-dimensional location and pointing angles of all components. The acousto-optic coincident volume and the frequency response of the acoustic system are then detailed. The use of the geometrically calibrated system

to estimate correspondence between individual sonar reflections and the target's 3-dimensional location and pose (orientation) relative to the sonar is then discussed. Finally, the application of the system to estimate the acoustic reflectivity, size, and orientation of 224 individual pelagic copepods from the orders Calanoida, Cyclopoida and Poecilostomatoida is described, with comparison to a well-known model, the Distorted Wave Born Approximation (DWBA) (Chu and Ye, 1999).

3.3. Material and Methods

3.3.1. O-Cam – a shadowgraph camera system

The O-Cam (Fig. 3.1) is based on a shadowgraph design (Settles, 2001) that uses a machine vision camera for imaging and a Light Emitting Diode (LED) strobe for illumination. The camera, an AVT GX-1910 (Allied Vision, USA) employs a Kodak 1920 x 1080 CCD with 5.5 μm pixels. It is used with a Rainbow S6X11M-II motorized 2/3" format CCTV zoom lens (Rainbow, USA). The magnification of 0.2 results in a 5.3 x 3.0 cm field of view, from which a 3.0 cm diameter circular sub-area is used. A 10W Blue LED array (LedEngin, USA) collimated with a condenser lens of focal length equal to 60 mm and diameter of 50.8 mm (Thor labs, USA) is used for illumination with a holographic diffuser (Edmund Optics, USA) placed between the LED array and the condenser, creating a more uniform illumination. The illumination system, in one housing, is aimed so the light beam projects directly into the camera in the second housing. The distance between the two housings is 71 cm, with the sampled volume approximately centered between the two.

The characterization of the camera system was relatively straightforward. Using test targets, the results indicated that a best resolution of approximately 30 μm is obtained at the focal plane with a field of view of 3 cm. Moving ±1.5 cm away from this center focal plane results in a decrease of resolution to approximately 54 μm. Images collected with the system permit reasonable identification of organisms as small as 360 μm in length (Fig. 3.2). In practice, the images are relatively immune to the potentially smearing effects of ship heave and water motion: the pulse length employed by the LED was ≤50 microseconds in all experiments reported here.

3.3.2. ZOOPlankton Sonar (ZOOPS)

The ZOOPlankton Sonar (ZOOPS) system consists of four single transducers that can be used to simultaneously transmit and receive (T/R) sound. However, here only one transducer is used in the T/R mode. All systems are controlled and synchronized with a National Instruments PXI-8081 embedded single board computer running Windows XP. In addition, a custom LabVIEW software program logged data from all of the sensors and controlled basic system operations. The signal synthesis and acquisition boards used a PXI-5412 100 MHz analog output board (National Instruments, USA), and a PXI-6115 10 MHz 12 bit analog to digital converter (National Instruments, USA). For transmit, the low-level analog output signal from the PXI-5412 was amplified with a 250 W power amplifier (AR Worldwide, USA). For receive, the low-level output from the transducer (TC3021, Reson, USA) was amplified with low noise preamplifiers (N.T.S. Ultrasonics, Australia).

A linear frequency modulated (LFM) chirp was used for all experiments:

$$y(t) = \cos\left(2\pi t\left[\left(\frac{f_{\max} - f_{\min}}{2T}\right)t + f_{\min}\right]\right)\sin\left(\frac{t\pi}{T}\right)^{\frac{1}{4}}, \text{ for } 0 \le t \le T \tag{1}$$

where $f_{\min}$ =1.5 MHz, $f_{\max}$ = 2.5 MHz and T = 0.5 ms. The amplitude weighting via the sine term with fractional power in (1) provided a compromise between bandwidth and side lobes in the transmit signal. A digital version of (1) using a 10 MHz sample rate

$$y_{ref}[n] = \cos\left(\frac{2\pi Tn}{N}\left[\left(\frac{f_{\max} - f_{\min}}{2T}\right)\frac{Tn}{N} + f_{\min}\right]\right)\sin\left(\frac{n\pi}{N}\right)^{\frac{1}{4}}, \text{ for } n = 0,1,..N \tag{2}$$

was used for signal synthesis and correlation processing, where N = 5000 samples.

The received signal was amplified with 70 dB gain and digitized at 10 MHz with 12 bit dynamic range to yield the measured waveform $y_m[n]$. In adjusting the range of the A/D a value was chosen so that as much of the full dynamic range as possible was used from the anticipated targets at the given range. The digitized waveforms were then cross-correlated with the reference signal (2) to yield the pulse-compressed waveform

$$cp_m = y_{ref} \otimes y_m \tag{3}$$

where ⊗ denotes cross-correlation and the subscript *m* denotes the measurement. The compressed pulse has much better range resolution than the transmitted signal and therefore allows identifying reflections from individual targets and surfaces.

The sonar system was calibrated with a 5 mm-diameter tungsten-carbide sphere tethered with a 25 μm nylon monofilament, and using the partial-wave technique of Dragonette (1981) that was extended to broadband waveforms and pulse-compressed processing by Stanton and Chu (2008). This method relies on isolating the first reflection from the calibration target, which is possible in this case due to the bandwidth of the system. To obtain the target strength of the calibration sphere, let the wavenumber of the sonar be *k* and the radius of the calibration sphere be *a*. At the center frequency of the sonar (2 MHz), $ka = 21$. It has been shown (Stanton and Chu 2008) that when $ka >> 1$, the magnitude of the first reflection from the sphere is approximately frequency-independent and the target strength of the sphere can be approximated as

$$TS_{sphere}(a) = 10\log\left(\frac{a^2}{4}\right) \tag{4}$$

To characterize reflections from sonar targets with a single scalar value, the pulse-compressed echo from the calibration sphere was then used to estimate the magnitude-squared of the first reflection

$$y_{cal} = \max_{n}\left(\mathrm{Env}\left[cp_{sphere}[n]^2\right]\right) \tag{5}$$

where Env[] denotes the envelope of the waveform computed from the absolute value of its Hilbert Transform (Oppenheim et al., 1999) and the max is taken over a window around the echo. In a similar fashion, the magnitude-squared of the compressed pulse of the echo from a target is computed as

$$y_{bs} = \max_{n}\left(\mathrm{Env}\left[cp_{bs}[n]^2\right]\right) \tag{6}$$

Next, using the partial-wave TS method described above, the Broadband Target Strength was defined as

$$BTS = 10\log_{10}\left(\frac{y_{bs}}{y_{cal}}\right) - 58.1 \text{ dB} \tag{7}$$

Note that the BTS is a weighted superposition of frequencies that are coherently added. In this sense, it can be viewed as a weighted average of the individual Target Strengths as a function of frequency, with suitable weights imposed by the envelope of the transmitted signal over the signal bandwidth.

In addition to the BTS, an estimate of the spectrum, B(*f*), from an individual target was computed. Let the Fourier transform of the windowed and zero-padded, first reflection from the calibration sphere be $CP_{sphere}(f)$, and the Fourier transform of

windowed and zero-padded echo from a target be $CP_{bs}(f)$, where f denotes frequency. Then

$$B(f) = 10\log_{10}\left|\frac{CP_{bs}(f)}{CP_{sphere}(f)}\right|^2 - 58.1 \text{ dB} \quad (8)$$

A comparison of the spectrum of the digitally synthesized signal with that of the impulse response from the pulse-compressed first reflection is shown in Figure 3.3. As can be seen, there is some reduction in bandwidth and a bit of shaping, primarily a result of the frequency response of the transducer and downstream electronics.

As part of the calibration, a value for the system noise level was established. This was determined by examining the average magnitude of the compressed-pulse output when no target was present, over a small range-resolved volume about 0.85 m from the transducer, where the sonar and optical volumes intersect (see section 3.3.3.2). The BTS value here was found to be close to -130 dB. A target was judged to be present when the BTS exceeded this level by 10 dB resulting in a minimum target detection level of BTS = -120 dB and an SNR of 10 dB.

3.3.3. ZOOPS-O^2 system configuration and components

The two stand-alone systems (O-Cam and ZOOPS) were assembled into a platform named ZOOPS-O^2, the "O^2" indicating that two O-Cams were configured together to build a stereoscopic system. ZOOPS-O^2 is a system that simultaneously

acquires both optical images and the broadband backscatter from particles within the common sampling volume of the transducer and cameras. In this configuration, it is possible to identify and extract the echo produced by a target while optically imaging the same target that produced the echo. The two cameras allow calculation of the 3D locations of the imaged particles. The projected optical images can also be used to infer the 3D locations of parts of the target by identifying common points in the images. This facilitates the measurement of particle length, width, and the orientation of the longest axis, relative to the incident sonar beam. The resultant sampled volume in this system (estimated at 20.03 mL) is constrained by the stereoscopic system and can be approximated by the volume of two intersecting cylinders (Hubbell, 1965).

3.3.3.1. Stereoscopic system

The O-Cams were configured to obtain a stereoscopic view of a common volume, subsequently referred to as the “stereoscopic volume”. The cameras were positioned and aimed so that the center of the common volume and the center of the two camera images were coincident. In addition, the camera volumes were configured so that the volume from each camera intersected the center of the other camera’s depth of field. This resulted in a stereoscopic volume that was approximately one fifth as large as the total imaged volume. However, it allowed accurate triangulation of targets that appeared in both of the cameras.

3.3.3.1.1. Stereoscopic system calibration

The cameras were calibrated using the stereo calibration toolbox for MATLAB (Jean-Yves Boguet, http://www.vision.caltech.edu/bouguetj/calib_doc/, Camera Calibration Toolbox for MATLAB). Although this software was used for convenience, the calibration of stereo imaging systems is well known; methods generally rely on imaging a common set of targets to establish the intrinsic and extrinsic camera parameters with the extrinsic parameters for each camera referenced to a global coordinate system (Jain et al., 1995). Given the small imaged volume and the geometry of the cameras, calibration was performed using a checkerboard target with 2 mm ±20 μm squares printed on a transparency (Fig. 3.4a,b). The stereoscopic calibration maps points in the 3D space defined by the intersection of two cameras' fields of view onto pixels in each camera image. Figure 3.4c, for example, shows all the back-projections of the calibration checkerboard images in 3D space and with respect to the relative position of the O-cams. Because only a small area of the checkerboard was visible simultaneously in both cameras (area bounded by yellow asterisks and orange lines in Figure 3.4a,b), the target was marked with letters and numbers to uniquely identify the squares used during the calibration process. All calibration exercises were done in a large tank filled with fresh water. This did not likely introduce significant bias into our calibration measurements.

The result of the calibration provided the input to the algorithm that computed the 3D positions of objects simultaneously imaged by the two cameras. All of the objects, including cameras, their pointing angles, and the subsequent location of the

transducer, were defined in a common coordinate system, referred to as the Global Coordinate System (GCS) (Fig. 3.4c).

3.3.3.2. Combining optics and acoustics

In order to use the stereo optics to identify the target that generated the observed acoustic reflection, the two systems, ZOOPS and the two O-Cams, now O^2, were assembled using a metal frame (Fig. 3.5d). For this study, the two O-Cams were mounted on the frame 25.5 cm below a circular aluminum plate with a post-calibrated angle of 115^o between them (Fig. 3.5a). The transducer was aimed downward with a post-calibrated angle of 16.5° with respect to the O-Cams (Fig. 3.5b) and, as measured, approximately 85.3 cm from the center of the stereoscopic volume (Fig. 3.5a,b). This is where the acoustic beam crosses the stereoscopic volume. This geometry resulted in the transducer beam pointing toward the stereoscopic volume (Fig. 3.5c) while avoiding strong reflections from the aluminum frame.

The next task was to establish object positions in the GCS and measured range in the acoustic system, given the physical location of all devices. Here, the tungsten-carbide sphere tethered with a 25 μm nylon monofilament used for acoustic calibration was imaged by the stereoscopic camera system, while simultaneously recording acoustic reflections (pings). The acoustic reflection was characterized by its range (r) in meters (subtracting 2.5 mm to compute the center of the sphere) and the BTS in dB. For each acoustic measurement, the position of the tungsten-carbide sphere in the GCS was recorded. The total data set consisted of 1342 image pairs and “pings”.

To co-register the optic and acoustic systems, the 3D origin of the ping in the coordinate system of the stereo camera is needed. To accomplish this a simple minimization algorithm was used. Given the set of 1342 3D locations of the sphere, where (x_i,y_i,z_i) designates the "ith" location, and the corresponding, measured, acoustic range as $r_{measured_i}$ we seek the acoustic origin of the transducer (h,k,l) so that $r^2_{measured_i} = (x_i - h)^2 + (y_i - k)^2 + (z_i - l)^2$ over the entire set of data. The equation ensures that the distance from the origin of the acoustic sound to the measured range is equal to the measured range to the sphere as computed from the 3D optical data. The position of the acoustic origin is estimated by minimizing

$$\min\left\{\sum_{i=1}^{N} abs\left[(x_i - h)^2 + (y_i - k)^2 + (z_i - l)^2 - r^2_{measured_i}\right]\right\} \tag{9}$$

The MATLAB function *fminsearch* was used to find (h,k,l) that satisfied equation (9), though a variety of optimization algorithms could have been used to solve this equation as there are only three unknown parameters with search bounds given by positions measured on the aluminum frame (Fig. 3.5). Finally, given (h,k,l) and (x_i,y_i,z_i), the acoustic ranges ($r_{predicted_i}$) were predicted using the expression: $r^2_{predicted_i} = (x_i - h)^2 + (y_i - k)^2 + (z_i - l)^2$.

The optimized values of (h,k,l) taken over all of the 1342 tungsten-carbide sphere locations resulted in a residual between $r_{measured_i}$ and $r_{predicted_i}$ with a mean of 0.063 mm and standard deviation of ±0.2217 mm. This acousto-optic calibration

produced a mapping between the 3D, optically imaged volume, computed from the pair of stereo images, and the corresponding acoustic range of the transducer. This then permitted the localization of a particular target's echo in range given the target location in the GCS computed from the stereo image pair.

Data from the acousto-optic calibration are displayed in figure 3.6 where the basic setup that includes the pair of images and the 3D location of the sphere (Fig. 3.6a), and the acoustic beam (Fig. 3.6b) is shown. Figure 3.6c shows the set of corresponding acoustic ranges computed from the derived knowledge of 3D position and the range of positions of the sphere that was moved around inside the illustrated volume. As expected, a single range describes an arc of positions, centered on the transducer origin. Figure 3.6d shows the estimated set of BTS values, as computed using equation 7 (section 3.3.2). We note that, over the range of target positions, the recorded BTS of the sphere (assuming its value of -58.1 dB is at the center) does not vary by more than ±3 dB. It was therefore not necessary to obtain an estimate for the center of the acoustic beam and then correct for target location relative to the beam axis. Likewise, corrections for spreading and attenuation were not implemented, for the same reason. As a further confirmation, a simulation of the broadband beam pattern for the identical diameter transducer after implementing the correlation receiver indicated that the beam width was in agreement with that measured via the use of the calibration sphere.

In summary, the stereo calibration resulted in the ability to compute a 3D location in the GCS given the set of labeled points from O-Cam 1 and O-Cam 2. In addition, the acoustic and optical calibration permitted the prediction of the range of the target observed by the sonar from the location in the GCS. As observed, the small variance in the set of calibrated records indicate the accuracy of this procedure to at least a quarter of the system's range resolution of close to 1.5 mm and, in almost all cases, when an echo greater than -120 dB was recorded, the 3D position of targets predicted an echo that was observed at the corresponding acoustic range.

3.3.3.3. Ancillary Components

Additional components, not listed above and shared by both systems were: (1) A set of 8, 95 Watt-hour Lithium-Ion battery packs (BA95HC-FL, Ocean Server) allowing up to 8 hours of remote deployment of the entire system, (2) a large pressure housing with depth rating of 500 m, and (3) a temperature-pressure (TP) sensor (SBE 39, Seabird, USA) mounted at the same level as the cameras.

3.3.4. Acquisition and processing of *in situ* data

ZOOPS-O^2 was deployed in the Southern California Bight from the R/V New Horizon March 28-29, 2013. The system was vertically profiled at speed of 15-25 m min^{-1} in a self-recording mode to its maximum rated depth (500 m) or close to the bottom when shallower. Data were processed according to the methodology above and then automatically inspected to identify echoes from the correlator output (Equation 6)

that exceeded the given BTS signal to noise ratio threshold of -120 dB at ranges between 0.84 m and 0.88 m. Corresponding image pairs were then visually inspected and images that were judged to contain the same zooplankter or particle were selected for further processing.

A graphical user interface algorithm (echo-locator) based on the results of the calibration exercises in sections 3.3.3.1.1 and 3.3.3.2 was used to manually identify the echo of the particle imaged *in situ*. The echo-locator algorithm works in the following way: selected imaged pairs are displayed side by side. The user selects the particle present in pictures from both cameras by clicking first on the image from O-cam 1, then on the image from O-cam 2, trying to select the same part of the zooplankton or particle being displayed (red circles on Fig. 3.7 a-b and d-e). By clicking on the images, the points (x_1, y_1) for O-cam 1 and (x_2, y_2) for O-cam 2 are recorded in pixel units. The algorithm then uses the *stereo_triangulation* function from the MATLAB camera calibration toolbox to triangulate the pixel coordinates, which locates the particle in the GCS. To ensure that the same object was selected in both cameras, the point from O-cam 1 is re-projected back onto O-cam 2. If the re-projected point (yellow circles on Figure 3.7b,e) lies on top of the selected point (red circles on Figure 3.7b,e) from camera 2 then the particle selected on both images is inferred to be identical. We call this the re-projection condition.

Once the re-projection condition was satisfied, the particle location was used to estimate its distance to the transducer ($r_{predicted}$, see section 3.3.3.2). The echo found at that location was then interpreted as being produced from the *in situ* optically

identified target. The echo was then extracted for further processing that included determining the BTS, and spectrum, B(*f*).

3.3.5 Computing BTS and modeled spectra, B(*f*), for 224 copepods

Given that thousands of stereo images and their concurrent acoustic data were processed, there were many options for illustrating the performance of the system. Here, the system's performance is demonstrated via the analysis of a subset of targets: 224 individual pelagic copepods from the orders Calanoida, Cyclopoida, and Poecilostomatoida. Data from these 224 organisms were used in a statistical analysis of the reflected energy as a function of target size and orientation. The spectra from the individual copepods were compared to predictions of the Distorted Wave Born Approximation (DWBA) (Chu and Ye, 1999; Lavery et al., 2002) implemented for a homogeneous, prolate spheroid. This comparison will allow comparison of the actual (data) and predicted (DWBA model) effects of size and orientation on the reflected acoustic signal.

3.3.5.1 Estimating Geometric Properties from Stereoscopic Image Data

Taking advantage of the stereoscopic calibration (section 3.3.3.1.1) each of the 224 copepods was modeled as a prolate spheroid, and its major axis **a,** and minor axis **b** were estimated from image data. To accomplish this, four points were selected on the copepod shown on the O-Cam 1 image in this specific order: tip of the prosome (P1), end of the prosome (P2), left side of prosome (P3) and right side of prosome

(P4). The same was repeated for the corresponding copepod on the O-Cam 2 image. The prosome is the main part of the copepod's body (see Figure 3.8). Because these points come from the O-cam images, they are in two dimensions. Hence, these two-dimensional points were translated into the GCS using the *stereo_triangulation* algorithm to yield a set of four 3D points p_1, $p_{2,}$ $p_{3,}$ and p_4, respectively. The major axis length was then estimated as $a = \|p_1 - p_2\|_2$, the minor axis length as $b = \|p_3 - p_4\|_2$, and θ, the orientation of the major axis **a** with respect to the acoustic beam was estimated using

$$\theta = \cos^{-1}\left\langle \frac{p_1 - p_2}{\|p_1 - p_2\|}, \hat{\mathbf{w}} \right\rangle \tag{10}$$

where the unit vector $\hat{\mathbf{w}} = \mathbf{w}/\|\mathbf{w}\|$ is the center orientation of the beam in the GCS and <> denotes the inner product. Finally, the transducer vector **w** (o_1,o_2) was defined by the 3D point o_1 (origin of the transducer (*h*,*k*,*l*) in the GCS system estimated in section 3.3.3.2) and a point o_2. Point o_2 fell on the middle of major axis vector **a** (p_1,p_2) and was estimated using the mid-point formula: o_2=[½ (x_1+x_2), ½(y_1+y_2), ½(z_1+z_2)]. Note that **w** is estimated dynamically depending on the location of vector *b* in the GCS. This way, **w** intersected the major axis of the copepod in question. Because the beam spread angle was 2.2 degrees, this method did not introduce any significant bias to the angle estimates.

An example of this estimation process is shown in Figure 3.8, where the estimated spheroid from the point measurements is projected back into the images to confirm that it is consistent with the image data.

To confirm the quality of the estimates of the geometric parameters from the image data, a MATLAB simulation was performed using the stereoscopic calibration data. In this simulation, a spheroidal copepod was projected into each camera view to represent an imaged copepod and the procedure above was used to estimate the best-fit spheroid model. The spheroidal copepods were given "antennae" and a "urosome" as position clues in order that the points on the projected images could be selected in the same order as in the *in situ* data (e.g., Fig. 3.8). Because the axis parameters of the spheroidal copepod are known, this tested the validity of the estimates of a and b from the *in situ* imaged copepods by the human operator. Out of a set of 10 simulation tests with randomly sized and oriented spheroidal copepods, excellent agreement was found between the simulated and predicted major axis length, and orientation (data not shown).

3.3.5.2 Applying the Distorted Wave Born Approximation (DWBA) to a spheroid

The DWBA for backscattering from a homogeneous prolate spheroid of major axis a, and minor axis b, and major-axis orientation relative to the sonar beam θ is given by (Chu and Ye, 1999):

$$f_{bs}(a,b,\theta,k) = k_1^2 ab^2(\gamma_k - \gamma_\rho)\frac{j_1(2k_2\Phi(a,b,\theta))}{2k_2\Phi(a,b,\theta)} \qquad (11)$$

where j_1 denotes the spherical Bessel function of order 1, and

$$\Phi(a,b,\theta) = \sqrt{a^2 \cos^2(\theta) + b^2 \sin^2(\theta)} \quad (12)$$

and $\gamma_k = (1\text{-}gh^2)/\, gh^2$, $\gamma_\rho = (\rho_2\text{-}\rho_1)/\rho_2 = (1\text{-}g)/g$ and $g = \rho_2/\rho_1$, and $h = c_2/c_1$, are the density and sound speed contrasts between the body and the surrounding medium. To predict values of the BTS and spectrum that would be measured from targets with geometric values of measured (a, b, θ) the equation was implemented in MATLAB using values of g = 1.05 and h = 1.05 (Stanton et al., 1998a,b).

3.4. Results

3.4.1. Discerning echo peaks for multiple targets within the stereoscopic volume

To explore the system's ability to discern echoes from closely spaced targets, image pairs containing multiple targets were evaluated. Figure 3.9 illustrates one such image pair containing three copepods of different sizes within the stereoscopic volume (Fig. 3.9a, b), along with their predicted echoes (Fig. 3.9c). Note that one copepod in each image (marked with black arrows in Figure 3.9a,b) did not appear in the corresponding image. Thus they were separate individuals, located outside of the acoustic beam and the stereoscopic volume. This conclusion is further validated by the absence of additional acoustic reflections inside the shared acousto-optic volume.

3.4.2. Measured versus Modeled (DWBA) BTS and spectra for copepods

A comparison between the modeled (DWBA) and measured BTS for 224 individual copepods measured *in situ* is summarized in Figure 3.10. The graph shows the BTS, one for each animal, as a function of θ (the angle between the major axis a and the transducer vector **w**, section 3.3.5.1). The copepods ranged in length (a) from 360 μm to 4.47 mm and in thickness (b) from 16.4 μm to 1.232 mm. As illustrated, the best agreement between the BTS and DWBA occurs when the copepods are broadside to the acoustic beam. Interestingly, as the organism becomes more aligned with the axis of the sonar beam, the measured BTS decreases more slowly than predicted by the DWBA for the same spheroid. Note that a set of systematic adjustments of the values of the g and h parameters within a reasonable range ($1.01 \leq g,h \leq 1.05$) did not change the BTS values enough to reconcile the two data sets. We also note that the potential error in the angular estimate increases as θ approaches either 0 or π. Accordingly, the variance in the data increases at these more oblique angles.

Spectra, B(f), were also computed for each of the organisms over the usable bandwidth of the *in situ* system between 1.6 to 2.4 MHz. A comparison of the DWBA spectra and those estimated from the acquired data is shown in Figure 3.11.

3.5. Discussion

We have described the combination of a new broadband system (ZOOPS) and a set of underwater microscopes (O-Cam) for viewing plankton. Results indicate that the combined systems have the capability to acoustically observe copepods as small as

360 μm while, at the same time, optically identifying the organism that reflected the sound. While the system performed quite well and the combination of optics and acoustics was successful, a number of instrumentation and interpretation issues remain.

It is important to discern what level of confidence exists in the determination of the BTS values. As explained, the tungsten sphere's BTS was predicted, based on the size and the isolation of the first reflection. While this value is undoubtedly reliable, it is possible that the extrapolation of this value to the reflectivity of small animals that reflect four orders of magnitude less sound could produce errors. To accommodate this large dynamic range the dynamic range of the receivers was adjusted via changes in the preamplifier gains and the full-scale extent of the digitizer. However, there is the potential of introducing error if the changes in amplification and/or the voltage range were not completely linear. We thus regard the observation that the backscatter strength showed less angular dependence than predicted via the DWBA to be a more reliable conclusion than the absolute values of the BTS.

Another important concern is whether the 25 μm tether (visible in Figure 3.7a, b and 6a, b) on the 5 mm sphere contributed to the observed BTS during calibration tests. To explore this, we performed experiments where only the monofilament was in the imaged 3D volume. The measured BTS (-120 to -130 dB) was several orders of magnitude lower than the calibration sphere (-58.1; see section 3.3.3.2). In addition, no knots were used in wrapping the monofilament around the sphere. Rather, the tip of the monofilament was dipped into waterproof glue and immediately attached to the

sphere and let dry overnight. The droplet was mostly flattened at the junction of the line and the sphere's surface, likely causing no effect on the overall reflectivity of the sphere. Though it is virtually impossible to judge the overall effect of the filament, in our estimation it was minimal compared to that of the sphere.

One of the major advantages of combining the optics and acoustics is to measure acoustic echoes with taxonomic identification of the corresponding, visually identified targets. The opto-acoustic calibrations shown in section 3.3.3.2 demonstrate that the images and echoes from individual targets can be simultaneously and accurately located in both the stereoscopic volume and in the acoustic record. Furthermore, the minimal difference between the predicted and observed distances of the calibration sphere with respect to the transducer indicates that *in situ* targets can be accurately located in the acoustic record. Figure 3.9, for example, shows that the system can resolve the acoustic peaks of three copepods contained within the stereoscopic volume. The figure also shows how the presence of an animal in one camera but not the other implies that the animal is outside of the stereoscopic volume.

A current goal in ground-truthing acoustic systems is to reduce the uncertainties in interpreting field data. Stanton (2012) identified several issues regarding acoustic methods, especially at the high-frequency (MHz) range. One is the influence of orientation (tilt angle) of elongated organisms. The stereoscopic nature of ZOOPS-O^2 provides an ideal tool for studying the dependence of BTS on *in situ* orientation, without the confounding influence of tethers, artifacts associated with laboratory settings, or the physiological state of the organisms due to stress or other

post-capture factors (e.g., Greenlaw, 1977; Johnson, 1977). As shown in section 3.3.5 the major and minor axes (*a* and *b*, respectively), and the orientation of the major axis *a* with respect to the acoustic beam were estimated for 224 copepods from the *in situ* data using the stereoscopic calibrations. Assuming the copepod prosome resembled a spheroid, the expected BTS inferred using the well-known Distorted Wave Born Approximation (DWBA) model was compared with the measured BTS.

An interesting result from our comparison of *in situ* measurements of 224 copepods with predictions from a theoretical model was that the spheroidal DWBA under-predicts the BTS compared to the measured data (Fig. 3.10). As is widely appreciated, copepods are not simply spheroidal bags of homogeneous substance but have exoskeletons with antennae, and feeding and swimming appendages. The internal organs of potentially different composition, and oil sacs (spherical or oblong) present in some species of calanoid copepods could contribute to the observed differences between the measured and DWBA. Furthermore, copepod body shape can be diverse (Fig. 3.2), and female copepods can often carry spermatophores (sacs containing the male's sperm) or egg sacs attached to their urosome ("tail") (Fig. 3.2l, n-q). The spheroidal DWBA does not consider the effects of these various features; the nulls that are evident in the spectra in figure 3.11 may be caused by these differences and, moreover, the potential increase in backscatter contrast due to these features are not incorporated into the model.

Given that a perpetual confounding influence in interpreting sonar backscatter has been the organism orientation, it is certainly welcome to see that the *in situ* data are less orientation-dependent than predicted from the elongate structure based on the dimensions of the prosome. Although evaluation of the angle between the animal's major axis and that of the sonar beam is more error prone as the animal becomes less broadside, there is a much less decrease in the BTS value than predicted by the spheroidal model approximation. We therefore have confidence that the departures of the data from the model are real. From this observation we conclude that it is likely zooplankton surveys are less susceptible to copepod orientation than previously thought.

There is a wide range of other applications of the ZOOPS-O^2 system, with many potential benefits. For one, the system could be mounted on the sea floor. This would be useful in a shallow water environment to study plankton abundance and the changes that occur due to predation, reproduction, and dispersion due to flow over local bottom features. In this case, with slow currents, the hydrodynamic signature of the system and the potential for its detection by the organisms would be small. An additional strategy would be to measure changes in abundance, and possibly rates of predation, along current trajectories by employing multiple spatially separated transducers.

It is natural to think that future systems focused on different targets could use the same methodology. For example, there is a dire need for understanding the relationship between backscatter changes as a function of tilt angle for fish. One

approach would be to use a stereo camera system with a sonar to both image the fish and measure its backscatter. The requirement that the organism be in the far field of the sonar imposes a minimal distance for this to work; however, we anticipate that in the future, coupled acoustic and optic systems will be become ever more popular, perhaps following the optical design of the Cam Trawl (Williams et al., 2010) and coupling that to acoustics, in a similar way to the work of Ryan et al. (2009) and Macaulay et al. (2013), where they studied the *in situ* target strength of orange roughy (*Hoplostethus atlanticus*).

With the advent of broadband technologies such as the Simrad EK80 system, an interesting option would be to attempt to classify targets using features of the echo. Such features could include echo envelope width, shape or other statistics. These methods are currently being used to classify images (e.g., Sosik and Olson, 2007), and could be fruitfully extended to sonar echoes. This would be especially valuable in turbid conditions, where the optical system would have substantially less range capability than the acoustics. The joint use of acoustics and optics would also be synergistic in the case of object classification from multiple views, where the different modalities can be fused together to mitigate the orientation-dependent appearance of elongated plankton in image and acoustic data (Roberts et al., 2009).

Lastly, an important area of inquiry would be to use the ZOOPS-O^2 system to study the acoustic properties of fragile, gelatinous taxa (e.g., doliolids, siphonophores, hydromedusae, and ctenophores) as well as chaetognaths and appendicularians, which have important ecological roles. Such organisms have been encountered during

sampling with the system, and efforts to characterize the BTS of a variety of pelagic entities, including marine snow, are currently underway.

3.6. Summary

The ZOOPS-O^2 system combines a stereoscopic camera system with broadband sonar to estimate acoustic reflectivity of individual plankton with concurrent measurement of their size and orientation. Measurements of the system's performance show that copepods as small as 360 μm give a reflected broadband target strength (BTS) that is at least 10 dB above the system's noise level. The 1.5 mm range resolution of ZOOPS, along with the visual identification capabilities of the O-Cam (designated O^2 in stereoscopic mode) permits extraction of echo properties of individual copepod targets in their natural environment with concurrent identification. As demonstrated, ZOOPS-O^2 can be used to study the acoustic properties of this ecologically important plankton group *in situ*.

3.7. Acknowledgements

The authors would like to thank the National Science Foundation (0728305) for funding the development of the system. Christian Briseño-Avena would like to thank UC MEXUS and CONACyT for their support to fund his PhD studies. The authors would also like to thank the captain and crew of the R/V New Horizon for their assistance during fieldwork.

Chapter 3, in full, is a reprint of previously published material as it appears in Methods in Oceanography, 2015, Briseño-Avena, C., Roberts, P.L.D., Franks, P.J.S., and Jaffe, J.S. The dissertation author was the primary investigator and author of this paper.

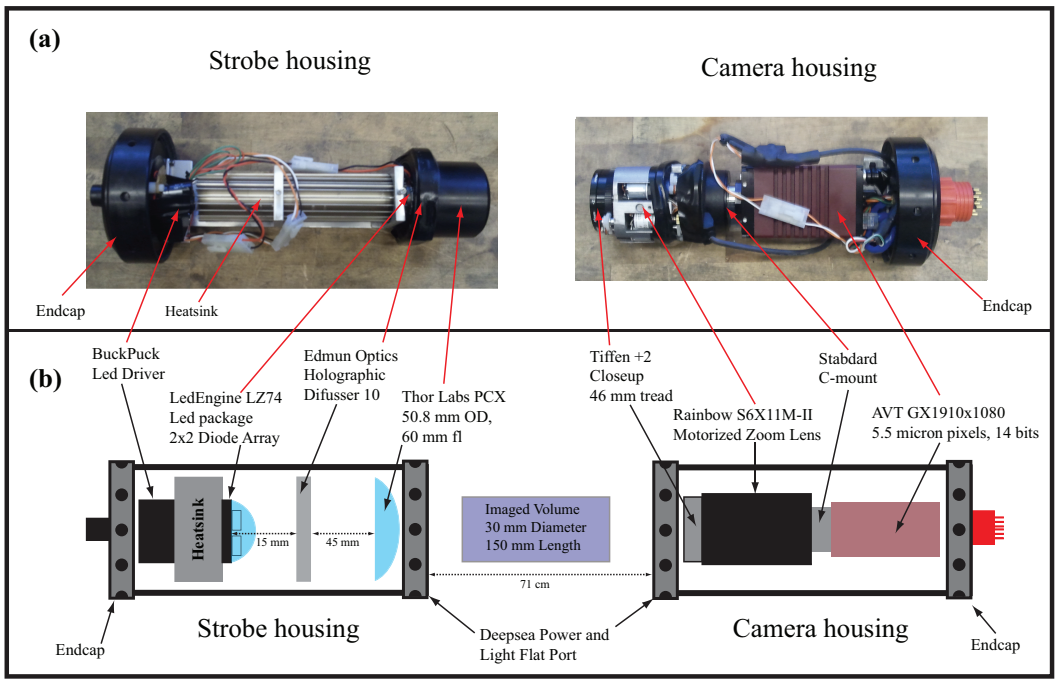

Figure 3.1. O-Cam configuration. (a) The strobe and camera components with the housings removed. (b) Schematic of the strobe and camera housings. The imaged volume size representation is exaggerated in this diagram, but noted dimensions are accurate.

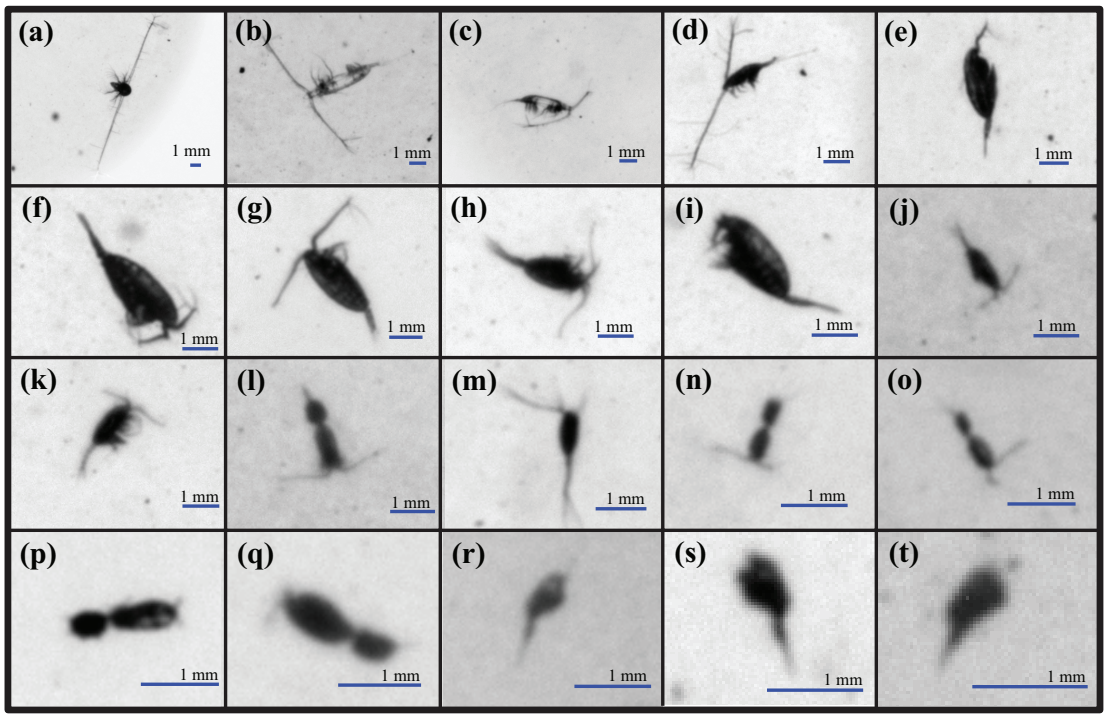

Figure 3.2. Examples of O-cam *in situ* images of Calanoida (a-k), Cyclopoida (l-q), and Poecilostomatoida (r-t) copepods. Images are arranged in order of size from large to small (all scale bars were kept to 1 mm) for ease of comparison. Notice the wide range of orientations.

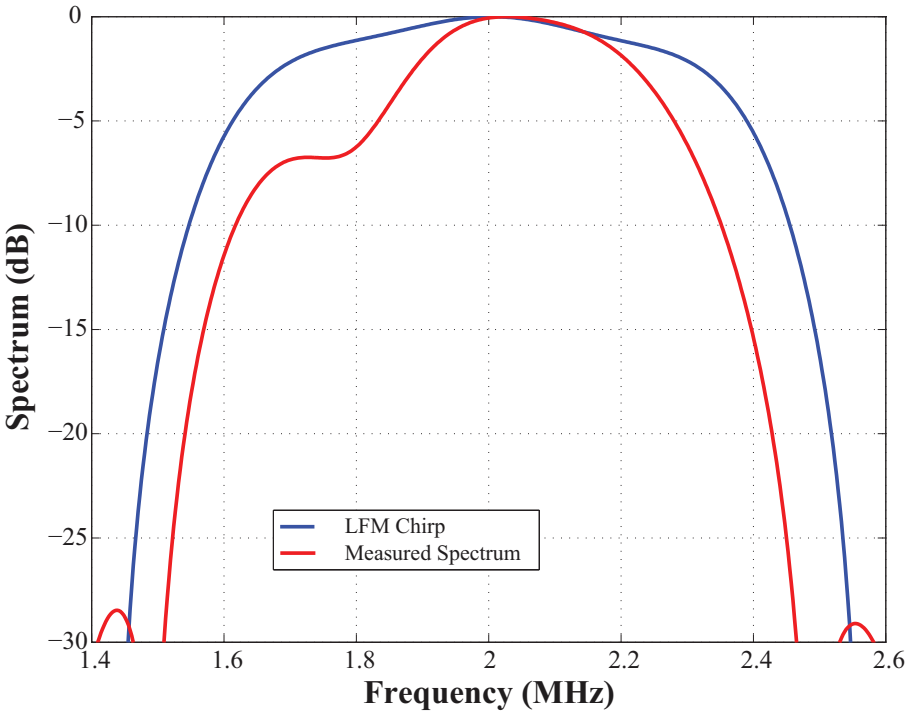

Figure 3.3. A comparison of the LFM chirp spectrum (blue) with that of the measured spectrum (red). See text for definitions.

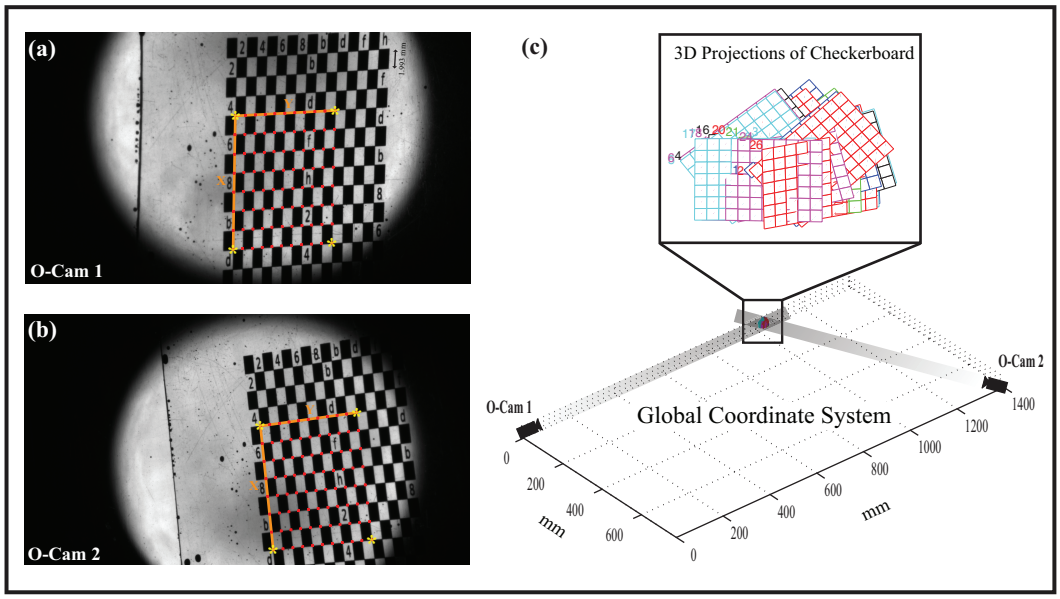

Figure 3.4. Example of the stereo camera calibration. (a-b) Images of the checkerboard target simultaneously imaged by O-cam 1 and O-Cam 2. The yellow asterisks are the corners of the effective area used during calibration. The Orange lines indicate the x and y axes with respect to the upper left corner. (c) The Global Coordinate System (GCS) showing the relative position of O-Cam 2 with respect to O-Cam 1. The intersected imaged volume (gray shaded paths) is enlarged to show the checkerboard projections in the stereoscopic volume.

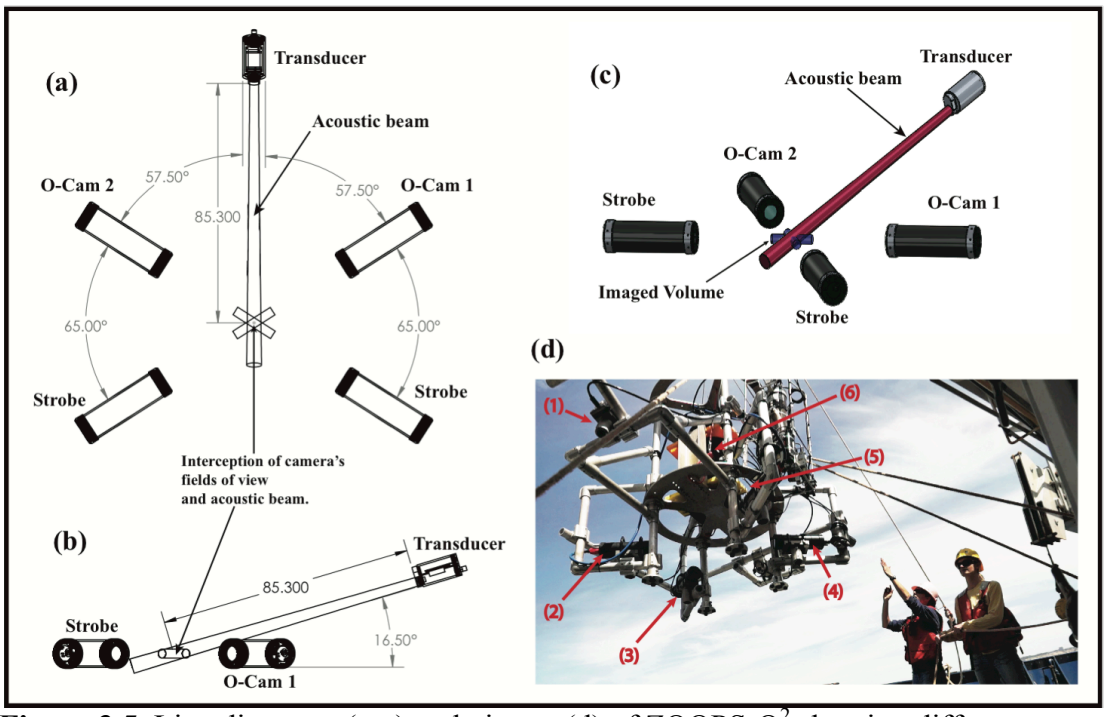

Figure 3.5. Line diagrams (a-c) and picture (d) of ZOOPS-O^2 showing different views. (a) Top-down view of the configuration of the O-Cams and the transducer. The acoustic beam and imaged volumes from the cameras are also drawn. (b) Side view (minus one O-cam for visual clarity) to show the inclination of the transducer with respect to the cameras. (c) 3D rendering showing the two O-cams and transducer as well as the acoustic beam intercepting the stereoscopic volume. (d) The system being deployed at sea from the R/V New Horizon. (1) Transducer; (2) O-Cam 1; (3 and 4) Strobe housings (5) O-Cam 2; (6) temperature-pressure sensor.

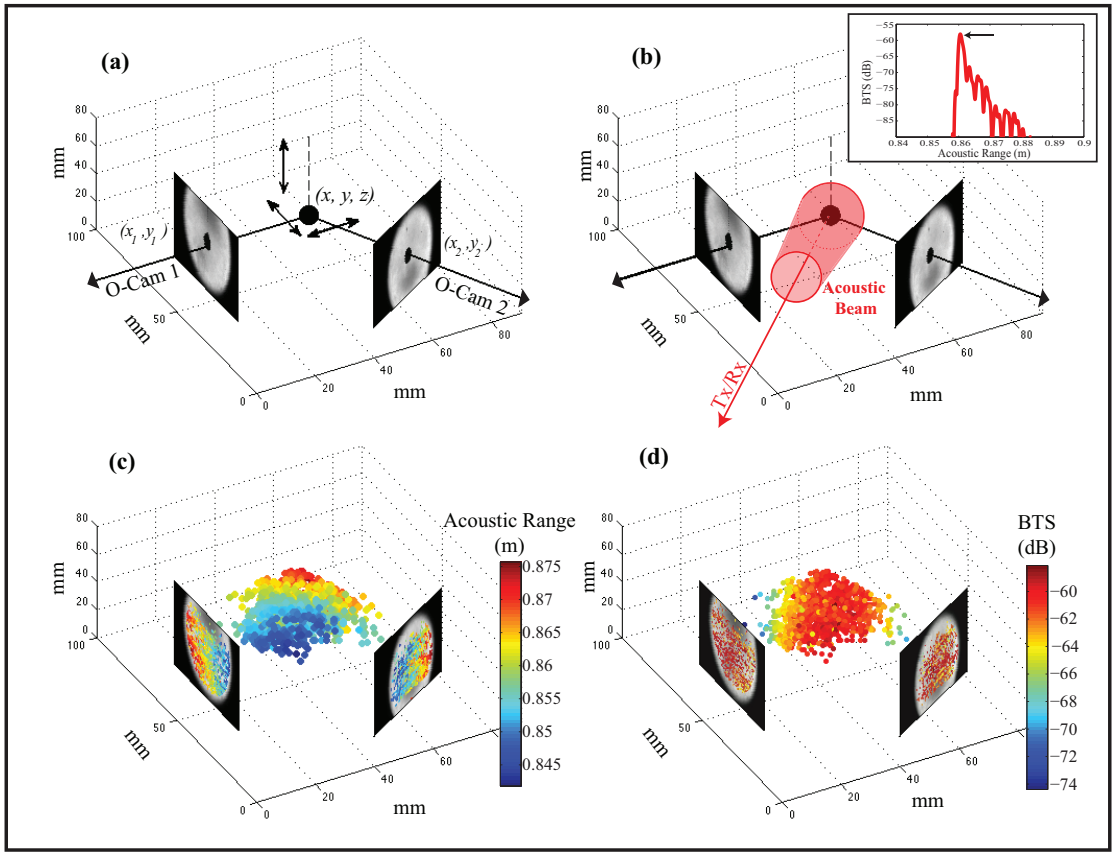

Figure 3.6. The optic and acoustic data in the 3D global coordinate system (GCS). (a, b) The 5 mm tethered tungsten-carbide sphere being simultaneously imaged and ensonified. The inset panel in (b) shows the acoustic record with the peak of the first return indicated with an arrow. The red truncated cone represents a portion of the idealized acoustic beam and the general direction and relative location of the transducer (Tx/Rx). (c, d) The acoustic data (acoustic range, broadband target strength: BTS) mapped in the GCS with the corresponding camera viewpoints, as re-projected into the coordinate system of the cameras.

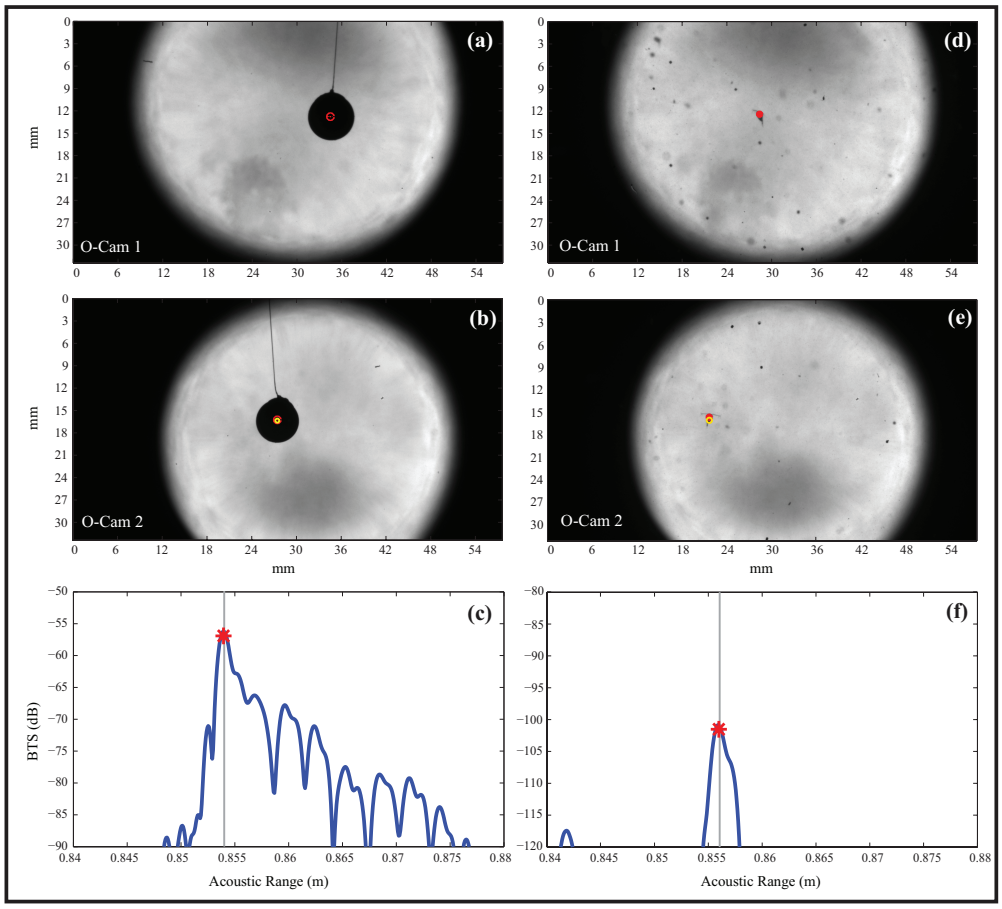

Figure 3.7. Results of the echo-locator algorithm for calibration sphere (a, b, and c) and an *in situ* recorded calanoid copepod (d, e, and f). Red circles in a, b, d, and e indicate manually selected points on individual images. The yellow circles are the points on images from camera 1 (O-Cam 1) re-projected onto images from camera 2 (O-Cam 2). Red asterisks in c and f indicate the peak location of the extracted echo (blue line) and the gray vertical lines represent the predicted peak location in the acoustic range.

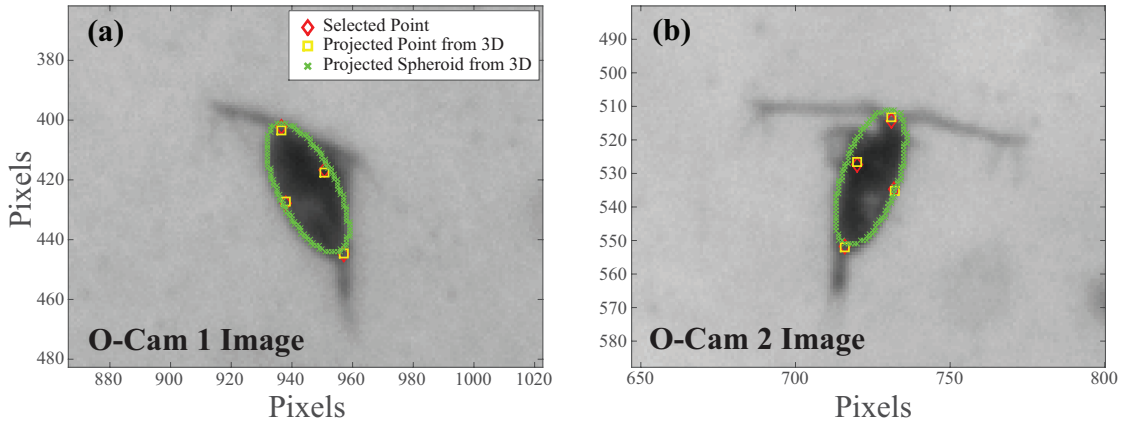

Figure 3.8. Example of the geometric parameter estimation from stereo image pairs. Panels a and b show the O-Cam 1 and O-Cam 2 images of the same copepod, respectively. The red diamonds show the four points selected manually in each image. The yellow squares show the re-projection of the four 3D points estimated from the *stereo_triangulation* back into each image. The green xs demarcate the boundary points of the estimated spheroid projected back into each image. This boundary encloses the copepod's prosome.

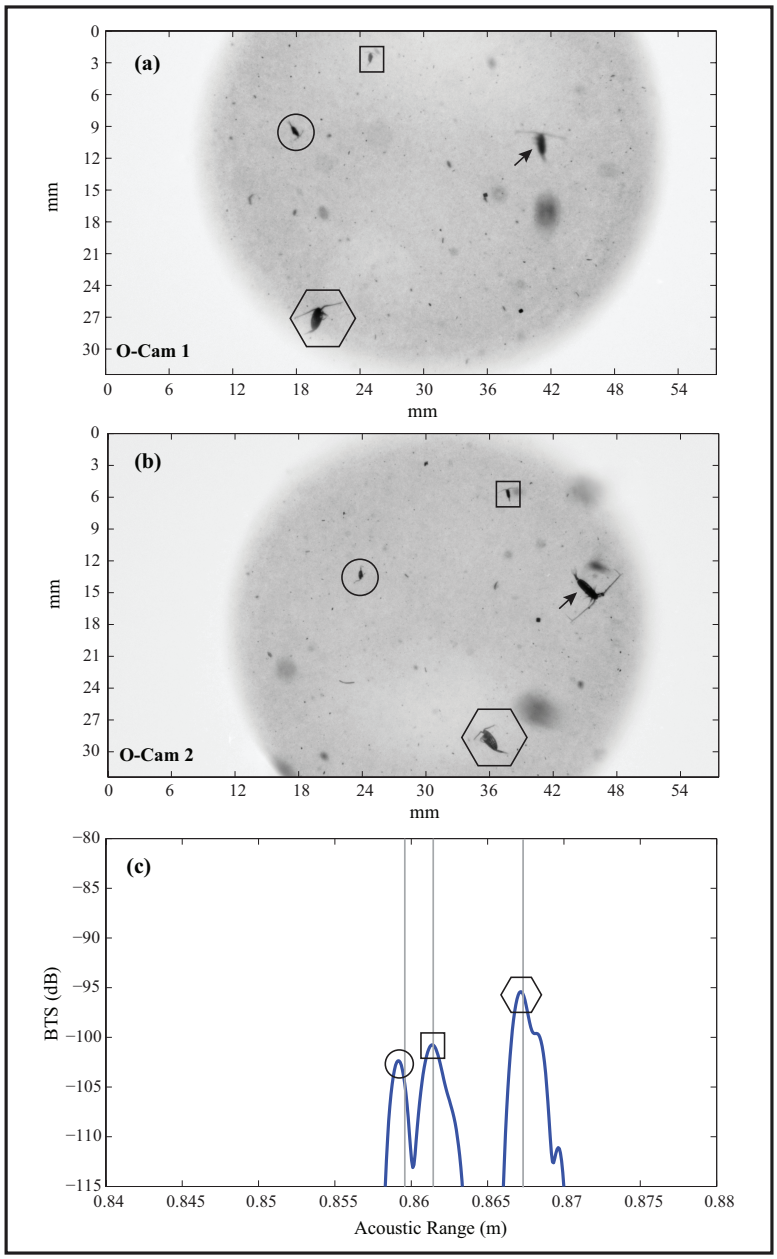

Figure 3.9. Panels a and b are two temporally synchronized images. The images were processed as described to yield a 3D position, and hence a prediction of acoustic range, for each target. Three copepods yielded acoustic reflections whose peaks were well predicted, as indicated by the thin vertical lines in panel c. Geometrical shapes denote the corresponding echo to each copepod in a and b. An additional two copepods, shown by the two arrows in panels a and b were judged to be different and, as expected, the targets are outside of the coincident 3d volume and hence, there are no measured acoustic reflections from the organisms in the acoustic record.

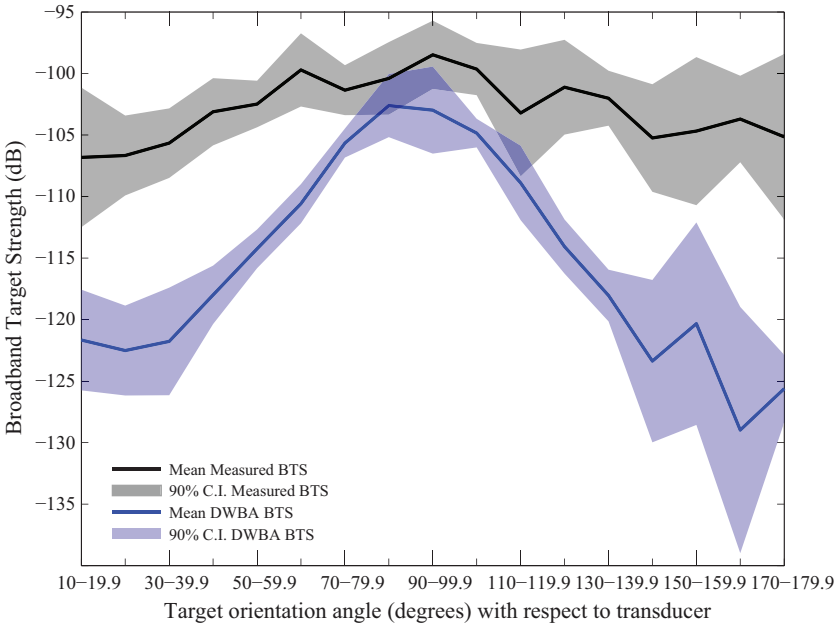

Figure 3.10. Mean (± 90% Confidence Intervals, shaded areas) estimates for measured (black) and DWBA (blue) BTS for 224 copepods. Data was binned every 10 degrees (target orientation with respect to transducer) to estimate the presented statistics.

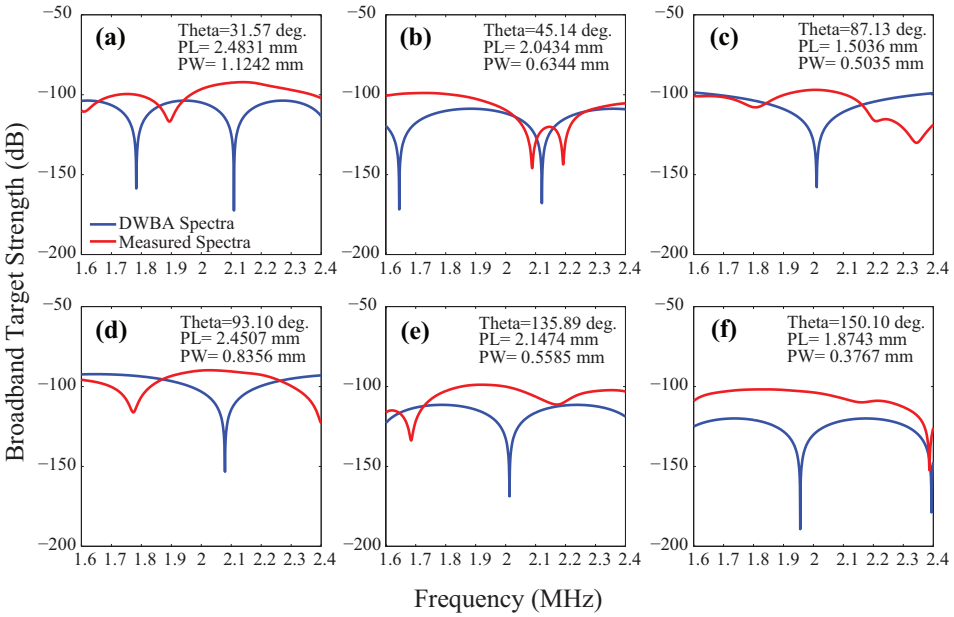

Figure 3.11. Measured (red lines) and modeled (DWBA, blue lines) spectra B(*f*) from five copepods at different orientations with respect to the sonar. Theta values are given in degrees. PL=Prosome Length (major axis *a*); PW=Prosome Width (minor axis *b*).

3.8. References

Benfield, M.C., Wiebe, P.H., Stanton, T.K., Davis, C. S., Gallager, S.M. and Greene, C.H., 1998. Estimating the spatial distribution of zooplankton biomass by combining Video Plankton Recorder and single-frequency acoustic data. Deep-Sea Res. Pt. II, 45: 1175-1199.

Chu, D. and Stanton, T.K., 1998. Application of pulse compression techniques to broadband acoustic scattering by live individual zooplankton. J. Acoust. Soc. Am. 104(1): 39-55.

Chu, D. and Ye, Z., 1999. A phase-compensated distorted wave Born approximation representation of the bistatic scattering by weakly scattering objects: Application to zooplankton. J. Acoust. Soc. Am., 106(4): 1732-1743.

Costello, J.H., Pieper, R.E. and Holliday, D.V., 1989. Comparison of acoustic and pump sampling techniques for the analysis of zooplankton distributions. J. Plankton Res. 11(4): 703-709.

Dragonette, L.R., Numrich, S.K. and Frank, L.J., 1981. Calibration technique for acoustic scattering measurements. J. Acoust. Soc. Am., 69(4): 1186-1189.

Fernandes, P.G., Gerlotto, F., Holliday, D.V., Nakken, O. and Simmonds, E.J., 2002. Acoustic applications in fisheries science: the ICES contribution. – ICES Marine Science Symposia, 215: 483–492.

Fornshell, J.A. and Tesei, A., 2013. The development of SONAR as a tool in marine biological research in the twentieth century. Int. J. Oceanogr. 2013: 1-9.

Gallienne, C.P. and Robins, D.B., 2001. Is *Oithona* the most important copepod in the world's oceans? J. Plankton Res., 23(12): 1421-1432.

Genin, A., Jaffe, J.S., Reef, R., Richter, C. and Franks, P.J.S., 2005. Swimming Against the Flow: A Mechanism of Zooplankton Aggregation. Science, 308: 860-862.

Greene, C.H., Wiebe, P.H. and Burczynski, J., 1989. Analyzing zooplankton distributions using high-frequency sound. Limnol. Oceanogr., 34(1): 129-139.

Greenlaw, C.F., 1977. Backscattering spectra of preserved zooplankton. J. Acoust. Soc. Am., 62(1): 44-52.

Holliday, D.V. and Pieper, R.E., 1980. Volume scattering strengths and zooplankton distributions at acoustic frequencies between 0.5 and 3 MHz. J. Acoust. Soc. Am., 67(1): 135-146.

Hubbell, J.H., 1965. Common volume of two intersecting cylinders. J. Res. NBS C Eng. Inst., 69C(2): 139-143.

ICES. 2011. Report of the Working Group on Fisheries Acoustics Science and Technology (WGFAST), 10–13 May 2011, Reykjavík, Iceland. ICES CM 2011/SSGESST:12. 37 pp.

ICES. 2012. Report of the Working Group on Fisheries Acoustics, Science and Technology (WGFAST), 23-27 April 2012, Brest, France. ICES CM 2012/SSGESST:09. 38 pp.

ICES. 2013. Report of the Working Group on Fisheries Acoustics Science and Technology (WGFAST), 16-19 April 2013, San Sebastian, Spain. ICES CM 2013/SSGESST:09. 42 pp.

ICES. 2014. Report of the Working Group on Fisheries Acoustics, Science and Technology (WGFAST), 6-9 May 2014, New Bedford, Massachusetts, USA. ICES CM 2014/SSGESST:07. 41 pp.

Jaffe, J.S., Ohman, M.D. and De Robertis, A., 1998. OASIS in the sea: measurement of the acoustic reflectivity of zooplankton with concurrent optical imaging. Deep-Sea Res. Pt. II, 45: 1239-1253.

Jain, R., Kasturi, R. and Schunck, B.G., 1995. *Machine vision*. Vol. 5. New York: McGraw-Hill. 549 pp.

Johnson, R.K., 1977. Sound scattering from a fluid sphere revisited. J. Acoust. Soc. Am., 61(2): 375-377.

Lavery, A.C., Stanton, T.K., McGehee, D.E. and Chu, D., 2002. Three-dimensional modeling of acoustic backscattering from fluid-like zooplankton. J. Acoust. Soc. Am., 111:3304-3326.

Lavery, A.C., Wiebe, P.H., Stanton, T.K., Lawson, G.L., Benfield, M.C. and Copley, N., 2007. Determining dominant scatterers of sound in mixed zooplankton populations. J. Acoust. Soc. Am., 122(6): 3304-3326.

Lavery, A.C., Chu, D., and Moum, J.N., 2010. Measurements of acoustic scattering from zooplankton and oceanic microstructure using broadband echosounder. ICES J. Mar. Sci., 67: 379-394.

Macaulay, G.J., Kloser, R.J., and Ryan, T.E., 2013. *In situ* target strength estimates of visually verified orange roughy. ICES J. Mar. Sci., 70(1): 215-222.

Oppenheim, A.V., Schafer, R.W. and Buck, J.R., 1999. Discrete-Time Signal Processing. 2nd ed. Prentice-Hall, Inc., Upper Saddle River, NJ. 796 pp.

Pieper, R.E., Holliday, D.V. and Kleppel, G.S., 1990. Quantitative zooplankton distributions from multifrequency acoustics. J. Plankton Res., 12(2): 433-441.

Powell, J.R. and Ohman, M.D., 2012. Use of glider-class acoustic Doppler profilers for estimating zooplankton biomass. J. Plankton Res., 34(6): 563-568.

Roberts, P.L.D. and Jaffe, J.S., 2007. Multiple angle acoustic classification of zooplankton. J. Acoust. Soc. Am., 121(4): 2060-2070.

Roberts, P.L.D. and Jaffe, J.S., 2008. Classification of live, untethered zooplankton from observations of multiple-angle acoustic scatter. J. Acoust. Soc. Am., 124(2): 796-802.

Roberts, P.L.D., Jaffe, J.S. and Trivedi, M.M., 2009. A multiview, multimodal fusion framework for classifying small marine animals with an opto-acoustic imaging system. *Applications of Workshop on Computer Vision (WACV),* 7-8 Dec. 2009, pp 1:6.

Ross, T. and Lawson, G., 2009. Long-term broadband acoustic observations of zooplankton scattering layers in Saanich Inlet, British Columbia. J. Acoust. Soc. Am., 125:2551.

Ryan, T.E., Kloser, R.J., and Macaulay, G.J., 2009. Measurement and visual verification of fish target strength using an acoustic-optical system attached to a trawlnet. ICES J. Mar. Sci., 66: 1238-1244.

San Martin, E., Harris, R.P. and Irigoien, X., 2006. Latitudinal variation in plankton size spectra in the Atlantic Ocean. Deep-Sea Research Pt. II, 53: 1560-1572.

Settles, G.S. 2001. Schlieren and shadowgraph techniques: Visualizing Phenomena in Transparent Media. Springer. Germany. 376 p.

Sosik, H.M. and Olson, R.J., 2007. Automated taxonomic classification of phytoplankton sampled with imaging-in-flow cytometry. *Limnol. Oceanogr. Methods*, 5: 204-216

Stanton, T.K., 2012. 30 years of advances in active bioacoustics: *A personal perspective*. Methods in Oceanography, 1-2: 49-77.

Stanton, T.K. and Chu, D., 2008. Calibration of broadband active acoustic systems using a single standard spherical target. J. Acoust. Soc. Am., 124(1): 128-136.

Stanton, T.K., Chu, D. and Reeder, D.B., 2004. Non-Rayleigh acoustic scattering characteristics of individual fish and zooplankton. IEEE J. Oceanic Eng., 29(2): 260-268

Stanton, T.K., Chu, D. and Wiebe, P.H., 1996. Acoustic scattering characteristics of several zooplankton groups. ICES J. Mar. Sci., 53: 289-295

Stanton, T.K., Chu, D. and Wiebe, P.H., 1998a. Scound scattering by several zooplankton groups. II. Scattering models. J. Acoust. Soc. Am., 103(1): 236-253.

Stanton, T.K., Wiebe, P.H. and Chu, D., 1998b. Differences between sound scattering by weakly scattering spheres and finite-length cylinders with applications to sound scattering by zooplankton. J. Acoust. Soc. Am., 103(1): 254-264

Sutor, M., Cowles, T.J., Peterson, W.T. and Lamb J., 2005. Comparison of acoustic and net sampling systems to determine patterns in zooplankton distribution. J. Geophys. Res., 110: C10S16

Thompson, G.A., Dinofrio, E.O. and Alder, V.A., 2013. Structure, abundance and biomass size spectra of copepods and other zooplankton communities in upper waters of the Southern Atlantic Ocean during summer. J. Plankton Res., 0(0): 1-20

Wiebe, P.H., Greene, C.H., Stanton, T.K. and Burczynski, J., 1990. Sound scattering by live zooplankton and micronekton: Empirical studies with a dual-beam acoustical system. J. Acoust. Soc. Am., 88(5): 2346-2360

Wiebe, P.H., Mountain, D.G., Stanton, T.K., Greene, C.H., Lough, G., Kaartvedt, S., Dawson, J. and Copley, N., 1996. Acoustical study of plankton on Georges Bank and the relationship between volume backscattering strength and the taxonomic composition of the plankton. Deep-Sea Res. Pt. II, 43(7-8): 1971-2001

Williams, K., Towler, R. and Wilson, C., 2010. Cam-trawl: a combination trawl and stereo-camera system. Sea Technol., 51(12): 45-50.

CHAPTER 4

Underwater active acoustics: an unexpected diversity of *echogenic* particles

Christian Briseño-Avena, Jules S. Jaffe, and Peter J.S. Franks

4.1 Abstract

In 1980, Holliday and Pieper stated: "Most sound scattering in the ocean volume can be traced to a biotic origin." However, most of the bioacoustics research in the past three decades has selectively focused on a few groups of organisms. Targets such as small gelatinous organisms, marine snow, and phytoplankton, for example, have been generally considered acoustically transparent. However, using a broadband system (ZOOPS-O^2) we found that these targets contributed significantly to acoustic returns at 1.5-2.5 MHz frequencies. Given that phytoplankton and marine snow layers are ubiquitous features of coastal regions, this works suggests that they may affect interpretations of acoustical biological surveys. Without appropriate ground-truthing exercises these "weak" scatterers may lead to significant errors in acoustic abundance estimates.

4.2. Introduction

Using acoustical methods to understand the distributions of biological scatterers in the water column requires knowledge of the acoustic properties of such targets. Most ground-truthing and models have concentrated on the understanding the acoustical properties and detection of fishes; relatively little effort has been focused on

planktonic organisms. Some plankton-oriented studies have been carried out in laboratory settings, through *in situ* observations, modeling efforts or combinations of these (e.g., Greenlaw, 1977; Holiday and Pieper, 1980; Richter 1985; Demer and Martin, 1995; Martin et al., 1996; Stanton et al., 1996; Jaffe et al., 1988; Lawson et al., 2004; Briseño-Avena et al., 2015). However, there are still significant gaps in our knowledge. Data from the latest generation of broadband sonars present new opportunities for acoustical investigations of plankton. Such investigations require a thorough understanding of the capabilities and limitations of such systems.

In the past decades, aquatic and fisheries ecologists have favored acoustical methods over optical ones for conducting large-scale biological surveys of zooplankton and fish assemblages (Fernandes et al., 2002). Because of the transparency of water to acoustical waves, sonar methods work well for remote sensing of planktonic and nektonic organisms throughout the water column. The far-reaching sensing capability, fast acquisition and almost real-time processing of acoustical data give acoustical methods an advantage over optical technologies. However, classification of acoustical target returns can be ambiguous. In contrast to sound, water strongly attenuates light, limiting the working range of optical devices. However, what optic methods lack in far-sensing capabilities they gain in their ability to generate details of imaged targets, commonly allowing identification down to genus and often to species; coarse taxonomic identification (i.e. copepod, jellyfish, ctenophore, chaetognath, appendicularian, etc.) is almost always possible.

With a few exceptions in higher latitudes, most marine ecosystems are species rich (e.g., De Monte et al., 2013), with a high diversity not only of species, but also of body shapes, sizes and behaviors. In these regions acoustic methods are at a disadvantage when compared to optic ones: while it is possible to visually distinguish planktonic taxa, it is difficult to acoustically differentiate even the most basic forms with current signal processing methods (Fielding et al., 2004) and the use of narrowband systems.

Historically, narrowband systems working at discrete frequencies have been at the forefront of acoustic methods (Stanton, 2012 and references therein; Fornshell and Tesei, 2013). Yet, the resolution and accuracy required to determine the identity of the targets insonified by such tools have been a major challenge. New developments in broadband acoustic sensors and signal processing have begun to give us new insights into the acoustic properties of planktonic organisms. However, the exploration phase of broadband sensors is an ongoing effort.

Ground truthing (i.e., inter-method comparison) exercises are by far the best and most direct method to aid in acoustic data interpretation. Comparing acoustic data to net-derived and optic-derived estimates of abundance and/or biomass is the most common approach (e.g., Wiebe et al., 1996; Benfield et al., 1998; Sutor et al., 2005; Lara-Lopez and Neira, 2008; Powell and Ohman, 2012). However, fragile organisms such as jellyfish, ctenophores, siphonophores, doliolids and appendicularians can be severely damaged by nets, making it difficult to fully account for them during acoustic-net comparisons. Furthermore, there are organisms and particles such as

marine snow and phytoplankton not sampled by net systems. Since the goal has been to sample zooplankton – despite their conspicuous presence in rich, productive regions of the ocean – other organisms and particles are virtually unaccounted for during traditional ground-truthing experiments. As part of this chapter we investigate the acoustic reflectivity of these often-ignored organisms and particles at high frequencies (1.5-2.5 MHz).

The idea of phytoplankton and marine snow contributing to acoustical returns is not new, with references as far back as 1956 (Cushing et al.). After a gap of almost four decades, the idea of such targets contributing to acoustical returns re-surfaced in a report by Anoshkin and Goncharov (1993). Since then, there have been efforts to quantify the acoustical reflectance of phytoplankton (Selivanovsky et al., 1996; Bok et al., 2010; Bok et al., 2013) and gelatinous organisms (Mutlu, 1996; Brierley et al., 2005; Warren and Smith, 2007). However, no attempts have focused on the potential acoustical reflectance of marine snow. Because of their microscopic size, fragile composition, and patchy distribution, these targets appear to have been ignored in underwater acoustical research and perhaps more importantly, in the interpretation of acoustical survey data.

Phytoplankton thin layers are ubiquitous features of coastal regions, extending over kilometers and persisting from hours to several days (e.g., Cowles et al., 1998, McManus et al., 2003). Their thickness ranges from tens of centimeters to a few meters as documented in a variety of marine environments. Phytoplankton have usually been considered acoustically transparent, and so are ignored as potential

acoustic reflectors. Recently, Timmerman and colleagues (Timmerman, et al., 2014) suggested that a layer containing diatom flocculates was detected by a narrowband sonar (200 kHz), and further, that these particles were responsible for the observed scattering signal.

Marine snow layers are also common features of coastal waters (Alldredge and Silver, 1988; Alldredge et al., 2002), occurring in both surface waters, and – unlike phytoplankton – at depths well below the euphotic zone (e.g., Ransom et al., 1998). However, little work has been conducted on acoustic estimates of these abundant and densely aggregated particles, though there are anecdotal references in the acoustic literature (e.g., Anoshkin and Goncharov, 1993).

One approach to understanding the sources of reflected sound is to combine optic and acoustic methods, orienting the sensors so that a common volume is observed by both modalities. Such an instrument, combining *in situ* stereoscopic imaging with simultaneous measurement of acoustic reflectivity, was described by Briseño-Avena et al. (2015). Here we used data acquired by that system to provide evidence for the acoustic reflectivity of phytoplankton, marine snow, and small gelatinous organisms (350 μm – 24 mm).

4.3. Material and Methods

4.3.1. ZOOPS-O^2 system description

ZOOPS-O^2 is a broadband, ultra high-frequency (1.5-2.5 MHz) system that combines an instrument to measure the acoustic reflectivity of individual targets

(ZOOPS) with two cameras giving concurrent stereo visual images of the targets reflecting sound (O-Cams) (Briseño-Avena et al., 2015). Using the system, data triplets (image pairs and their acoustic signal envelope) were acquired. Here we present examples of the data showing a diverse suite of targets detected by the system. Data in this section were extracted from 7 (18,347 image pairs) out of a total of 19 (42,779 total image pairs) profiles performed during a cruise aboard RV New Horizon on March 28-29, 2012 in the Southern California Bight. A CTD (SBE 911 plus) equipped with a fluorometer (Seapoint Chlorophyll Fluorometer) was mounted on the ZOOPS-O^2 platform for this fieldwork. The profiles were conducted at inshore (Scripps Canyon) and offshore (San Diego Trough) locations. Maximum cast depths ranged between 40 m and 500 m, the maximum operational depth of the package.

4.3.2. Manual counting and identification of zooplankton and marine snow particles

Images from the O-Cam 1 were manually processed by visually identifying and counting zooplankton and marine snow particles in each image displayed in Matlab. Particles were sorted into 22 categories or groups (e.g., euphausiids, calanoid copepods, jellyfish, marine snow, etc.). Abundance estimates (individuals per mL) for each category were obtained by dividing the number of organisms or particles per image by the individual camera's imaged volume (~106 mL).

4.3.3. Diatom-like particles image identification and quantification

The ZOOPS-O^2 images were processed to identify the number of diatom-like particles and their three-dimensional locations. A subset of images was used to construct a training set of diatom-like particles by manually selecting the objects identified by a user as centric diatoms. Next, the particle moments (i.e., centroid, area, major and minor axes, aspect ratio) of the manually selected objects were obtained with the function '*regionprops'* in Matlab. Finally, the moment statistics were used to automatically detect diatom-like particles in images from the O-Cams (Fig. 4.1). Visual inspection of at least 100 randomly selected image pairs corroborated that automatic processing was accurate in identifying the centric diatoms. Then, using the stereoscopic calibration described in Briseño-Avena et al. (2015), corresponding diatom-like particles found within the stereoscopic volume were identified from the image pairs (Fig. 4.1a, green circles). That is, when a red cross (O-Cam 1 image) overlapped a green circle (predicted location in the stereoscopic volume) that particle was considered to have been imaged by both cameras and thus present in the stereoscopic volume (Fig. 4.1c). The remaining particles were considered to be outside of this common volume and were not quantified. As expected, this process resulted in a drop in the total counts of diatom-like particles, as the stereoscopic volume is approximately 1/5 of the volume imaged by each camera independently. Diatom-like particle abundance was then estimated by dividing the total diatom-like particle counts (Fig. 4.2c) by the stereoscopic imaged volume (~20.0268 mL).

4.3.4. *In situ* acoustic reflections

4.3.4.1. Individual zooplankton and marine snow acoustic reflections

The 18,347 image pairs and their accompanying acoustic records were processed using the 'echo-locator' algorithm method reported in Briseño-Avena et al. (2015). A brief description of the method is provided here. The ZOOPS-O^2 stereoscopic volume intercepted the acoustic beam at ranges 0.84-0.88 m, thus the acoustic records containing echoes at those ranges with Broadband Target Strength (BTS) at or above -120 dB were extracted for further processing. The image pairs were shown side by side along with their corresponding echogram. Once the identified acoustic target was confirmed to be in the stereoscopic volume, its acoustic range was calculated from the images, and the corresponding echo peak was identified in the echogram. The echo statistics were extracted and saved for further analysis. Table I summarizes the basic statistics for the particles whose echoes were successfully located.

4.3.4.2. Zooplankton and marine snow acoustically derived abundance estimates

Previous studies have shown that ZOOPS-O^2 is capable of detecting echoes from individual targets. Here, we used those echoes to estimate the abundance of acoustically reflective targets whose broadband target strength (BTS) was above -120 dB and whose size was in the 350 μm – 24 mm range. The targets were identified as zooplankton and marine snow particles (Table I). Abundance estimates were calculated by counting the number of targets found in the full acoustic range of the

system and dividing the total target counts by the acoustic beam volume (1L). Estimates are reported as individuals per mL.

4.3.4.3. Diatom acoustically derived abundance estimates

To test the ability of ZOOPS-O^2 to detect phytoplankton aggregated in high densities, the abundance estimates obtained from the automated diatom-like particle detection algorithm were compared with the acoustic reflectivity. One profile, where bulk fluorescence was dominated by centric diatoms (*Coscinodiscus* sp.), is used for this comparison. Given that the system's acoustic detection threshold is above -130 dB, and the fact that most zooplankton identified here had BTS values above -123 dB, we exploited this 7 dB difference to test for the presence of a signal originating from these diatoms. The number of peaks detected in this 7 dB interval was divided by the estimated acoustic volume (53.74 mL) of the beam between ranges 0.84 and 0.88 m (the range intercepted by the stereoscopic volume) to obtain acoustic estimates of diatom-like target abundance, reported here as targets per mL.

4.4. Results and Discussion

After rigorous examination and selection, only 377 image pairs (out of 18,347) clearly showed a common planktonic particle whose position also yielded an unambiguous echo in the acoustic record. From these image pairs we found a diverse suite of *echogenic* targets (Fig. 4.2). Surprisingly, we found that small gelatinous organisms (e.g., hydromedusae, doliolids, ctenophores, chaetognaths,

appendicularians) were acoustically reflective. Most unexpectedly we found that phytoplankton and marine snow aggregates can contribute to the echoes sensed by a broadband, high frequency system (1.5-2.5 MHz).

4.4.1. Zooplankton and marine snow acoustic reflectivity

There was an unexpectedly diverse group of targets whose echoes were detectable at 1.5-2.5 MHz (Table I). While we obtained expected echoes from individual crustacean zooplankton (e.g., copepods, euphausiids, mysids; Fig. 4.2) we were surprised to see gelatinous organisms (e.g., hydromedusae, doliolids, chaetognaths, appendicularians; Fig. 4.3) and marine snow particles (Fig. 4.4) in the acoustic records. Phytoplankton were also present in the acoustic and stereoscopic records, but this group was treated differently (see below). Interestingly, we found that despite the size range of the targets, there was a general overlap of broadband target strength (BTS) values for all categories (Table I). This suggests that at frequencies 1.5-2.5 MHz, and using only target strength (TS), a large marine snow particle (Fig. 4.4b) can be as acoustically reflective as – and be confounded with – some crustacean zooplankton (Fig. 4.2).

Marine snow layers are commonplace features in coastal oceans, yet their contribution to acoustic returns in field surveys seems to be virtually unexplored. Importantly, these layers can have intense biological activity. For example, the coincidence of marine snow layers, copepods, and their predators have been documented in the Baltic Sea using underwater optics (Möller et al., 2012). In light of

the present results, the collocation of such targets can complicate acoustic processing and interpretation, potentially leading to an over-estimate, for example, of copepod abundance.

While the TS of some gelatinous organisms has been measured, most studies have focused on physonect siphonophores (a colonial pelagic cnidarian with a pneumatophore or "float", filled mostly with carbon monoxide): the air-filled pneumatophore strongly scatters sound. The TS of large jellysfish has also been measured using narrowband frequencies centered at 120 and 200 kHz (*Aurelia aurita*, umbrella diameter: 9.5-15.5 cm; Mutlu, 1996), and at 18, 38, and 120 kHz (*Chrysaora hysoscella* (5-8.5 cm), and *Aequorea aequorea* (10-61 cm); Brierley et al., 2005). The hydromedusae measured in the present study were much smaller, ranging from 0.2 to 2.4 cm. Notice that at frequencies of 1.5-2.5 MHz, the TS of a large gelatinous organism (Fig. 4.3a) could lead it to be misinterpreted as a medium-sized copepod (Fig. 4.2a). However, notice that the shape of the echo envelope (Fig. 4.2 and 4.3, red lines on overlapping plots) is qualitatively different between these two groups. At present, however, generally only measurements related to the TS of targets are utilized in the acoustic community. While the properties of the echo envelope related to each individual target is under investigation, this is a cautionary tale for interpreting acoustic data from emerging broadband technologies, and even more significantly, single, narrowband technologies that rely on echo-integrating principles. As we have shown, many unexpected taxa have the potential to contribute to acoustic signals.

4.4.2. Phytoplankton acoustic reflectivity

To explore whether diatoms in high densities (as those most likely to be observed in thin layers) are capable of reflecting sound we used a profile in which centric diatoms dominated the bulk fluorescence signal (Fig. 4.5a, b). A water sample taken at the depth of the chlorophyll maximum and later inspected under a microscope confirmed that the phytoplankton assemblage was comprised of the centric diatom *Coscinodiscus* sp. In the camera system the centric diatoms were clearly distinguishable as circular targets when viewed end-on, and in side view both thecae (Petri dish-like shape) were obvious. Here we refer to these imaged centric diatoms as diatom-like particles due to the image processing method utilized (see material and methods). However, no other phytoplankton types were apparent in the image records, suggesting the layer was dominated by a single species. The maxima of these diatom-like particles peaked in the same depth interval as the fluorescence, suggesting that these diatoms were the source of the fluorescence signal (Fig. 4.5b). Stereoscopically derived abundance estimates of the centric diatoms fall within the range observed in the SCB region (e.g., Venrick, 2012). Diatom-like abundances derived from the stereoscopic system revealed that there were actually two, rather than one, diatom abundance peaks (Fig. 4.5c, green dotted line). Most interestingly, we found an increase in the acoustic signal coincident with both abundance peaks, supporting the hypothesis that diatoms were the source of the acoustic signal.

Dense phytoplankton aggregations are often areas of intense grazing, and increased abundances of zooplankton within or near the observed diatom peaks might be expected. However, acoustically (targets whose BTS > -120 dB; Table I) and optically derived abundance estimates (see material and methods) of zooplankton and marine snow traced each other (Fig. 4.5c, solid black line and red dotted line, respectively), and their abundances did *not* peak at the location of the diatom abundance peaks. This suggested that neither zooplankton nor marine snow were the cause of the increased acoustic signals found within the diatom peaks (Fig. 4.5c, solid blue line). This further supported the hypothesis that the high concentration of diatoms was responsible for the broadband, high-frequency (1.5-2.5 MHz) signal detected by the ZOOPS-O^2 system.

One other potential source of the acoustic signal in the layers is thermal microstructure. Phytoplankton abundances are often found to vary with thermal structure (Gessner, 1948; Derenbach et al., 1980). Acoustic scattering associated with the thermocline, for example, had been reported as early as 1958 (Weston). It has also been found that thermal structures are sensed by wide-band systems at high and ultra-high frequencies (Holliday and Pieper, 1980; Lavery et al., 2010). The coincidence of biological and thermal structures has been recognized since early acoustic underwater research (Cushing et. al., 1956; Cushing and Richardson, 1956; Tveite, 1969). Given that ZOOPS-O^2 is a wide-band system operating at 1.5-2.5 MHz, we wanted to rule out the possibility that the acoustic signal in the profile in figure 4.3c (blue solid line) was due to thermal microstructure.

To test this, temperature, acoustic and optic diatom-like abundance data were binned over 1 meter, and temperature gradients estimated by measuring the change in temperature (ΔT) over 1 m depth (ΔZ) (Fig. 4.6, thin black solid line). Three main sharp temperature gradients were apparent (Fig. 4.6, dotted horizontal lines). The first (Fig. 4.6, feature labeled 1) was found above the diatom peaks, and the two subsequent ones (Fig. 4.6, features labeled 2 and 3) at the top and bottom of the two diatom-like peaks. If the increase in the acoustic signal (Fig. 4.6, blue line) were solely a response to the sharp temperature structure, one would expect to see three corresponding acoustic peaks. However, the acoustic signal did not experience a drop where there were no sharp temperature gradients. In contrast, high values of diatom-like particles were observed in that depth interval. This suggested that temperature microstructure was not the main the source of the observed acoustic return in the -130 to -123 dB signal. Furthermore, a simple regression showed that variations in the acoustic data were better explained by the stereoscopic diatom-like abundance ($r^2 = 0.8522$) than by thermal gradients ($r^2 < 0.07$). While this does not rule out the possibility of thermal microstructure contributing to some degree to the acoustic signal, our analyses suggest that the increase in the acoustic returns is primarily due to the presence centric diatoms.

Interestingly, the relationship between optic-derived densities and acoustic-derived densities of diatom-like particles was not linear (Fig. 4.5c, inset). This suggests that at high centric diatoms concentrations the observed acoustic signal became saturated, no longer reflecting the echoes of individual diatoms, but rather

integrating over multiple targets. We did not pursue volume backscatter relationships in this paper, and they remain a topic for further study.

4.5. Conclusions

In this chapter it has been shown that gelatinous and marine snow individual targets are capable of reflecting broadband, high frequency (1.5-2.5 MHz) acoustic energy. We also showed that diatoms in high concentrations were capable of reflecting sound at these high frequencies. Knowing that diatom and marine snow layers are conspicuous and recurrent features in coastal areas, the results of this work suggest that such particles should be taken into account during acoustic surveys. Furthermore, concentrations of gelatinous organisms (jellyfish, siphonophores, doliolids and salps – although no salps where observed in the present work) can be significant and dominate the zooplankton at times (e.g., Richardson et al., 2009; Everett et al., 2011; Alvarez Colombo et al., 2014). The reflectivity of such organisms observed in this work indicates they should be more carefully considered during research acoustic surveys.

The emergence of commercially available wide-band technologies creates new opportunities for the use of processing methods for interpreting acoustic data. While not fully considered in the present work, the properties of acoustic echoes (e.g., the echo envelope; see red lines in Figs. 4.2, 4.3, and 4.4) can add more degrees of freedom to acoustic target classification. The information contained in such acoustic envelopes could be a rich area for future exploration to improve target discrimination.

The results presented here underscore the need to exercise caution when interpreting acoustic data based solely on target strength measurements.

In the future, ZOOPS-O^2 could be used to carry out experiments to compare the *in situ* versus modeled BTS and spectra of organisms such as euphausiids, mysids, and chaetognaths, as Briseño-Avena et al. (2015) did for copepods. Such exercises will be useful to refine extant models and consider more complex body shapes.

Future field biological surveys should incorporate a suite of technologies including acoustic, optic, and net systems to capture a more complete picture of planktonic distributions. In light of the present observations, a zooplankton survey using acoustics should clearly take into account phytoplankton and marine snow. While nets target a finite size-range of planktonic organisms, retaining large particles and destroying fragile organisms and marine snow particles, optic cameras are complementary because of their non-invasive capabilities. Furthermore, nets cannot resolve the fine spatial scales at which phytoplankton and marine snow layers occur. Optical tools, on the other hand, can be used to detect such ubiquitous features and provide ground truthing information for acoustic studies that might be affected by phytoplankton, marine snow and fragile, gelatinous taxa.

Chapter 4, in full, is currently being prepared for submission for publication of the material. Briseño-Avena, C., Franks, P.J.S., and Jaffe, J.S. The dissertation author was the primary investigator and author of this paper.

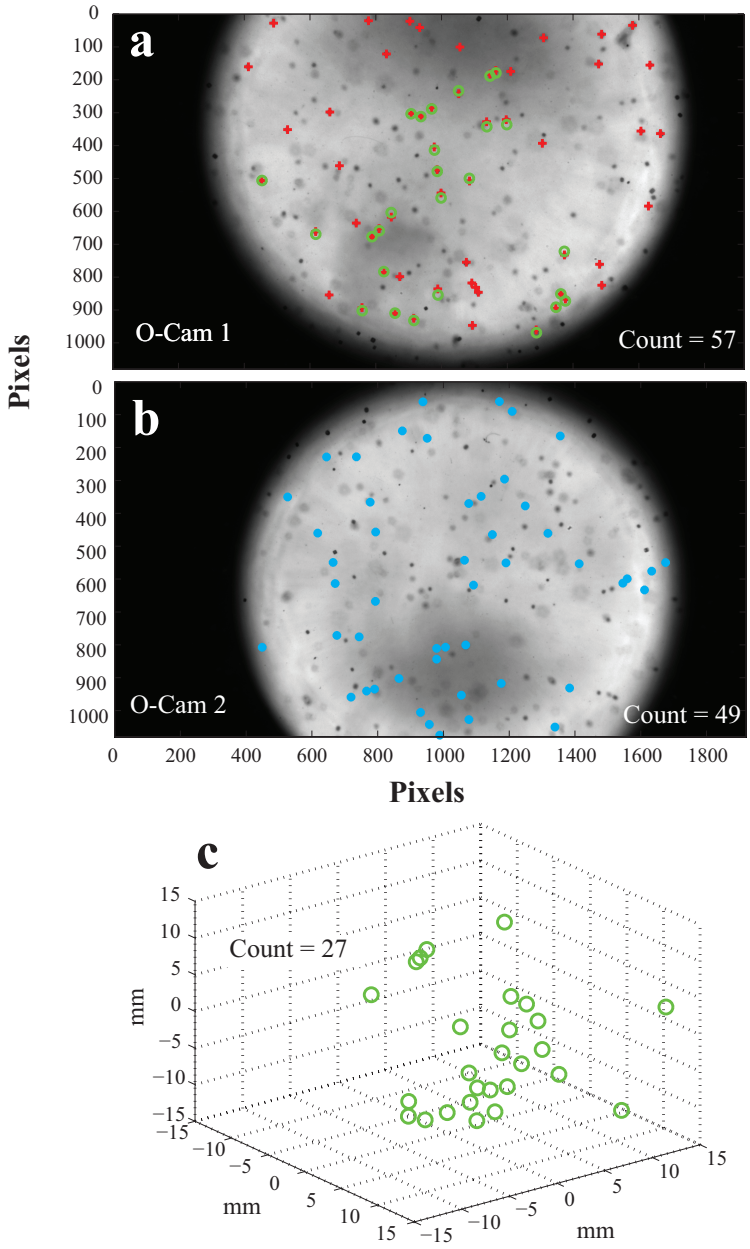

Figure 4.1. Result of the diatom-like particle detection. (a) and (b) are images from the two O-Cams showing the automatic detection of diatom-like particles (red crosses in (a) and blue dots in (b)). Green circles that overlap the red crosses in (a) indicate the diatom-like particles that have a corresponding particle in (b). Counts in (a) and (b) are the total number of diatom-like particles identified by the automatic detection algorithm. (c) Total diatom-like particles and their three-dimensional locations in the stereoscopic volume.

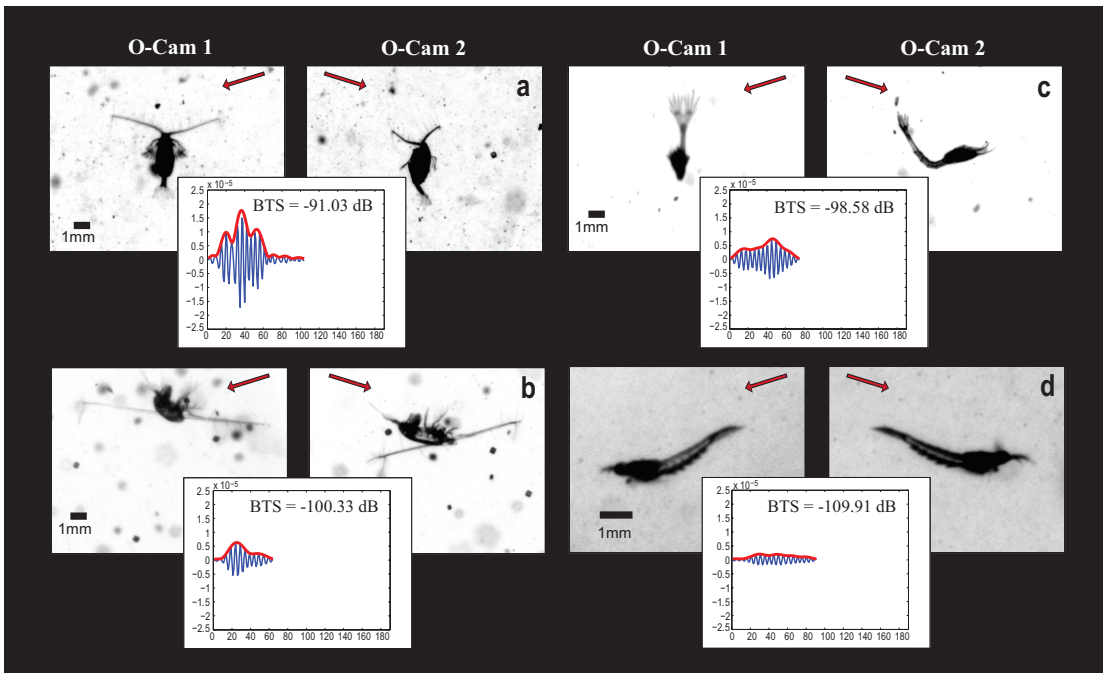

Figure 4.2. Examples of crustacean zooplankton whose broadband target strength (BTS in dB) was measured *in situ* with ZOOPS-O^2. For each triplet: left image= O-Cam 1, right image= O-Cam 2, overlapping plot = echo signal (blue line) and echo envelope (red line). Scale bars are given for each image pair. For all echo envelope plots the *x*-axis is time and *y*-axis is Voltage; all of them are standardized to the same scale. Peak BTS is also noted for each target. The red arrows indicate the direction the acoustic beam is hitting the imaged particle. (a) Calanoid copepod; (b) Eucalanid copepod; (c) Mysid; (d) Euphausiid.

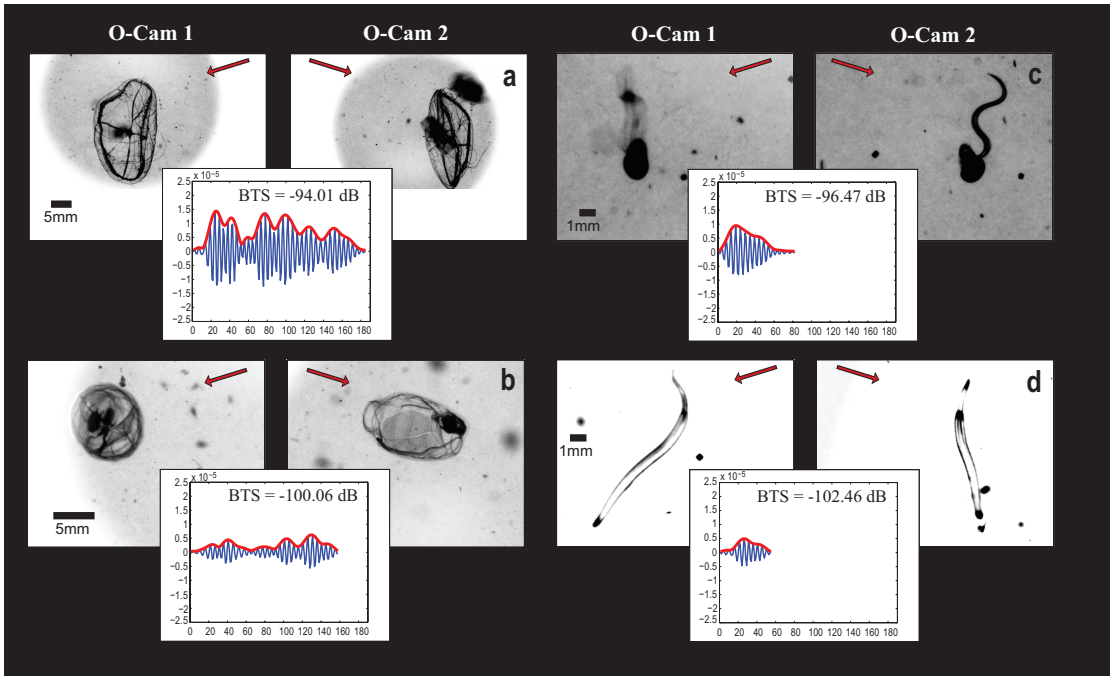

Figure 4.3. Examples of gelatinous and other fragile zooplankton whose broadband target strength (BTS in dB) was measured *in situ* with ZOOPS-O^2. Legend the same as figure 4.2. (a) Hydromedusa; (b) Doliolid; (c) Appendicularian; (d) Chaetognath.

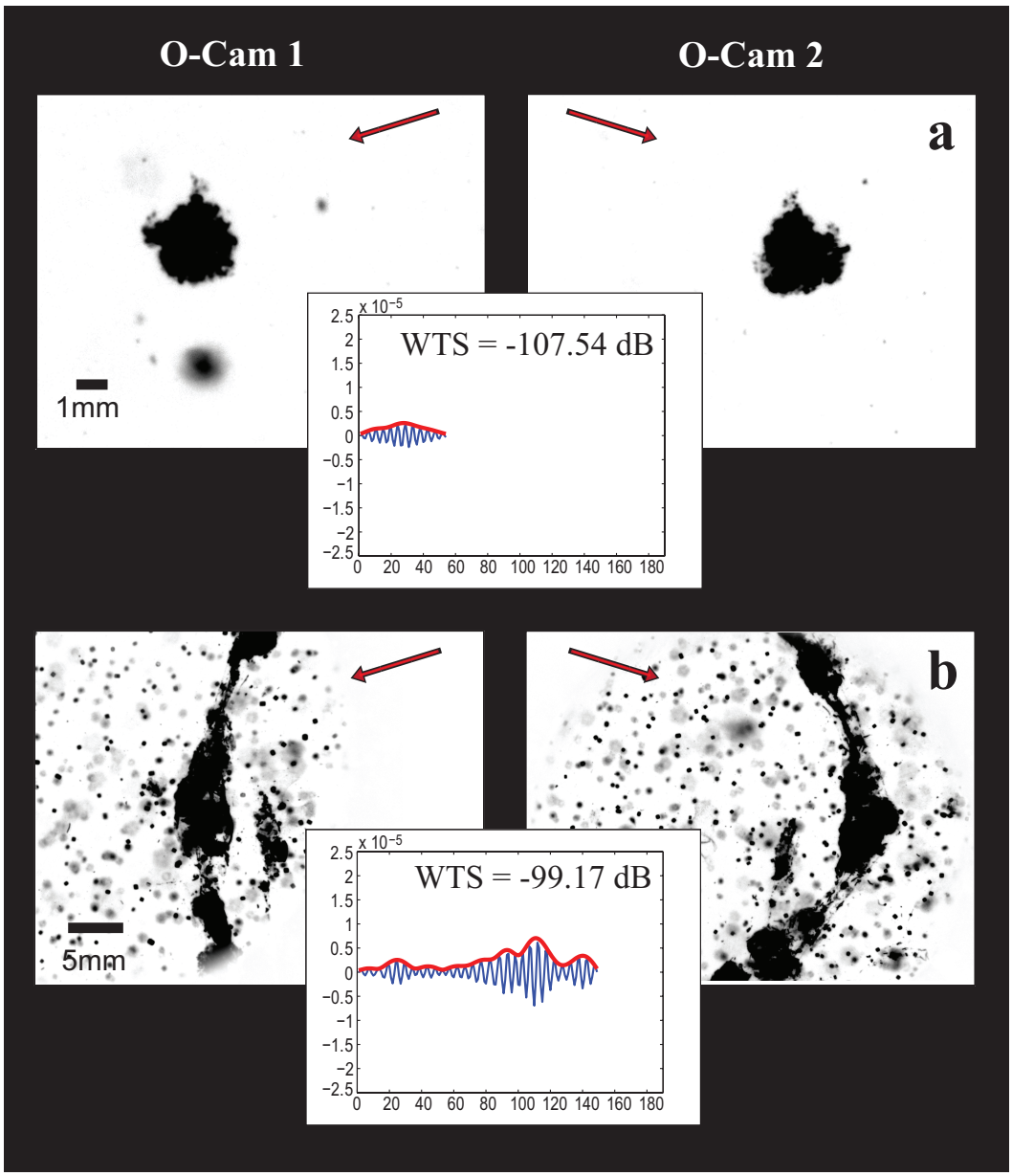

Figure 4.4. Examples of small (a) and large (b) marine snow particles whose broadband target strength (BTS in dB) was measured *in situ* with ZOOPS-O^2. Legend the same as figure 4.2.

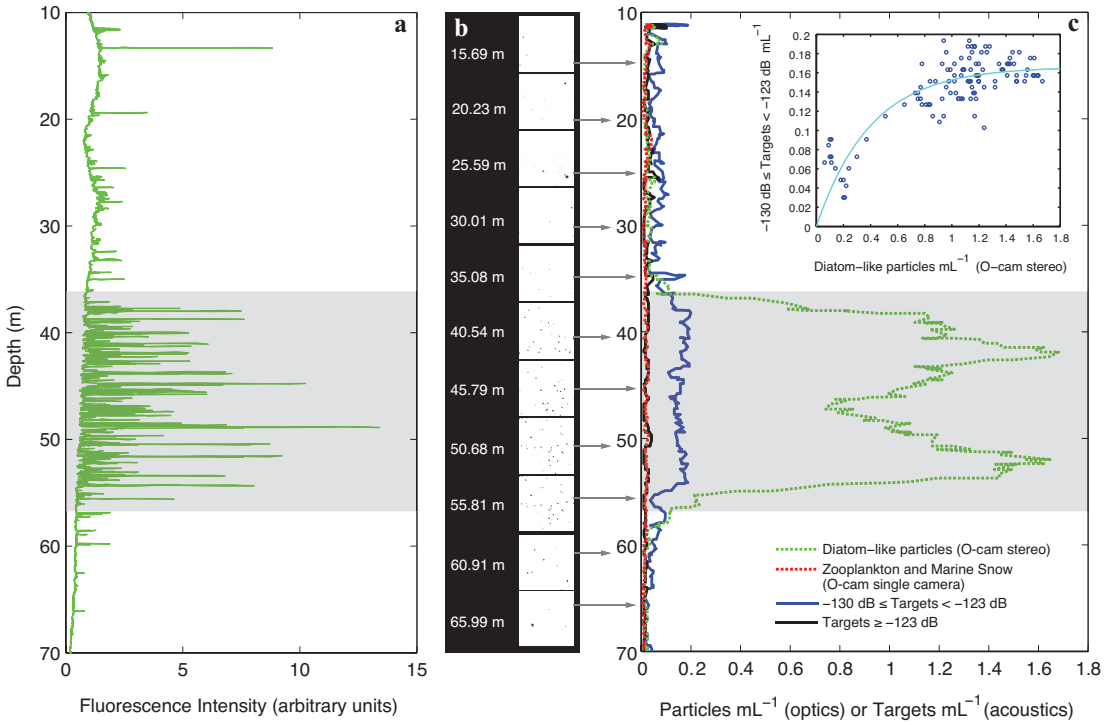

Figure 4.5. Acoustic reflections from two thin peaks of large centric diatoms sampled on March 28, 2012. (a) Fluorescence intensity profile; (b) images from O-Cam 1; (c) ZOOPS-O^2 profiles comparing optic (doted lines) and acoustic (solid lines) data; black solid line represent targets in the range of zooplankton and marine snow (BTS > -123 dB); red dotted line represents zooplankton and marine snow counts from one O-Cam; blue solid line indicates abundance estimates from acoustic data from targets whose BTS ranged between -130 and – 123 dB (diatom-like targets). Inset in (c) shows the relationship between optic and acoustic estimates of diatom densities.

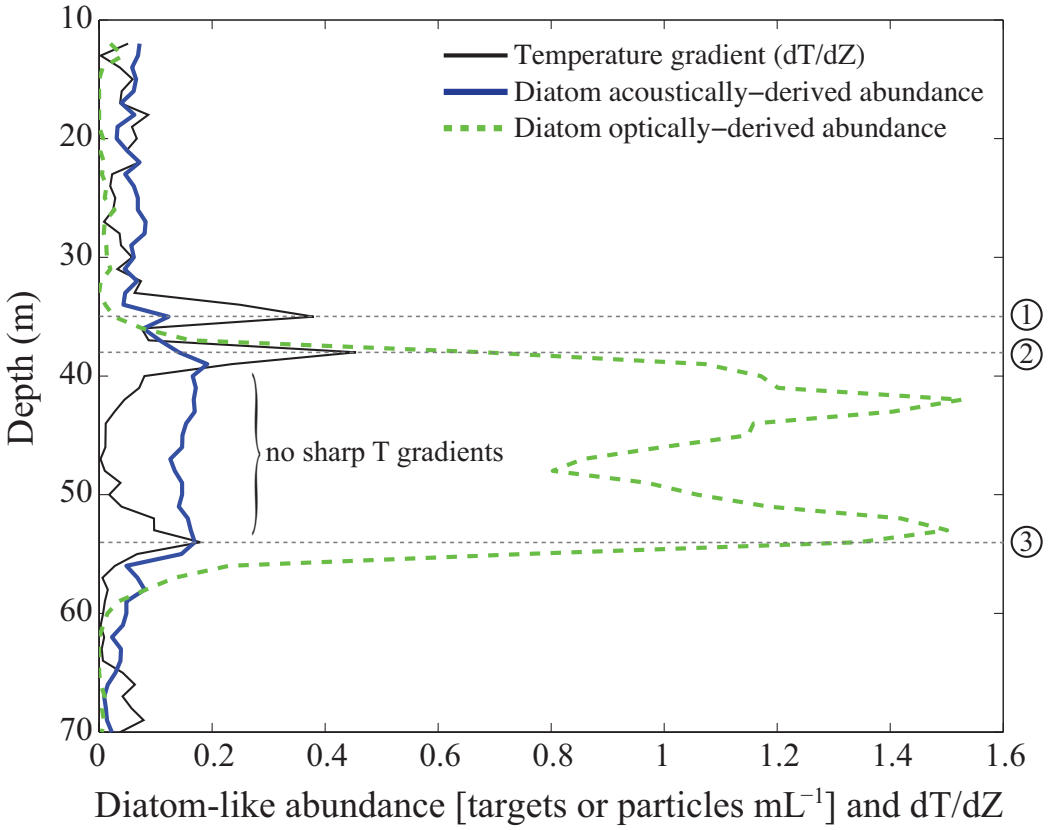

Figure 4.6. Optically and acoustically derived diatom-like abundance (green dashed line and blue solid line, respectively) and temperature gradients ($\Delta T/\Delta Z$; thin black solid line) for the same profile shown in figure 4.5. The three sharpest gradients in temperature are indicated by horizontal dashed lines and labeled with circled numbers 1, 2, and 3 on the secondary *y*-axis.

Table 4.1. *In situ* BTS (dB) measured from individual targets from ZOOPS-O[2].

Taxa of Category	Sample size (n)	Length (mm)	Range of BTS (dB)	Mean BTS (dB)	Standard Deviation
Copepods[a]	224	0.36 – 4.47	-111.54 to -84.14	-101.60	± 6.82
Marine Snow	90	0.92 – 11.09	-111.60 to -94.78	-107.66	± 4.15
Appendicularians[b]	28	1.95 – 11.54	-111.20 to -93.78	-104.10	± 4.83
Doliolids	15	2.7 – 12.47[f]	-111.71 to -86.98	-102.10	± 4.29
Gelatinous[c]	10	2.27 - 24.08[g]	-111.70 to -92.97	-101.92	± 7.15
Chaetognaths	4	8.73 - 17.73	-112.84 to -96.51	-105.08	± 7.13
Siphonulae[d]	3	~1.02	-96.04 to -93.89	-95.33	± 1.24
Euphausiids[e]	2	~3.91	-109.91 to -101.54	-105.73	± 5.92
Ctenophores	1	~8.43	-105.77	N/A	N/A
Ostracods	1	~1.48	-103.93	N/A	N/A

[a]Mostly calanoid and poecilostomatoid copepods. It may include early developmental stages. Length of copepods is the estimated prosome length.
[b]Including individuals with and without their "house".
[c]Mainly hydromedusae.
[d]An early developmental stage of siphonophores.
[e]Small euphausiids (probably juvenile stages).
[f]Diameter not measured.
[g]Bell diameter.

4.6. References

Alldredge, A.L., Cowles, T.J., MacIntyre S., Rines, J.E.B., Donaghay, P.L., Greenlaw, C.F., Holliday, D.V., Dekshenieks, M.M., Sullivan, J.M., and Zaneveld, J.R.V. 2002. Occurrence and mechanisms of formation of a dramatic thin layer of marine snow in a shallow Pacific fjord. Marice Ecology Progress Series. 233: 1-12.

Alldredge, A.L. and Silver, M.W. 1988. Characteristics, dynamics and significance of marine snow. Progress in Oceanography, 20: 41-82.

Anoshkin, A.F. and Goncharov, V.K. 1993. Submersible vehicle investigation of sound scattering layers and hypotheses about their physical nature. Acoustical Physics, 39: 302-306.

Benfield, M.C., Wiebe, P.H., Stanton, T.K., Davis, C.S., Gallager, S.M., and Greene, C.H. 1998. Estimating the spatial distribution of zooplankton biomass by combining Video Plankton Recorder and single-frequency acoustic data. Deep-sea Research II, 45: 1175-1199.

Bok, T., Na, J., and Paeng, D. 2013. Diel variation in high frequency acoustic backscatter from *Cochlodinium polykrikoides*. Journal of the Acoustic Society of America, 134, EL140-146.

Bok, T., Paeng, D., Na, J., and Kang, D. 2010. Ultrasound backscatter power from *Cochlodinium polykrikoides*, the main red tide species in the Southern Sea of Korea. Journal of Plankton Research, 32: 503-514.

Brierley, A. S., Boyer, D.C., Axelsen, B.E., Lynam, C.P., Sparks, C.A.J., Boyer, H.J., and Gibbons, M.J. 2005. Towards the acoustic estimation of jellyfish abundance. Marine Ecology Progress Series, 295: 105-111.

Briseño-Avena, C., Roberts, P.L.D., Franks, J.S.P., and Jaffe, J.S. (2015). ZOOPS-O^2: A broadband echosounder with coordinated stereo optical imaging for observing plankton *in situ*. Methods in Oceanography, 12: 36-54.

Alvarez Colombo, G., Benovic , A., Malej, A., Lucic, D., Makovec, T., Omofri, V., Acha, M., Madirolas, A., and Mianzan, H. 2009. Acoustic survey of a jellyfish-dominated ecosystem (Mljet Island, Croatia). In Pitt, K.A., and Purcell, J.E. (eds.) Jellyfish Blooms: Causes, Consequences, and Recent Advances. Developments in Hydrobiology, 206: 99-111.

Cowles, T.J., Desiderio, R.A., and Carr, M. 1998. Small-scale planktonic structure: persistence and trophic consequences. Oceanography, 11: 4-9.

Cushing, D.H. and Richardson, I.D. 1956. A record of plankton on the echo-sounder. J. Mar. Biol. Ass. U.K., 35: 231-240.

Cushing, D.H., Lee, A.J., and Richardson, I.D. 1956. Echo traces associated with thermonclines. ICES Journal of Marine Research, 15: 1-13.

De Monte, S., Soccodato, A., Alvain, S., and d'Ovidio, F. 2013. Can we detect oceanic biodiversity hotspots from space? International Society for Microbial Ecology, 7: 2054-2056.

Derenbach, J.B., Astheimer, H., Hansen, H.P., and Leach, H. 1979. Vertical Microscale Distribution of Phytoplankton in Relation to the Thermocline. Marine Ecology Progress Series, 1: 187-193.

Everett, J.D., Baird, M.E., and Suthers, I.M. 2011.Three-dimensional structure of a swarm of the salp *Thalia democratica* within a cold-core eddy off southeast Australia. Journal of Geophysical Research, 116: C12046.

Fernandes, P.G., Gerlotto, F., Holliday, D.V., Nakken, O., and Simmonds, E.J. 2002. Acoustic applications in fisheries science: the ICES contribution. ICES Marine Science Symposia, 213: 483-492.

Fielding, S., Griffiths, G., and Roe, H.S.J. 2004. The biological validation of ADCP acoustic backscatter through direct comparison with net samples and model predictions based on acoustic-scattering models. ICES Journal of Marine Science, 61: 184-200.

Fornshell, J.A. and Tesei, A. 2013. The Development of SONAR as a Tool in Marine Biological Research in the Twentieth Century. International Journal of Oceanography, 2013: 1-9, DOI: 678621.

Gessner, F. 1948. The vertical distribution of phytoplankton and the thermocline. Ecology, 29: 386-389.

Holliday, D.V. and Pieper, R.E. 1980. Volume scattering strengths and zooplankton distributions at acoustic frequencies between 0.5 and 3 MHz. Journal of the Acoustic Society of America, 67: 135-146.

Lara-Lopez, A. and Neira, F.J. 2008. Synchronicity between zooplantkton biomass and larval fish concentrations along a highly flushed Tasmanian estuary:

assessment using net and acoustic methods. Journal of Plankton Research, 30: 1061-1073.

McManus, M.A., Alldredge, A.L., Barnard, A.H., Boss, E., Case, J.F., Cowles, T.J., Donaghay, P.L., Eisner, L.B., Gifford, D.J., Greenlaw, C.F., Herren, C.M., Holliday, D.V., Johnson, D., MacIntyre, S., McGehee, D.M., Osborn, T.R., Perry, M.J., Pieper, R.E., Rines, J.E.B., Smith, D.C., Sullivan, J.M., Talbot, M.K., Twardowski, M.S., Weidemann, A., and Zaneveld, J.R. 2013. Characteristics, Distribution and Persistence of Thin Layers Over a 48 Hour Period. Marine Ecology Progress Series, 261: 1-19.

Möller, K.O., St. John, M., Temming, A., Floeter, J., Sell, A.F., Herrmann, J., and Möllmann, C. 2012. Marine snow, zooplankton and thin layers: indications of a trophic link from small-scale sampling with the Video Plankton Recorder. Marine Ecology Progress Series, 468: 57-69.

Moriarty, R. and O'Brien, T.D. 2013. Distribution of mesozooplankton biomass in the global ocean. Earth Syst. Sci. Data, 5: 45-55.

Mutlu, E. 1996. Target strength of the common jellyfish (*Aurelia aurita*): a preliminary experimental study with a dual-beam acoustic system. ICES Journal of Marine Science, 53: 309-311.

Powell, J.R. and Ohman, M.D. 2012. Use of glider-class acoustic Doppler profilers for estimating zooplankton biomass. Journal of Plankton Research, 34: 563-568.

Ransom, B., Shea, K.F., Burkett, P.J., Bennet, R.H., and Baerwald, R. 1998. Comparison of pelagic and nepheloid layer marine snow: implications for carbon cycling. Marine Geology, 150: 39-50.

Richardson, A.J., Bakun, A., Hays, G.C., Gibbons, M.J. 2009. The jellyfish joyride: causes, consequences and management responses to a more gelatinous future. Trends in Ecology and Evolution, 24: 312-322.

Stanton, T. K. 2012. 30 years of advances in active bioacoustics: *A personal perspective*. Methods in Oceanography, 1-2: 49-77.

Selivanovsky, D.A., Stunzhas, P.A. and Didenkulov, I.N. 1996. Acoustical investigation of phytoplankton. ICES Journal of Marine Science, 53: 313-316.

Sutor, M., Cowles, T.J., Peterson, W., and Lamb, J. 2005. Comparison of acoustic and net sampling systems to determine patterns in zooplankton distributions. Journal of Geophysical Research, 110: C10S16.

Timmerman, A.H.V., McManus, M.A., Cheriton, O.M., Cowen, R.K., Greer, A.T., Kudela, R.M., Ruttenberg, K., and Sevadjian, J. 2014. Hidden thin layers of toxic diatoms in a coastal bay. Deep-Sea Research II, 101: 129-140.

Tveite, S. 1969. Zooplankton and the discontinuity layer in relationto echo traces in the Oslofjord. Fisk. Dir. Skr. Ser HauUnders, 15: 25-35.

Warren, J.D. and Smith, J.N. 2007. Density and sound speed of two gelatinous zooplankton: Ctenophore (*Mnemiopsis leidyi*) and lion's mane jellyfish (*Cyanea capillata*). J. Acoust. Soc. Am. 122: 574-580.

Weston, D.E. 1958. Observations on a scattering layer at the thermocline. Deep-Sea Research, 5: 44-50.

Wiebe, P.H., Mountain, D.G., Stanton, T.K., Greene, C.H., Lough, G., Kaartvedt, S., Dawson, J., and Copley, N. 1996. Acoustical study of the spatial distribution of plankton on Georges Bank and the relationship between volume backscattering strength and the taxonomic composition of the plankton. Deep-Sea Research II, 43: 1971-2001.

CHAPTER 5

First observation of the rhizarian *Paradinium poucheti* parasitizing the copepod *Oithona similis* in the Pacific Ocean: evidence from a moored *in situ* camera

Christian Briseño-Avena

5.1 Abstract

Parasites of pelagic copepods can reduce fecundity, increase mortality, and reduce fecal pellet nutrient content, potentially affecting carbon export. However, parasite prevalence in copepods has been received little attention. Images from a moored, *in situ* camera were used to make the first observations of *Oithona similis* parasitized by *Paradinium poucheti* in the Pacific Ocean. Time series reveal significant fluctuations in the prevalence of infection, and its relationship to the abundance of females *O. similis*.

5.2. Introduction

Copepods are the most numerous metazoans in pelagic ecosystems (and arguably on Earth; see Schminke, 2007). Parasites have been recognized as key components in shaping planktonic community structures globally (Lima-Mendez et al., 2015), yet the ecological implications of parasites on copepod populations are mostly unknown (Skovgaard, 2014). However, from the limited information available, it is clear that copepod mortality due to parasites can be devastating. For example,

Kimmerer and McKinnon (1990) reported female mortalities as high as 41% per day in a population of *Paracalanus indicus* in Port Phillip Bay, Australia. Fields et al. (2015) reported devastating effects on grazing and egg production (females are disproportionately affected) of *Calanus finmarchicus* in coastal Norwegian waters. Given the abundance of copepods in marine ecosystems, and their important role in carbon transport (Legendre and Rivkin, 2002) the reduced size in fecal pellets from parasitized copepods (Fields et al., 2015) may contribute to a decrease in carbon transport out of the euphotic zone and potentially weaken carbon sequestration in marine ecosystems. The effects of parasites can ripple through the food web, depleting the resources to carnivorous zooplanktonic predators (Ohtsuka et al., 2011).

Based on images from La Jolla, California, USA, acquired with the *in situ* Scripps Plankton Camera (SPC) I report here the first observation of *Oithona similis* Claus (1863) infected by the parasite *Paradinium pocheti* Chatton (1910). In the three decades since Ho and Perkins (1985) pointed out the limited information on the geographical occurrence of copepod parasites, and their prediction of further reports of parasites affecting copepod populations, very little has been published on parasitized copepods. An extensive literature search found no reports of *Paradinium poucheti* Chatton (1910) for the North Pacific. Alf Skovgaard (Copenhagen), an expert on *P. poucheti,* furthered confirmed that this parasite has not been reported in the Pacific Ocean, and "much less in U.S. waters where fewer works on copepod parasites have been conducted" (*pers. comm.*). Indeed, the only reports of *P. poucheti* come from the

Mediterranean Sea and the Northeast Atlantic Ocean (Skovgaard and Sainz, 2006; Skovgaard and Daugbjerg, 2008).

5.3. Materials and Methods

5.3.1. The Scripps Plankton Camera

The Scripps Plankton Camera (SPC) is a shadowgraph-type underwater microscope developed in the Jaffe Lab for Underwater Imaging (Scripps Institution of Oceanography), and installed under the Ellen Browning Scripps Memorial pier at the Scripps Institution of Oceanography, La Jolla, California, USA (Fig. 5.1). The geometry of the SPC is similar to that of the O-Cam (Briseño-Avena et al., *in press*), though the SPC acquires color images. It records images at 1 Hz, using an automatic cropping algorithm to identify and save regions of interest (ROIs), with their associated metadata (parameters including area, major and minor axis length, texture, transparency, among others.). An online server allows images and data to be interrogated for further identification and labeling of individual ROIs.

5.3.2. Quantifying *Oithona similis* and determining parasite prevalence

ROIs with objects ranging in length from 0.5 to 2 mm were visually screened to find *Oithona similis* copepods during the 58 days between March 12 (camera installation date) and July 21, 2015. The data server was interrogated for 5000 ROIs at a time for blocks of four hours (0-4, 4-8 … 20-24 hours, local time) each day. Sometimes fewer than 5000 ROIs were available in a block, and not all blocks were

inspected for every date. At least 100 copepods were counted for each date, though the present analysis includes10 dates with 57 to 93 copepods. At least two blocks were processed each day, spanning the nighttime hours 0-4 and 20-24 h when the copepods were expected to be near the surface during their diel vertical migration. When 100 ROIs had been inspected and both time blocks were processed, no further time blocks were analyzed. All *O. similis* for the block being processed were included in the counts. Once the ROIs for each date were labeled as *O. similis* (Fig. 5.2a-c), the copepods displaying the parasite's gonosphere attached to their urosome (Fig. 5.2b) were labeled; the same was done with copepods carrying egg sacs (Fig. 5.2c).

Oithona similis copepods were considered parasitized when *P. poucheti*'s gonospheres were observed attached to the end segment of the copepod's urosome (Fig. 5.2b). The gonosphere is the last stage of this parasite physically associated with the copepod (Jepps, 1937; also see Fig. 7d in Shields, 1994). This life stage is also the most obvious physical manifestation of the parasite (Fig. 5.2b). The proportion of parasitized copepods (parasite prevalence) was estimated by dividing the number of *O. similis* showing a gonosphere by the total *O. similis* counted each day. The 95% Confidence Intervals (C.I.) were estimated using the Agresti-Coull method:

$$\text{C.I.} = p_{Paradinium} \pm \left(Z_{\alpha=0.05} \sqrt{\frac{p_{Paradinium}(1 - p_{Paradinium})}{n+4}} \right) \quad (1)$$

where the $Z_{\alpha=0.05}$ deviate had a value of 1.96 and $p_{Paradinium}$ was estimated using the following equation:

$$p_{Paradinium} = \frac{\text{No. Parasitized } O.\ similis \text{ per day } + 2}{n + 4} \quad (2)$$

where *n* in (1) and (2) is the total *O. similis* counted per day.

Paradinium poucheti lives in the copepod hoemocoel; before leaving the copepod's body via the digestive system the parasite invades and destroys the female's gonads (Jepps, 1937). To test for the potential neutering capability of this parasite we quantified the presence of ovigerous females. *Oithona similis* is an egg-carrying copepod; fertilized eggs remain attached to the genital segment of the copepod until they hatch (e.g., Drif et al., 2010). Percentages of ovigerous females were estimated by dividing the number of observed egg-carrying females by the total number of *O. similis* enumerated for a given day. The 95% C.I. were estimated following (1) and (2), replacing *O. similis* with the number of egg-carrying females and $p_{Paradinium}$ with $p_{Ovigerous}$.

5.4. Results and Discussion

I was able to manually identify and classify *Oithona similis*, both with and without gonospheres (*P. poucheti*), and with and without egg-sacs (Fig. 5.2 a-c). A total of 570,556 ROIs were visually inspected, of which 10,038 were classified as *O. similis*. Of the latter, 975 were observed to have a gonosphere, and 1,591 were

observed carrying egg sacs. Egg-carrying copepods were never observed with a developed gonosphere; and *vice versa*: no copepod carrying a gonosphere was observed carrying egg sacs.

We standardized the total counts by dividing them by the total number of ROIs inspected each day. Although this method doesn't yield abundance estimates, it gives a consistent metric for the relative presence of this copepod. Though the relationship between total and relative copepod counts was linear (Fig. 5.3d), we report only the standardized values.

During the initial and final weeks of the study, the relative counts of *O. similis* were higher than the intervening period (Fig. 5.3a). The average prevalence of *P. poucheti* over the four-and-a-half-month period analyzed here was 11.70% (±6.81 1SD). This prevalence ranged from 2.83 to 32%, fluctuating between these limits during the study period (Fig. 5.3b). The percentage of ovigerous females (egg-carrying *O. similis*) over the same period was 15.96% (±6.81 % 1SD), fluctuating from 1.6% to 31.14% (Fig. 5.3c) during the study.

The 95% C.I. on the time series of the prevalence of *P. poucheti* (Fig. 5.3b) suggest that the observed variability is likely not noise or random sampling effects, but rather a real signal; the same was true for the proportion of ovigerous females (Fig. 5.3c). Note, though, that not all ROIs in the data set were inspected; a single day of sampling by the SPC can yield more than 100,000 ROIs; however, the great majority of these ROIs are smaller than 0.5 mm length. The search of ROIs in the size range 0.5-2 mm likely retrieved a representative sample of the total *O. similis* imaged by the

SPC. This system is new and automatic methods (such as Neural Networks) to classify ROIs are being developed. In the future, I envision using automated methods to extract and differentiate *O. similis* from the rest of the imaged copepods; because of the characteristic shape of the egg sacs and *P. poucheti*'s gonosphere, I believe the algorithm will also be able to differentiate egg-carrying and gonosphere-carrying *O. similis* from the non-carriers. This will make possible to obtain real-time data on this dynamic, potentially making this parasite-host relationship a model for the study of the effects of parasitism in the plankton from hours to interannual time scales.

Oithona similis is a cosmopolitan species (Razouls et al., 2015). However, reports of parasitism prevalence on this species are constrained to a few locations, mainly in the Mediterranean and Northeast North Atlantic (Skovgaard and Sainz, 2006; Skovgaard and Daugbjerg, 2008). *Paradinium poucheti*'s gonosphere development lasts only about an hour from the moment it migrates out of the copepod's digestive system, attaching itself to the urosome and finally bursting and releasing the spores into the environment (see Jepps, 1937 for a recount of Chatton's description). The transience of the gonosphere's manifestation relative to typical field sampling frequencies makes the probability of its observation low, which might explain the paucity of data on the prevalence of *P. poucheti* in copepod populations. The continuous imaging of the Scripps Plankton Camera (SPC) allows me to more reliably record this time-sensitive physical manifestation of *P. poucheti*.

Whether this phenomenon of *P. poucheti* parasitizing *O. similis* is anomalous is not yet known. The SPC was only recently deployed (March 12, 2015) and image acquisition began during anomalously warm water conditions in the Southern California Bight (SCCOOS 2014 2015 Pacific Anomalies Workshop; http://www.sccoos.org/about/meetings/). Longer time series will allow assessing parasitism intensity over longer time scales and under different hydrographic and ecological conditions. Auxiliary data will help quantifying how pervasive these parasitizing events are; the causes, triggers and environmental conditions likely to render copepods vulnerable to infection; and how parasitism changes due to natural environmental variability or to climate change. Temperature changes due to anthropogenic climate variability have altered host-parasite relationships in cases ranging from terrestrial to marine ecosystems (e.g., Harvell et al., 2002; Kutz et al., 2005; Wiedermann et al., 2007). In marine ecosystems such changes have been observed in intertidal (Studer et al., 2010; Larsen and Mouritsen, 2014), benthic (Bates et al., 2010), and nektonic (Macnab and Barber, 2012) organisms. The SPC time series could help in exploring these dynamics.

Little is known about the free-living stage of *Paradinium poucheti* and nothing is known about the life stage at which *O. similis* gets infected by this parasite. The high parasitic prevalence in copepod populations observed in the present report and its fluctuations, combined with the negative correlation between the proportion of parasitized and ovigerous females (Fig. 5.3e) suggests that *P. poucheti* has a negative effect on *O. similis* populations. This organism likely relies on its host for survival

and, rather than killing its host, it feeds on a rich component of the female copepod's anatomy: its gonads. The more females there are, the more resources available to this parasitoid. However, whether *O. similis* survives after the parasite's gonosphere bursts is not clear. The almost synchronous inverse fluctuations between parasitized and ovigerous copepods (Fig. 5.3bc) strongly suggest a parasitoid relationship between parasite and host.

Clearly, there is a need to quantify the natural abundance of *P. poucheti* and its infection rate of its host. Future work should focus on culturing the host and parasite to establish the nature of this symbiotic relationship and to further understand how the host is affected. Information on the growth rate of *P. poucheti* should also be investigated, as well as the environmental parameters controlling the development and dispersion of the parasite and its infection of its host. Answering these basic questions will be necessary to appropriately interpret the variability observed in the *Oithona similis*-*Paradinium poucheti* time series.

5.5. Acknowledgements

I would like to thank UC MEXUS and CONACyT for funding my PhD studies. Alf Skovgaard for providing definite identification of *Paradinium poucheti*. I thank Jules S. Jaffe for giving me full access to the SPC data and Peter J.S. Franks for his useful comments and for providing me with feedback on this manuscript. I also would like to express my gratitude to Ryan Hechinger for giving me a flash course on all things parasitic. The Integrated Ocean Observing System (IOOS) partially funded

the Scripps Plankton Camera and its support made possible the discovery of the seemingly pervasive phenomenon reported here.

Chapter 5, in full, has been submitted for publication as a short communication paper to Journal of Plankton Research. Briseño-Avena, C. The dissertation author was the primary investigator and solely author of this paper.

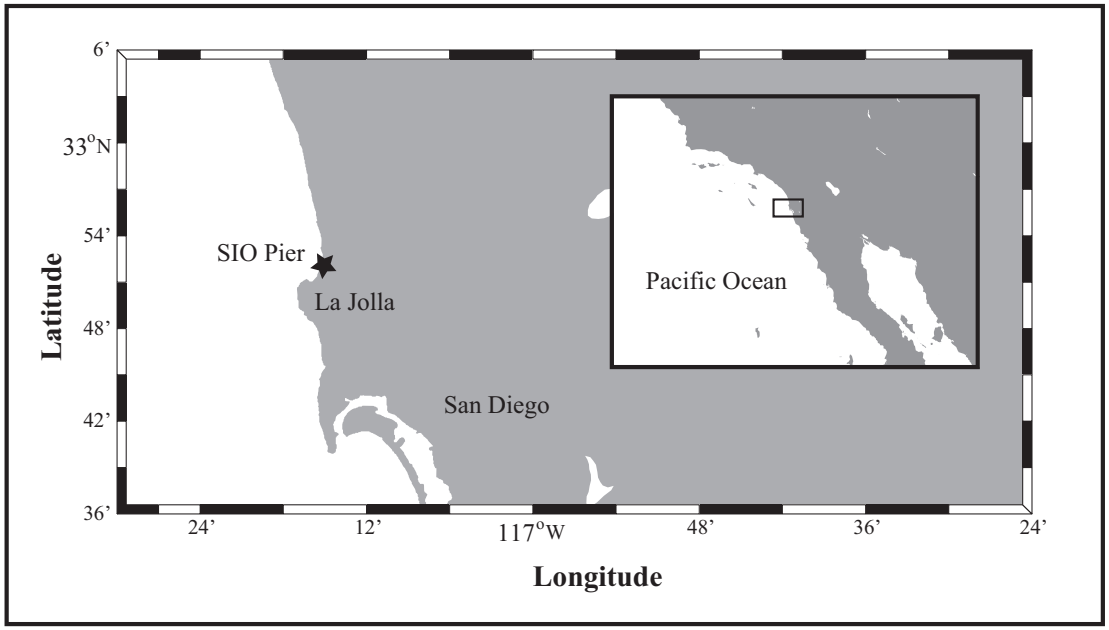

Figure 5.1. Location of the Ellen Browning Scripps Memorial pier (SIO Pier), where the Scripps Plankton Camera (SPC) is currently installed and actively collecting plankton images (spc.ucsd.edu).

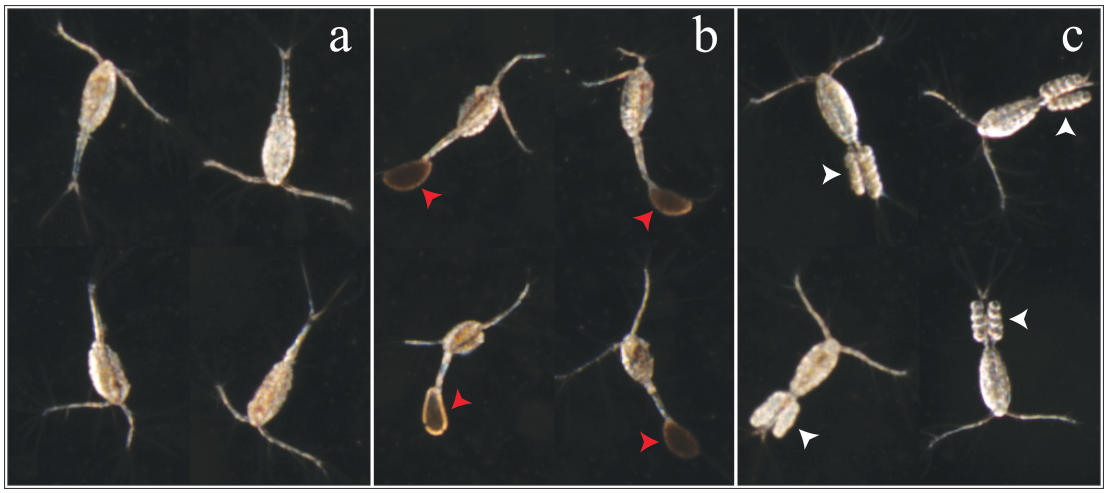

Figure 5.2. Examples of *in situ* of *Oithona similis* Regions of Interest (ROIs); a) without *Paradinium poucheti*'s gonospheres; b) with *P. poucheti*'s gonospheres (red arrowheads) attached to the end segment of their urosomes; c) with egg-sacs. Images taken by the Scripps Plankton Camera (SPC). Each panel is a collage of ROIs recorded at different times.

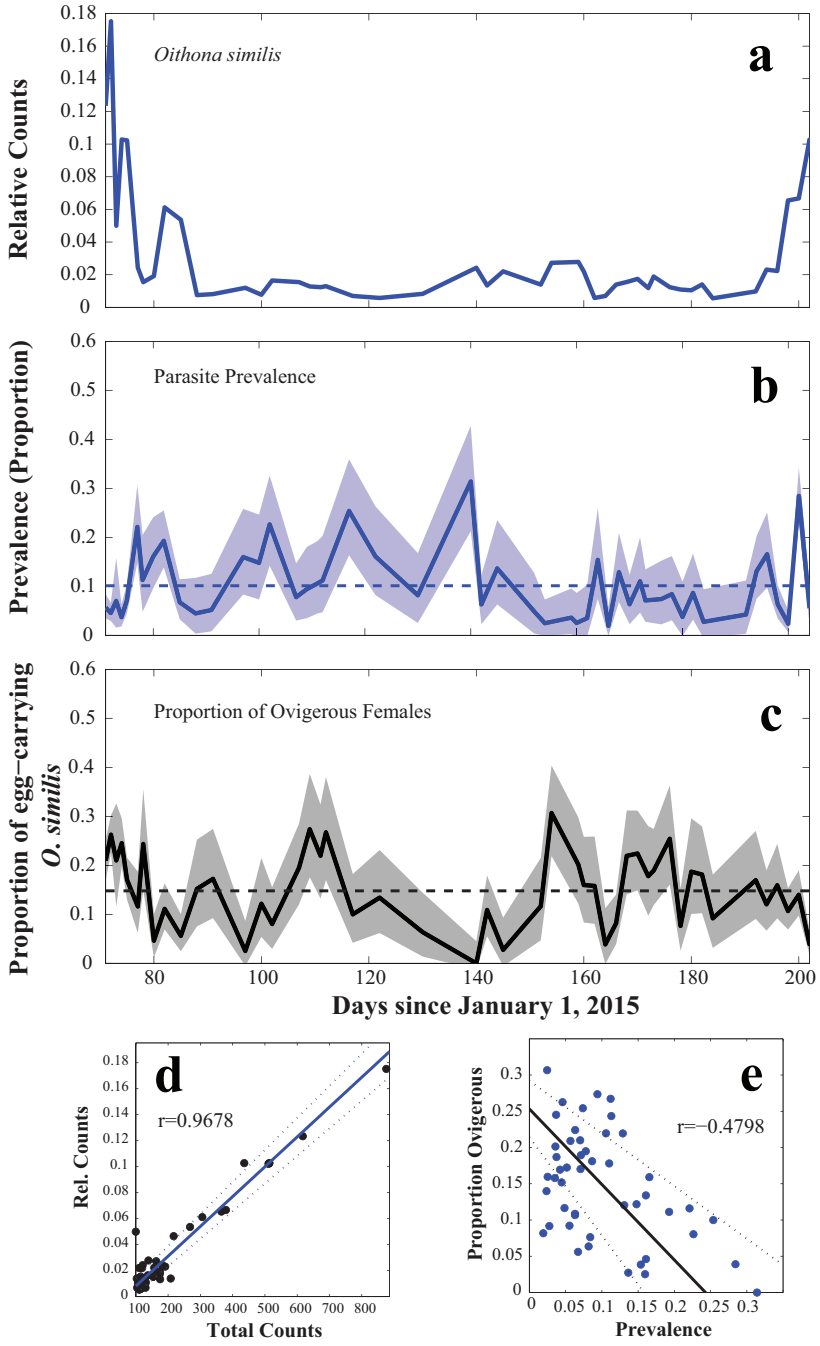

Figure 5.3. Time series of *Oithona similis* and *Paradinium poucheti* using the Scripps Plankton Camera data. a) Relative counts of *Oithona similis*; b) parasite prevalence; c) proportion of ovigerous females. Shaded areas in a and b represent the 95% confidence intervals (C.I.) estimated using equations 1 and 2. Dashed horizontal lines are the overall mean values for each series. d) Type II regression between total *O. similis* counts and relative counts and e) Type II regression between parasite (*P. poucheti*) prevalence and proportions of ovigerous females. Dotted lines on d and e represent the 95 C.I.

5.6. References

Bates, A.E., Stickle, W.B., and Harley, C.D.G. (2010) Impact of temperature on an emerging parasitic association between a sperm-feeding scuticociliate and Northeast Pacific sea stars. *J. Exp. Biol. Ecol.*, 384, 44--50.

Briseño-Avena, C., Roberts, P.L.D., Franks, P.J.S., and Jaffe, J.S. 2015. ZOOPS-O^2: a broadband echosounder with coordinated stereo optical imaging for observing plankton in situ. *Methods in Oceanography*, 12: 36-64.

Drif, K., Hirst, A.G., and Hay, S. (2010) Seasonal abundance and egg production rates of *Oithona similis* and *Pseudocalanus elongates* in the northern North Sea: a first comparison of egg-ratio and incubation methods. *Mar. Ecol. Progr. Ser.*, 415, 159--175.

Fields, D.M., Runge, J.A.,Thompson, C., Shema, S.D., Bjelland, R.M., Durif, C.M.E., Skiftesvik, A.B., and Browman, H.I. (2015) Infection of planktonic copepod *Calanus finmarchicus* by the parasitic dinoflagellate, *Blastodinium* spp: effects on grazing, respiration, fecundity and fecal pellet production. *J. Plankton Res.*, 37, 211--220.

Harvell, C.D., Mitchell, C.E., Ward, J.R., Altizer, S., Dobson, A.P., Ostfeld, R.S., and Samuel, M.D. (2002) Climate warming and disease risks for terrestrial and marine biota. *Science*, 296, 2158--2162.

Ho, J. and Perkins, P.S. (1985) Symbionts of marine copepoda: an overview. *B. Mar. Sci.*, 37, 586--598.

Jepps, M. W. (1937) On the protozoan parasites of Calanus finmarchicus in the Clyde Sea area. *Q. J. Microsc. Sci.*, 79, 589--658.

Kimmerer, W.J. and McKinnon, A.D. (1990) High mortality in a copepod population caused by a parasitic dinoflagellate. *Mar. Biol.*, 107, 449--452.

Kutz, S.J., Hoberg, E.P., Polley, L., and Jenkins, E.J. (2005) Global warming is changing the dynamics of Arctic host-parasite systems. *P. Roy. Soc. B-Biol. Sci.*, 272, 2571--2576.

Larsen, M. H., and Mouritsen, K.N. (2014) Temperature-parasitism synergy alters intertidal soft-bottom community structure. *J. Exp. Mar. Biol. Ecol.*, 460, 109--119.

Legendre, L. and Rivkin, R.B. (2002) Fluxes of carbon in the upper ocean: regulation by food-web control nodes. *Mar. Ecol. Progr. Ser.*, 242, 95--109.

Lima-Mendez, G., Faust, K., Henry, N., Decelle, J., Colin, S., Carcillo, F., Chaffron, S., Ignacio-Espinoza, J.C., Roux, S., Vincent, F., Bittner, L., Darzi, Y., Wang, J., Audic, S., Berline, L., Bontempi, G., Cabello, A.M., Coppola, L., Cornejo-Castillo, F.M., d'Ovidio, F., Meester, L.D., Ferrera, I., Garet-Delmas, M., Guidi, L., Lara, E., Pesant, S., Royo-Llonch, M., Salazar, G., Sánchez, P., Sebastian, M., Souffreau, C., Dimier, C., Picheral, M., Searson, S., Kandels-Lewis, S., Tara Oceans coordinators Gorsky, G., Not, F., Ogata, H., Speich, S., Stemmann, L., Weissembach, J., Wincker, P., Acinas, S.G., Sunagawa, S., Bork, P., Sullivan, M.B., Karsenti, E., Bowler, C., de Vargas, C., and Raes, J. (2015) Determinants of community structure in the global plankton interactome. *Science*, 348, 1262073-1--9.

Macnab, V. and Barber, I. (2012) Some (worms) like it hot: fish parasites grow faster in warmer water, and alter host thermal preferences. *Glob. Change Biol.*, 18,1540--1548.

Ohtsuka, S., Horiguchi, T., Hanamura, Y., Yamaguchi, A., Shimomura, M., Suzaki, T., Ishiguro, K., Hanaoka, et al. (2011) Symbionts of planktonic copepods and mysids with epibionts and parasites in the North Pacific: diversity and interactions. *In* Asakura, A., Bauer, R.T., Hines, A.H., Thiel, M., Wada, K., Yamaguchi, T., Held, C., Schubart, C. et al. (eds.). New frontiers in crustacean biology: Proceedings of the TCS summer meeting, Tokyo, 20-24 September 2009. *Crustaceana Monographs*, Brill, Leiden, The Neatherlands, 15, 1--14.

Razouls, C., de Bovée, F., Kouwenderg, J., and Desreumaux, N. (2005-2015) Diversité et repartition géographique chez le Copépodes planctoniques marins. Available at: http://copepodes.obs-banyuls.fr

Schminke, H.K. (2007) Entomology for the copepodologist. *J. Plankton Res.*, 29, i149--i162.

Shields, J.D. (1994) The parasitic dinoflagellates of marine crustaceans. *Annu. Rev. Fish Dis*., 4, 241--271.

Scovgaard, A. (2014) Dirty Tricks in the Plankton: Diversity and Role of Marine Parasitic Protists. *Acta Protozool.*, 53, 51--62.

Skovgaard, A. and Daugbjerg, N. (2008) Identity and systematic position of *Paradinium poucheti* and other *Paradinium*-like parasites of marine copepods based on morphology and nuclear-encoded SSU rDNA. *Protist*, 159, 401--413.

Skovgaard, A. and Sainz, E. (2006) Seasonal occurrence and role of protistan parasites in coastal marine zooplankton. *Mar. Ecol. Progr. Ser*., 327, 37--49.

Studer, A., Thieltges, D.W. and Poulin, R. (2010) Parasites and global warming: net effects of temperature on an intertidal host-parasite system. *Mar. Ecol. Progr. Ser.*, 415, 11--22.

Wiedermann, M.M., Nordin, A., Gunnarsson, U., Nilsson, M.B., and Ericson, L. (2007) *Ecology*, **88**: 454--464.

Chapter 6

Conclusions

Chapter 2 described the fine-scale vertical distributions of five zooplankton taxa in relation to fluorescent particle distributions, acquired using two *in situ* optical systems: PLIF and O-Cam. The fine-scale resolution of the biological and hydrographic data showed that water density explained much of the temporal variability of the vertical distributions of both zooplankton and fluorescent particles. Such observations would not have been possible using net sampling techniques, which tend to average away such fine structures. The location of each zooplankton group in relation to the fluorescent particle distribution and with respect to each other was explained by invoking predator-prey interactions. Cyclopoid copepods, for example tended to avoid areas where their predators were present in large abundances, while calanoid copepods tended to be present in areas where a suitable assemblage of prey (appendicularians and marine snow aggregates) was present – in spite of being exposed to higher abundances of their own predators: hydromedusae. The shallow distributions of appendicularians suggested that we observed a reproduction event. The observations made here present a very dynamic ecological picture. Future observations using these tools should include daylight deployments and more frequent sampling to observe diel vertical distributions. Extending these observations to other seasons would also help us understand whether the location of cyclopoid copepods beneath both the chlorophyll a maximum and fluorescent particle maximum is a

recurrent phenomenon. The latter is particularly important, for it may have important effects on carbon export via fecal pellet production below the seasonal thermocline.

Chapter 3 described ZOOPS-O^2, a system that combines a stereoscopic camera system with broadband sonar to estimate acoustic reflectivity of individual plankton with concurrent measurement of their size and orientation. Measurements of the system's performance show that copepods as small as 360 μm give a reflected broadband target strength (BTS) that is at least 10 dB above the system's noise level. The 1.5 mm range resolution of ZOOPS, along with the visual identification capabilities of the O-Cam (designated O^2 in stereoscopic mode) permits extraction of echo properties of individual copepod targets in their natural environment with concurrent identification. As demonstrated, ZOOPS-O^2 can be used to study the acoustic properties of this ecologically important plankton group *in situ*. **Chapter 3** also explored the differences between the *in situ* measured versus a physical model prediction of BTS and spectra for a group of 224 pelagic copepods. The results of this comparison showed that the copepod pose with respect to the transducer was less orientation-dependent than the model suggested. In the future, ZOOPS-O^2 could be used to carry out experiments to compare the *in situ* versus modeled BTS and spectra of organisms such as euphausiids, mysids, and chaetognaths, as it was done for copepods in **Chapter 3**. Such exercises will be useful to refine extant models and consider more complex body shapes.

Chapter 4 showed that gelatinous and marine snow individual targets are capable of reflecting broadband, high frequency (1.5-2.5 MHz) acoustic energy. This

work also showed that even diatoms in high concentrations were capable of reflecting sound at these high frequencies. Knowing that diatom and marine snow layers are conspicuous and recurrent features of coastal waters, the results of this work suggest that such particles should be taken into consideration during acoustic surveys. Furthermore, concentrations of gelatinous organisms (jellyfish, siphonophores, doliolids and salps – although no salps where observed in the present work) can be significant and dominate the zooplankton abundance at times. The reflectivity of such organisms observed in **Chapter 4** indicates they should be more carefully considered during research acoustic surveys.

The emergence of commercially available wide-band technologies creates new opportunities for the use of processing methods for interpreting acoustic data. While not fully considered in the work presented in **Chapter 4**, the properties of acoustic echoes (e.g., the echo envelope) can add more degrees of freedom to acoustic target classification. The information contained in such acoustic envelopes could be a rich area for future exploration to improve target discrimination. These results underscore the need to exercise caution when interpreting acoustic data based solely on target strength measurements.

Future field biological surveys should incorporate a suite of technologies including acoustic, optic, and net systems to capture a more complete picture of planktonic distributions. In light of the observations presented in **Chapter 4**, a zooplankton survey using acoustics should clearly take into account phytoplankton and marine snow. While nets target a finite size-range of planktonic organisms,

retaining large particles and destroying fragile organisms and marine snow particles, optical systems can be superior tools because of their non-invasive capabilities. Furthermore, nets cannot resolve the fine spatial scales at which phytoplankton and marine snow layers occur. Optical tools, on the other hand, can be used to detect such ubiquitous features and provide ground truthing information for acoustic studies that might be affected by phytoplankton, marine snow and fragile, gelatinous taxa.

Chapter 5, using a moored underwater microscope, the Scripps Plankton Camera, presented the first report in the North Pacific Ocean of a parasite (*Paradinium poucheti*) affecting *Oithona similis* copepods. Previous observations of this parasite came from the North Atlantic Ocean and the Mediterranean Sea. Clearly, there is a need to quantify the natural abundance of *P. poucheti* and its infection rate of its host. Future work should focus on culturing the host and parasite to establish the nature of this symbiotic relationship and to further understand how the host is affected. Information on the growth rate of *P. poucheti* should also be investigated, as well as the environmental parameters controlling the development and dispersion of the parasite and its infection of its host. Answering these basic questions will be necessary to appropriately interpret the variability observed in the *Oithona similis*-*Paradinium poucheti* time series.